Doctoral dissertation

Prepared in the Institute of Physics of the Jagiellonian University

Submitted to the Faculty of Physics, Astronomy
and Applied Computer Science
of the Jagiellonian University

Investigations of mechanisms of particle production in proton-induced nuclear spallation

Udai Singh

Supervised by dr hab. Krzysztof Pysz, prof. IFJ PAN

Co-supervised by:
dr Sushil Sharma

Cracow 2021

Wydział Fizyki, Astronomii i Informatyki Stosowanej
Uniwersytet Jagielloński

Oświadczenie

Ja niżej podpisany Udai Singh (nr indeksu: 11 42 423) doktorant Wydziału Fizyki, Astronomii i Informatyki Stosowanej Uniwersytetu Jagiellońskiego oświadczam, że przedłożona przeze mnie rozprawa doktorska pt. *"Investigations of mechanisms of particle production in proton-induced nuclear spallation"* jest oryginalna i przedstawia wyniki badań wykonanych przeze mnie osobiście, pod kierunkiem dr hab. Krzysztof Pysza. Pracę napisałem samodzielnie.

Oświadczam, że moja rozprawa doktorska została opracowana zgodnie z Ustawą o prawie autorskim i prawach pokrewnych z dnia 4 lutego 1994 r. (Dziennik Ustaw 1994 nr 24 poz. 83 wraz z późniejszymi zmianami).

Jestem świadom, że niezgodność niniejszego oświadczenia z prawdą ujawniona w dowolnym czasie, niezależnie od skutków prawnych wynikających z ww. ustawy, może spowodować unieważnienie stopnia nabytego na podstawie tej rozprawy.

Kraków, dnia 6.09.2021 . . . .

1

Dedication

This work is dedicated to my late Mother. Also to my Father, Grand Mother, my younger Brothers and my late supervisor Prof. dr. hab. Zbigniew Rudy.

Abstract

Studies of the selected problems in understanding of nuclear spallation physics are undertaken. Among them are the description of the initial phase of proton - target nucleus collision and proceeding of the intranuclear cascade, isotropic emission of nuclear fragments of very broad mass spectrum, contribution of the nonequlibrium and equilibrium processes to the total production cross-section and its dependence on the isotope isospin, variation of the total production cross-section related to the number and ratio of protons and neutrons of the emitted particle. New experimental distributions of the double differential production cross-sections ($d^2\sigma/d\Omega dE$) for p, d, t, π^+ and π^- in the $p + Nb$ reaction at 3.5 GeV proton beam energy are provided. They have been measured by High Acceptance DiElectron Spectrometer (HADES) experiment. The measured energy range of hydrogen isotopes are significantly extended in comparison to the experimental data available in the literature. The new experimental spectra are confronted with the theoretical prediction of three models of intranuclear cascade - GiBUU, UrQMD, INCL++. Discrepancies of the experimental and theoretical distributions are noticed and discussed. Experimental data derived from the literature are used for examination of nuclear mechanisms assigned to the nuclear deexcitation phenomena. The comparative analysis of the four model prediction (ABLA07, GEMINI++, GEM2, SMM) of the selected observables relevant to the isotropic nuclear fragment emission is performed. Disagreement of the model prediction and the experimental data is observed.

Acknowledgements

First of all, I want to express my gratitude to my supervisor Prof. Krzysztof Pysz for the great help and assistance during the data analysis, their interpretation and preparation of this dissertation. I would also like to thank my co-supervisor, Dr. Sushil Sharma, for his guidance and dedicated participation at every stage of progress. I would also like to sincerely remember my first (late) Ph.D. supervisor Prof. Zbigniew Rudy for inviting me to join the spallation research group at Jagiellonian University and guiding me in first year of my Ph.D.

I want to express my heartfelt gratitude to Prof. Bogusław Kamys for his continuous support and many important explanations and discussions about life, especially the different expectations of spallation reactions. I would also like to thank him for his critical reading of the manuscript and necessary corrections.

I am very grateful to Prof. Paweł Moskal for allowing me to prepare this dissertation in the Faculty of Physics, Astronomy and Applied Computer Science of the Jagiellonian University.

I am indebted to Prof. Piotr Salabura for allowing me to work in the HADES group and always supporting me. I appreciate that I was allowed to participate in the HADES collaboration and use the data collected in the HADES experiment. I am very grateful to all my colleagues from HADES, especially Prof. Jerzy Smyrski, Prof. Witold Przygoda, Dr. Rafal Lalik, Prof. Manuel Lorenz, Prof. Izabela Ciepał, Krzysztof Nowakowski, Akshay Malige, Narendra Rathod and others. They always provided me with the necessary information and explanations. I would also like to thank all my colleagues from the cluster of nuclear physics departments. They were always kind to me and supported me.

Last but not least, I would like to thank Anjali Aggarwal for her constant support and motivation during the years of my Ph.D. studies. Tireless discussions about interesting topics in physics and general topics have kept this journey fascinating all these years. Without her always being there for me, I would not have been able to finish this work.

Contents

Chapter 1

Introduction

1.1   Spallation reaction

The nuclear spallation is a sequence of reactions induced when a target nucleus is struck by an incident particle of energy greater than around 50 MeV. In such a collision the emission of nucleons, light charged particles (LCP), i.e., particles heavier than proton but lighter than ^{5}He, and heavier nuclei may be expected besides elastic and inelastic collision of the projectile with the target nucleus. The nucleus resulting from the first collision is usually excited and may emit further ejectiles during its rearrangement. Therefore various nuclear processes may be involved, which usually lead to a significant modification of the initial nucleus.

1.1.1   Why study nuclear spallation?

Understanding these processes is interesting, but there are also practical reasons to undertake the studies of nuclear spallation. The gained knowledge can be used in numerous scientific, technological and medical applications. Only a few of them are mentioned below. They are:

- construction of the neutron sources used for scientific studies and technology applications [1];

- conversion of long-living nuclear waste into nonradioactive substances or short life products [2];

- production of short-living rare isotopes for medical science studies [3] and scientific purposes [4];

- construction of various kinds of radiation protection to be used on Earth or in the spacecraft;

- simulation and construction of detection apparatus for nuclear and particle physics.

1.1.2 The need for theoretical models

For such a broad range of applications of nuclear spallation, there is demand for the knowledge about the relevant quantities. They are, e.g., the total and differential cross-sections for the production of various nuclides. Usually, it is difficult, time-consuming and/or costly to obtain experimentally desirable information. Therefore the existence of a reliable theory of the mechanisms contributing to the spallation reactions is necessary.

Nuclear spallation is a complicated phenomenon proceeding in the many-body, excited quantum system. Due to the lack of analytical mathematical formalism of such processes, the simplified models have to be used. They contain contemporary knowledge about nuclear systems and nuclear reactions, usually with many unavoidable approximations. Models provide the solutions using the Monte Carlo simulations.

The models are developed and optimized in an iterative manner taking input from the information obtained experimentally. Thus, it is crucial to provide valuable and precise experimental observables for models development and benchmarking.

1.1.3 Types of models

In the modeling of the proton (p) - target nucleus (A) collision most commonly the idea of Serber [5] is adopted. It assumes that the p - A collision proceeds in two steps of different time span:

- The first and fast stage of the reaction consists of an intranuclear cascade (INC) of nucleon-nucleon and nucleon-pion collisions, leading to significant emission of nucleons, pions and nuclear clusters called Light Charged Particles (LCP). The excited residuum of the target nucleus appears in thermodynamical equilibrium.
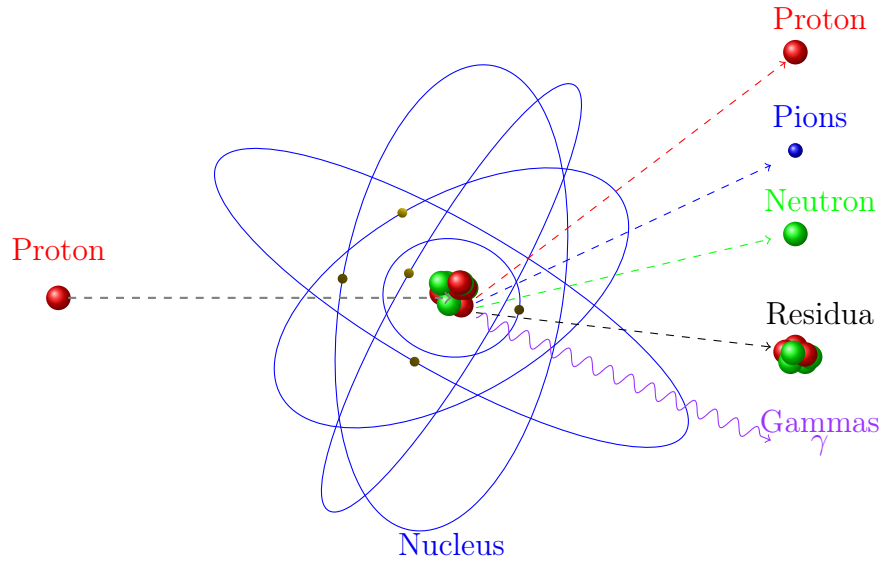
Figure 1.1: Particle emission in the first stage of the spallation reaction

- In the second stage (extended in time), various de-excitation processes of the residual excited nucleus are involved. The emission of single nucleons, LCP, heavier clusters (so-called Intermediate Mass Fragments - IMF) is possible due to evaporation, fission and/or fragmentation processes.

Fig 1.1.3 presents the particle emission during the intranuclear cascade.

Various models used for simulation of both of these two stages of the reaction are available.

The dynamical - first step o reaction can be simulated, e.g., with the following models: INCL++ [6–10], GiBUU [11], UrQMD [12, 13], JAM [14], Bertini [15, 16], CEM [17], ISABEL [18, 19].

The slow deexcitation of the after-cascade remnant is calculated, e.g., in ABLA07 [20], GEMINI++ [21, 22], GEM2 [23, 24], SMM [25].

The selection of the model depends on the projectile energy, target mass, resulting excitation energy, demanded quantity of interest but also on credibility of the model's results.

For example, the combination of the cascade model of INCL4.6 with the deexcitation model ABLA07 is able [9] to describe with the precision of factor 2 the total cross-sections as well as the energy spectra and angular distribu-

tions of neutrons, protons and pions for the broad range of the bombarding energies of the light projectile (from 50 MeV to 5 GeV). The experimental yields of the remnant nuclei could be reproduced as well.

However, these models - similarly to all other spallation models - meet a problem of the explanation and quantitative description of the non-equilibrium emission of complex light charged particles (LCP), *i.e.*, d, t, ^3He and ^4He as well as of the intermediate mass fragments (IMF), *i.e.*, particles heavier than ^4He but lighter than products of the fission.

1.2   Questions that need to be answered in nuclear spallation research

After many years of research in this field of experimental and theoretical groups, many fundamental questions are still unanswered. The main of them are:

- Is the assumption about the two step model justified or the scenario of the reaction is different (e.g., instantaneous formation of a few excited moving sources of particle emission [26]) ?

- What are the mechanisms acting during the initial part of collision? Is the energy/momentum dissipation within the target nucleus realized only by the binary collisions or other mechanisms are present as well ?

- How far it is justified to use the experimental nucleus-nucleus and nucleus-pion cross-sections measured in the vacuum for calculation of collision probability within the nuclear medium ?

- What are the mechanisms responsible for the creation of fast composite nuclear particles ?

- How far the excited nuclear quantum system can be approximated by the statistical ensemble of point-like particles described by thermodynamics ?

Some of these fundamental questions are addressed also in this thesis. The general assumption about the two step scenario of spallation process is adopted.

1.3 Organization of thesis

The review of contemporary theoretical models used for description of the spallation reactions is presented in chapter 2. The following experimental and theoretical objectives of the present work are discussed in the further chapters of the thesis:

i) Studies of the first step of spallation reaction (chapters 3 and 4): the experimental determination of the differential cross-section $(d^2\sigma/d\Omega dE)$ for emission of Hydrogen isotopes as well as charged pions from collisions of protons with Nb nuclei at $E_p = 3.5$ GeV (experiment performed in the frame of HADES collaboration) and theoretical description of the obtained data;

ii) Second step of the reaction - phenomena governing the deexcitation of the remnant of the first step: the theoretical analysis of the data published in the literature, which contain total isotopic cross-sections for production of nuclei from Li to Ba in $p+^{136}Xe$ collision at $E_p = 1$ GeV. Results of this analysis were partially published in [27] and [28]. For this subject the chapter 5 is devoted;

iii) Examination of the contribution of the non-equilibrium and equilibruim processes to the total production cross-section for various isotopes and its dependence on the ratio of protons and neutrons in the emitted object (chapter 6). For this aim the data of $p + Ag$ collisions at $E_p = 480$ MeV published in [29] were utilized;

iv) Theoretical assessment of the experimental observation of variation visible in the total production cross-section for various isotopes of similar mass number A known as Odd-Even Staggering of cross-section (OES). The experimental cross-section are adopted from [29]. This topic is presented in chapter 7.

The thesis is concluded with the summary.

Chapter 2

Contemporary theoretical models for spallation reactions

In this chapter some theoretical models, which are applicable for description of proton-induced spallation reactions will be discussed. According to hypothesis of Serber [5], such a reaction proceeds in two steps. The first step is a cascade of binary collisions among the constituents of the target nucleus, induced by the impinging projectile. This stage lasts a few fm/c. Elastic and inelastic interactions lead to distribution of the excitation among the target nucleons and creation of resonances (mainly deltas). Decay of resonances is a source of pions, which additionally contribute to the cascade of interactions. Those of nucleons and pions, which energies exceed their separation energies can be emitted. Also the complex objects like the H and He isotopes (and even heavier composite particles) can appear in this stage of reaction.

   The hypothesis of Serber assumes furthermore that after cascade of emissions of fast particles the excited remnant of the target nucleus is left in its thermal equilibrium.

   The second stage of the reaction consists in de-excitation of this remnant nucleus by various processes like particle evaporation, (multi-) fragmentation, asymmetric and symmetric fission. These processes are a source of single nucleons, light composite nuclear aggregates called the light charge particles (LCP), Intermediate Mass Fragments (IMF) of the mass number $A > 4$ but lighter than fission fragments and heavy residues.

   In general the shapes of experimental spectra of spallation reactions can be described with the models adopting such two step scenario of reaction. However, the low precision of the theoretical reproduction of the data induces

the need for looking for more complicated or quite different hypotheses of the reaction scenarios. For example there are models, which assume the three steps of the reaction. The intermediate stage called a pre-equilibrium stage is assumed between the cascade and the full thermal equilibration of the system.

In the next sections, a most commonly used models of the first and the second stage of reactions will be described.

2.1 Models of the first stage reactions

Among the models used to describe the dynamics of the proton target nucleus collision (i.e. first stage of reaction) are INCL [6–10], GiBUU[11], UrQMD[12, 13], JAM[14], INC by Bertini [15, 16], CEM [17], and ISABEL [18, 19]. Some of the them were created especially to study the spallation reactions (INCL, INC). Others try to describe in general the collisions of nuclear objects (e.g. the heavy ion collisions) and broad diversity of fundamental nuclear processes (GiBUU, UrQMD).

2.1.1 Intranuclear cascade models - INC

In the simplest approximation the proceeding of the first step of reaction - the intranuclear cascade (INC) can be imagined as collisions of the free nucleons, pions and other particles embedded in the volume of the target nucleus. Individual collisions take place if predefined conditions are fulfilled. The excitation of Δ resonance is one of possible effects of interaction of two nucleons or nucleon and pion. When Δ de-excites the pion is created. Particles, which gained enough energy are emitted from the nucleus but those whose kinetic energy is lower than their separation energy are reflected at the nuclear surface back into the nucleus. Such simplified picture of intranuclear reaction is presented in fig. 2.1.

The first model of this type has been created by Bertini in 1963 [15, 16]. Later, this conception was used also in other codes, e.g. by Yariv in his ISABEL code [18, 19]. In the 80's and 90's, the several versions of INC model were developed by Cugnon et al. [6–9]. Model of Cugnon was called Intranuclear Cascade Liège - INCL. Its latest version, utilized in this thesis, is INCL++5.6 [10].
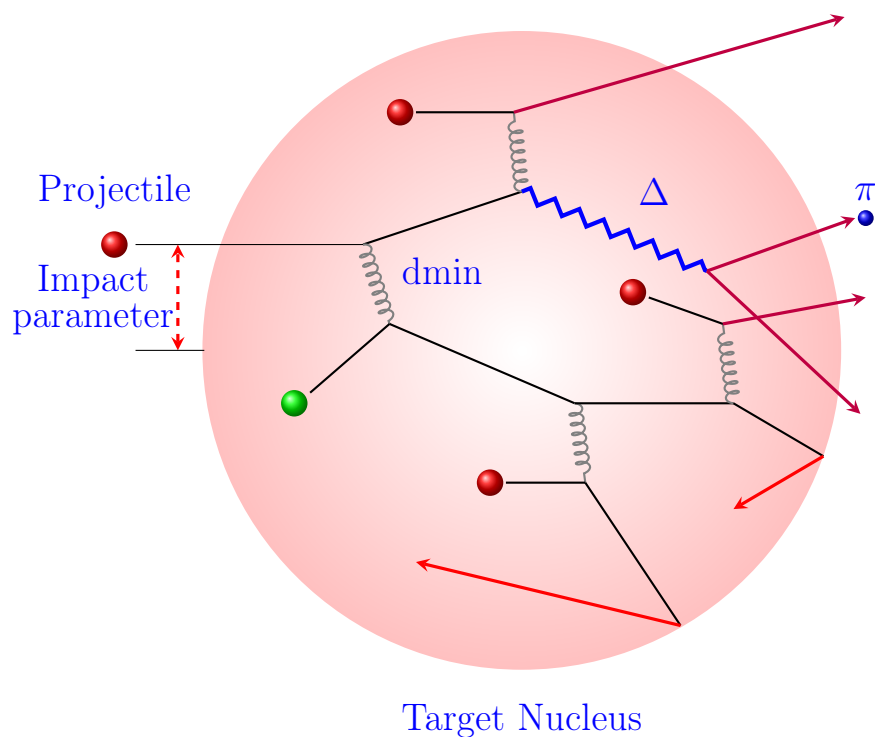
Figure 2.1: Schematic explanation of the proceeding of the intranuclear cascade (INC). For details see text.

INCL++ is most advanced among the models which utilize the assumption of the target nucleus as a Fermi gas of free nucleons kept in the nuclear potential well. It this work it is used both as one of the theoretical models confronted with the experimental data as well as reliable event generator used for simulation of response of detection system. Thus, it is described here in more details as the best example of the family of semi-classical INC models.

Features of INCL model

The most important assumptions used in INCL++ model are as follows:

(i) Target nucleus is treated as Fermi gas of protons and neutrons embedded in the potential well;

(ii) Initial positions of nucleons are stochastically selected inside the sphere of the radius dependent on the mass number A and the selected density profile;

(iii) Initial momenta of nucleons are as well randomly distributed inside the Fermi momentum sphere;

(iv) Nucleons move inside the nucleus along straight trajectories until two of them collide or until one nucleon reaches the nucleus surface, where it can be transmitted or reflected (shown in figure 2.1).

(v) Collision takes place when the distance between two nucleons is smaller than d_{min} which is given by:

$$d_{min} \leq \sqrt{\sigma_{tot}/\pi} \qquad (2.1)$$

where σ_{tot} is the free space total nucleon-nucleon cross-section;

(vi) Nucleons are divided into participants (these which take part in the collision) and spectators (not collided). Spectator cannot be emitted;

(vii) Pauli blocking is checked both during creation of initial phase-space distribution of nucleons as well as for final state of each collision;

(viii) Relativistic kinematics is used in this model.

Construction of target nucleus

The spatial distribution $\rho(r)$ of nucleons inside the target nucleus is prepared according to a Saxon-Woods formula:

$$\rho(r) = \begin{cases} \frac{\rho_0}{1+\exp(\frac{r-R_0}{a})} & r \leq R_{max} \\ 0 & r > R_{max} \end{cases} \qquad (2.2)$$

where $R_{max} = r_{int} + R_0 + 8a$ and $r_{int} = (\sigma_{NN}^{tot}/\pi)^{\frac{1}{2}}$. The σ_{NN}^{tot} is the the free space total nucleon-nucleon cross-section.

The R_0 and a values are taken from electron scattering measurements for Al to U target nuclei and parametrized as below.

$$R_0 = (2.7545 * 10^{-4} A_T + 1.063) A_T^{1/3} \tag{2.3}$$

$$a = 0.510 + 1.63 * 10^{-4} A_T \tag{2.4}$$

A_T is the mass number of the target nucleus.

The initial position and momentum of any target nucleon are generated as follows. First momentum p is taken randomly from a sphere of radius P_F. Then $R(p)$ corresponding to momentum p is calculated by equation 2.5. After that the position r is randomly selected from the sphere of radius $R(p)$.

$$\left(\frac{p}{P_F}\right)^3 = -\frac{4\pi}{3 A_T} \int_0^{R(p)} \frac{d\rho(r)}{dr} r^3 dr, \tag{2.5}$$

For more details please, refer to [7].

Potentials

In the INCL++ model both the nuclear as well as the Coulomb potentials for nucleons and pions are taken into account. Potentials for Δ particles are neglected.

Particles of the target nucleus are kept inside a potential well which approximates the mean nuclear potential. The value of the nuclear potential for nucleons is dependent on their actual energy. The dependence of the potential on the isospin of the nucleon is kept as well.

The energy and isospin dependent potential for nucleons is calculated according to formula 2.6:

$$V^i(E) = \begin{cases} V_0^i - \alpha \left(E - E_F^i\right) & E \leq E_0 \\ 0 & E > E_0 \end{cases} \tag{2.6}$$

In this equation superscript i stands for proton $(i = p)$ or neutron $(i = n)$. The parameter α of formula 2.6 is fixed and equal to 0.23, where energy E of nucleon of momentum k can be calculated by:

$$E = \frac{\hbar^2 k^2}{2M} + V_0^i(E) \tag{2.7}$$

The deepness of the potential V_0^i is calculated from the Koopman's theorem [30]:

$$V_0^i = S_i + T_F^i \tag{2.8}$$

where the appropriate quantities of separation energies S_i are taken from experiments [31]. The kinetic energy T_F^i of the particle i ($i = p$ for proton or $= n$ for neutron) is related to its Fermi momentum k_F^i which is different for proton and neutron and given by:

$$T_F^i = \frac{(\hbar k_F^i)^2}{2M} \tag{2.9}$$

where M is the mass of nucleon and $\hbar$ is the reduced Planck constant.

The limiting value of E_0 above, at which the nuclear potential for nucleons vanishes is equal to:

$$E_0 = \frac{V_0^i}{\alpha} + T_F^i \tag{2.10}$$

where α is a parameter having value 0.23. The values of the energy independent potentials for pions are distinguished according to their third component of isospin τ_3. They are energy independent. Potential for individual pion types are calculated according to [32]:

$$V(r, \tau_3) = V_t(\tau_3) = V_N(\tau_3) + \overline{V}_C, \qquad \text{for } r \leq R_c \tag{2.11}$$

$$V(r, \tau_3) = V_C(r) = \frac{Z_T \tau_3 e^2}{r}, \qquad \text{for } r > R_c \tag{2.12}$$

where Z_T is an atomic number for target nucleus, R_c is the radius where potential reduces to Coulomb potential and r is position of particle where potential is calculated.

When pions propagate inside the sphere of R_c they are influenced both by the average Coulomb potential $\overline{V}_C$ and by the nuclear potential $V_N(\tau_3)$. These potentials are calculated, respectively, by the formulas:

$$\overline{V}_C = \tau_3 \frac{1.25 Z_T e^2}{R_0} \tag{2.13}$$

(e - charge of electron, R_0 radius of nucleus)

and

$$V_N(\tau_3) = V_N^0 + V_N^1 \tau_3 \xi \tag{2.14}$$

Where $\xi = (N_T - Z_T)/A_T$ is the charge asymmetry parameter of target and the values of V_N^0 and V_N^1 are constant:

$$V_N^0 = -30.6 MeV \tag{2.15}$$
$$V_N^1 = -71.0 MeV \tag{2.16}$$

They were determined by tuning of the model results to the experimental data.

For the case of $r > R_c$ the potential reduces to the average Coulomb potential which is given by (2.12).

The Coulomb potential is considered as well when projectile enters the target nucleus and when the charged particles are emitted from it. The trajectories of particles are deflected accordingly to electrical field. The probability of penetration of Coulomb barier is calculated as well for emission of charged particles.

The potentials discussed here are inspired from known phenomenology. Values of theirs parameters are fixed.

Collisions between nucleons

Particles inside the nucleus propagate according to their current momenta. Their position is calculated for each time step. After each time step also the distances between particles are checked. If two of them get closer than minimal distance d their collision can take place. For this aim the following conditions are checked:

i) whether the distance d between two nucleons is smaller than:

$$d \leq \sqrt{\sigma_{tot}/\pi} \tag{2.17}$$

where σ_{tot} is the free space total cross-section for colliding nucleons at their current energies;

ii) whether the total center of mass energy of colliding particles is greater than 1910 MeV;

iii) whether the phase space is available for collision products.

The above mentioned total cross-section σ_{tot} is a sum of partial cross-sections of the processes included to the model and appropriate for the colliding particles and their energies. In the INCL++ the following possible reactions are considered:

$$NN \rightleftarrows NN(elastic) \quad NN \rightleftarrows N\Delta \quad N\Delta \rightleftarrows N\Delta(\text{delta absorption})$$
$$\Delta\Delta \rightleftarrows \Delta\Delta \quad\quad\quad \pi N \rightleftarrows \Delta$$
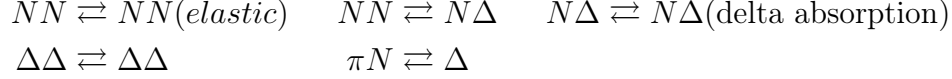
Listed here are only those processes which are relevant for the nuclear physics range studied in this thesis. But it general with the use of INCL++ much more fundamental interactions can be simulated. For example:

$$NN \rightarrow NN\omega, \quad NN \rightarrow N\Delta\omega, \quad NN \rightarrow NN\omega + x\pi$$
$$\pi N \rightleftarrows N\omega, \quad \omega N \rightleftarrows \omega N, \quad \omega N \rightarrow N\pi\pi$$
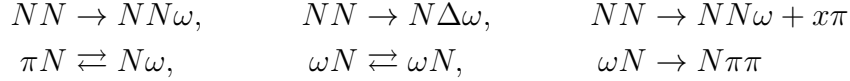
The probability of the kind of reaction which will be realized by the model is probed according to the balance of the values of individual cross-sections, which have to be taken into account for the colliding particles and their energies.

The angular dependence of the flight directions of the colliding objects is probed according to the parametrized differential angular cross-sections:

$$\frac{d\sigma}{d\Omega} \sim exp(B \cdot t) \tag{2.18}$$

where B is a parameter and t is the Mandelstam variable dependent on the center of mass momentum (p_{CM}^2) of colliding particles and the scattering angle θ:

$$t = -2 \cdot p_{CM}^2 \cdot (1 - cos\theta) \tag{2.19}$$

Pauli Blocking

The quantum nature of colliding systems is to some extent taken into account by introduction of the mechanism of Pauli blocking [7]. It blocks the interaction if final states of the participants of the collision are occupied.

The strict Pauli blocking is observed always for first collision [9]. The populated states of colliding particles should lie above the Fermi sea. Otherwise the collision is blocked. For the subsequent collisions the available phase-space is probed stochastically as described below.

The final state of two colliding objects i and j is given by their positions $(\vec{r(i)}, \vec{r(j)})$ and momenta $(\vec{p(i)}, \vec{p(j)})$.

The probability P that the interaction will not be blocked by limitation of the available phase space is given by:

$$P = (1 - f_i)(1 - f_j) \tag{2.20}$$

Where function f_i, f_j are calculated taking in respect the current occupation of the phase space by fermions of the same type as i and j:

$$f_i = \frac{1}{2} \frac{(2\pi\hbar)^3}{\frac{4\pi}{3} r_{PB}^3 \cdot \frac{4\pi}{3} p_{PB}^3} \sum_{k \neq i} \theta(r_{PB} - |\vec{r_k} - \vec{r_i}|)\, \theta(p_{PB} - |\vec{p_k} - \vec{p_i}|) \tag{2.21}$$

(the same for f_j).

The θ denotes here the Heaviside function and the factor $1/2$ is for the spin. The sum is taken over fermions k of same isospin state as i located inside the sphere of radius r_{PB} and having momenta inside the momentum sphere of p_{PB}. Thus, in other words, the r_{PB} and p_{PB} denote the sizes of the test volumes in phase space.

In the same way the f_j function is calculated.

The values of r_{PB} and p_{PB} used in INCL++ are optimized by comparison of the model results with the experimental data. They take the values of 3.18 fm and 200 MeV/c, respectively (cf. [33]).

Cluster creation and emission

In the INCL++ model for creation of the light charged particles (LCP) the hypothesis of so called surface coalescence [9] is adopted. According to idea of Butler and Pearson [34] the composite nuclear particles are composed as follows:

(i) The nucleon which is at the surface of the nucleus and its energy is sufficient for its emission is treated as a leading nucleon. It is assumed that such a leading nucleon can attach nucleons which were placed close to its path toward the surface. Particles present at the distance D from surface are considered as a candidates for a cluster members. D is is defined as follows:

$$D = R_0 + h \tag{2.22}$$

where R_0 is the half-density radius of the target nucleus and h is a parameter. The attached nucleons have to be sufficiently close each to other in the phase space, i.e.

$$r_i, [i-1]p_i, [i-1] \leq h_0\left(A_{cl}\right) \text{ for } i = 2, 3, ..., A_{cl}, \tag{2.23}$$

The symbols $r_i, [i-1]p_i, [i-1]$ represents spatial and momentum Jacobian coordinates of the i-th nucleon. The A_{cl} is mass number of the cluster and $h_0\left(A_{cl}\right)$ is a selected radius of the phase-space sphere delimitation assumed for the cluster of the given mass number A_{cl}. For the clusters foreseen in INCL the $h_0(A_{cl})$ parameter takes the following values:

$$h_0(A_{cl}) = \begin{cases} 424 \text{ fm MeV/c} & \text{for } A_{cl} = 2 \\ 300 \text{ fm MeV/c} & \text{for } A_{cl} = 3 \\ 300 \text{ fm MeV/c} & \text{for } A_{cl} = 4 \\ 359 \text{ fm MeV/c} & \text{for } A_{cl} > 4 \end{cases} \tag{2.24}$$

(ii) Among the possible candidates of clusters with mass number A_{cl} for various composition the one of the largest binding energy is selected for the emission. For this purpose minimal value of function ν is searched for, where ν is defined as:

$$\nu = \left(\sqrt{s} - \sum m_i\right) A_{cl} - B_{cl}/A_{cl} \tag{2.25}$$

Here $\sqrt{s}$ and B_{cl} are the total energy of the cluster and its binding energy, respectively.

(iii) Such constructed and selected cluster has to satisfy the emission criterion in respect to its kinetic energy. Kinetic energy of cluster T_{cl} has to be sufficient to allow him to escape from the nucleus, i.e.

$$T_{cl} = \sum_{i}^{A_{cl}} (T_i - V_i) - B_{cl} > 0, \tag{2.26}$$

where T_i and V_i are the kinetic energy and potential of the $i - th$ nucleon, respectively.

(iv) The cluster cannot be emitted too tangential to the surface of the nucleus. It is required that the angle θ between direction of cluster

emission and outward radial direction passing through the center of mass of the cluster fulfills the following condition:

$$\cos\theta > 0.7 \tag{2.27}$$

(v) If all the above mentioned tests are successful then cluster is emitted with the kinetic energy of T_{cl}. Otherwise only the leading nucleon is probed for the emission.

(vi) Emitted clusters of the short life time ($< 1ms$) are forced to decay isotropically.

Duration of cascade

The stopping time, t_{stop} (given in fm/c), of the cascade is determined by the model itself. It is dependent on the mass of the target nucleus, A_T, and calculated with the formula:

$$t_{stop} = 29.8 \cdot A_T^{0.16} \tag{2.28}$$

This formula were optimized in the course of development of INCL. Such calculated duration of cascade assures that the thermal equilibrium in the remnant of the target nucleus has been attained.

Conservation laws

The following conservation laws are followed in the INCL++ model:

$$A_P + A_T = A_{ej} + A_{rem} \tag{2.29}$$
$$Z_P + Z_T = Z_{ej} + Z_\pi + Z_{rem} \tag{2.30}$$
$$T_{lab} = K_{ej} + W_\pi + E_{rec} + E^*_{rem} + S \tag{2.31}$$
$$\vec{P}_{lab} = \vec{P}_{ej} + \vec{P}_\pi + \vec{P}_{rem} \tag{2.32}$$
$$\vec{\ell} = \vec{\ell}_{ej} + \vec{\ell}_\pi + \vec{\ell}_{rem} + \vec{\ell^*} \tag{2.33}$$

The meaning of symbols for equations 2.29 - 2.33 are defined in table 2.1. The still not defined symbols are as follows: E^*_{rem}, $\vec{\ell^*}$ - excitation energy and intrinsic angular momentum of remnant, respectively. E_{rec} and S are total recoil energy and total separation energy of nucleons, respectively.

Symbol meaning	Subscript meaning				
	Ejectile (ej)	Pions (π)	Remnant (rem)	Target (T)	Projectile
Mass A	A_{ej}		A_{rem}	A_T	A_P
Charge Z	Z_{ej}	Z_π	Z_{rem}	Z_T	Z_P
Kinetic energy	K_{ej}				T_{lab}
Total energy		W_π			
Momentum P	P_{ej}	P_π	P_{rem}		P_{lab}
Angular Momentum $\vec{\ell}$	$\vec{\ell}_{ej}$	$\vec{\ell}_\pi$	$\vec{\ell}_{rem}$		$\vec{\ell}$

Table 2.1: Symbols meaning for equations 2.29 - 2.33

2.1.2   Quantum Molecular Dynamics (QMD) Models

The so-called Quantum Molecular Dynamics (QMD) is used not only in nuclear physics but also in other fields of physics or chemistry. It is applicable for description of the problems where examined phenomena can be described as time evolution of n-body quantum system.

In nuclear physics it is used to describe the evolution of the nuclear system undergoing the collision. It is applicable both to heavy ion collisions as well to much simpler collision of the proton with nuclei.

Initial ground states of the colliding systems are reproduced with great care. Each nucleon is described with its wave function. Pauli principle is observed strictly. The Hamiltonian of the studied system is carefully constructed and has components describing the potentials, possible interactions and the symmetry energy term.

There are many version of QMD models depending on their specific application. In this thesis the so-called Ultra relativistic Quantum Molecular Dynamics (UrQMD) [12] model is used. In following it is described in more details.

Ultra Relativistic Quantum Molecular Dynamics (UrQMD)

In relativistic application of quantum molecular dynamics model the energy limits are extended to relativistic energies. This requires the collision term containing heavy baryon-resonances, strange particles and string-excitation for high energy hadron-hadron interactions.

Intialization

Initial positions and momenta of nucleons in the ground state of target nucleus are sampled iteratively as long as the demanded shape of density distribution and the required phase space density are obtained. Pauli exclusion principle is checked for the resulting fermion distributions after each iteration of sampling.

The nucleons of a target (but also the projectile and the produced later particles) are represented as Gaussian wave packets, $\varphi(x_j, t)$:

$$\varphi(x_j, r_i, p_i, t) = \left(\frac{2\alpha}{\pi}\right)^{3/4} \exp\left\{-\alpha(x_j - r_i(t))^2 + \frac{i}{\hbar}p_i(t)x_j\right\} \qquad (2.34)$$

In above equation x_i is the spacial coordinate of nucleon, r_j and p_j are the three-dimensional time dependent space and momentum parameters of the Gaussian function, respectively, and α is a parameter given in table 2.2.

The wave function of the whole nucleus is defined as a product of wave functions of all nucleons and given by:

$$\phi = \prod_j \varphi_j(x_j, r_i, p_i, t) \qquad (2.35)$$

For the whole target nucleus the following conditions have to be fulfilled:

1. $\sum_i r_i = 0$, i.e. it is centered in space around 0.

2. $\sum_i v_i = 0$, i.e nucleus at rest state.

   Where r_i is position and v_i velocity vector of particle i.

3. The binding energies of nuclei should be equal to binding energies given by the Bethe-Weizsäcker formula.

4. The mean radius of nucleus should follow the mass dependence:

$$R(A) \approx r_0 A^{1/3} \qquad (2.36)$$

   where r_0 is calculated with equation:

$$r_0 = \left(\frac{3}{4\pi\rho_0}\right)^{1/3} \qquad (2.37)$$

   in which ρ_0 is a ground state density.

5. All nucleons of nucleus should be in ground states

The initial momenta of nucleons are sampled randomly from 0 to maximal Fermi-momentum p_F calculated separately for protons and neutrons:

$$p_F = \hbar c \left(3\pi^2 \rho\right)^{1/3} \tag{2.38}$$

where ρ corresponds to proton or neutron density.

Potentials

Sum of two body and three body Skyrme, Yukawa and Coulomb potentials, are used in the UrQMD model.

The nuclear potentials are parametrized with the effective Skyrme interaction.

The two body Skyrme potential of particle j is given by equation:

$$V_j^{Skyrme2} = t_1 \sum_k^N \left(\frac{2\alpha}{\pi}\right)^{\frac{3}{2}} \exp\left\{-\alpha(r_j - r_k)^2\right\} = t_1 \varrho_j^{int}(r_j) \tag{2.39}$$

whereas the three body one for particle j, l, k is calculated with the use of formula:

$$
\begin{aligned}
V_j^{Skyrme3} =\, & t_2 \frac{1}{2!} \sum_k^N \left(\frac{4\alpha^2}{3\pi^2}\right)^{\frac{3}{2}} \\
& \exp\left\{-\frac{2}{3}\alpha\left((r_j - r_k)^2 + (r_k - r_l)^2 + (r_l - r_j)^2\right)\right\} \\
=\, & t_\gamma(\gamma + 1)^{-3/2}(\varrho_j^{int})^\gamma
\end{aligned}
\tag{2.40}
$$

The values of parameters t_1, t_γ and α are given in table 2.2. The value of γ is 2. The r_j represents position of particles.

The Yukawa, Coulomb and Pauli potentials are given by following equations:

$$V_{Yukawa}^{ij} = V_0^{Yuk} \frac{\exp\left\{|r_i - r_j|/\gamma y\right\}}{|r_i - r_j|} \tag{2.41}$$

$$V_{Coulomb} = \frac{Z_i Z_j e^2}{|r_i - r_j|} \tag{2.42}$$

$$V_{Pau}^{ij} = V_{Pau}^0 \left(\frac{\hbar}{p_0 q_0} \right)^3 \exp \left\{ -\frac{|r_i - r_j|^2}{2q_0^2} - \frac{|p_i - p_j|^2}{2p_0^2} \right\} \delta_{\tau_i \tau_j} \delta_{\sigma_i \sigma_j} \qquad (2.43)$$

The values of parameters V_0^{Yuk}, V_{Pau}^0, γy, p_0 and q_0 are given as well in table 2.2. The symbol σ_j and τ_j represents spin and isospin of particle j of charge Z_j and e is the electron charge.

Usage of the Pauli potential in the model is optional.

Table 2.2: List of parameter values used in equations of potentials (Skyrme-type potential, Yukawa, Coulomb and Pauli potential) with and without Pauli potential

Parameter	Unit	Without Pauli potential	With Pauli potential
α	fm^{-2}	0.25	0.1152
t_1	MeV fm^3	-7264.04	-84.5
t_γ	MeV fm^6	87.65	188.2
γ		1.676	1.46
V_0^{yuk}	MeV fm	-0.498	-85.1
γy		1.4	1.0
V_0^{Pauli}	MeV	$-$	98.95
q_0	fm	$-$	2.16
p_0	MeV/c	$-$	120

Particle propagation and collisions

Constituents of the colliding system are moving according to the classical equation of motion. Their positions and momenta are calculated at the user selected time steps.

Collisions among the particles are probed stochastically (in the similar way, as in described above INCL++ model). Two particles can collide if their mutual distance in 3-dimensional space d_{trans} fulfills the relation:

$$d_{trans} \leq \sqrt{\frac{\sigma_{tot}}{\pi}} \qquad (2.44)$$

where σ_{tot} is the total reaction cross-section interpreted geometrically as an area. σ_{tot} depends on the type of colliding particles and their total center of mass energy $\sqrt{s}$.

Cross-sections and reaction channels

Although it is not fully applicable for the energy range and for the reactions studied in this thesis it is worth to mention that in the UrQMD model production or excitation of 55 baryon species including nucleons, Deltas and hyperons is considered (see table 2.3). Production of 32 different mesons (see table 2.4) is implemented as well. All their corresponding anti-particles and all isospin-projected states are taken into account.

For utilisation in the UrQMD model the available nucleon-nucleon or pion-nucleon cross-sections measured in the vacuum are parametrized. It is similar as for other described here models of the first step of spallation reaction. Isospin symmetry is used when possible in order to reduce the number of parameterized or tabulated individual cross-sections.

Table 2.3: List of particles included in the hadronic cascade

Nucleon	Delta	Lambda	Sigma	Xi	Omega
N_{938}	Δ_{1232}	Λ_{1232}	Σ_{1192}	Ξ_{1317}	Ω_{1672}
N_{1440}	Δ_{1600}	Λ_{1600}	Σ_{1385}	Ξ_{1530}	
N_{1520}	Δ_{1620}	Λ_{1620}	Σ_{1660}	Ξ_{1690}	
N_{1535}	Δ_{1700}	Λ_{1700}	Σ_{1670}	Ξ_{1820}	
N_{1650}	Δ_{1900}	Λ_{1900}	Σ_{1775}	Ξ_{1950}	
N_{1675}	Δ_{1905}	Λ_{1905}	Σ_{1790}	Ξ_{2025}	
N_{1680}	Δ_{1910}	Λ_{1910}	Σ_{1915}		
N_{1700}	Δ_{1920}	Λ_{1920}	Σ_{1940}		
N_{1710}	Δ_{1930}	Λ_{1930}	Σ_{2030}		
N_{1720}	Δ_{1950}	Λ_{1950}			
N_{1900}		Λ_{1890}			
N_{1990}		Λ_{2100}			
N_{2080}		Λ_{2110}			
N_{2190}					
N_{2200}					
N_{2250}					

Unfortunately the production of composite nuclear particles is not considered in the UrQMD model.

Table 2.4: Mesons and meson-resonances included into UrQMD, where mesons are categorized as J^{PC}. The symbol J, P, C represents total angular momentum, parity, and charge conjugation.

0^{-+}	1^{--}	0^{++}	1^{++}	1^{+-}	2^{++}	$(1^{--})^{*}$	$(1^{--})^{**}$
π	ρ	a	a_1	b_1	a_2	ρ_{1450}	ρ_{1700}
K	K^*	K_0^*	K_1^*	K_1	K_2^*	K_{1410}^*	K_{1680}^*
η	ω	f_0	f_1	h_1	f_2	ω_{1420}	ω_{1662}
η'	ϕ	f_0^*	f_1'	h_1'	f_2'	ϕ_{1680}	ϕ_{1900}

2.1.3 Boltzmann-Uehling-Uhlenbeck (BUU) models

The classical transport equation developed for gases by Boltzmann was adapted for quantum systems by Uehling and Uhlenbeck [35]. First time this theory was used for description of nuclear collisions by Bertsch in 1984 [36]. The Boltzmann-Uehling–Uhlenbeck (BUU) equation with a self-consistent potential field and with a collision term that respects the Pauli principle is meant in this respect.

The Giessen Boltzmann–Uehling–Uhlenbeck (GiBUU) transport model [11], which grew out of these early studies is a method and simulation code for hadron-, photon-, electron-, neutrino-, and heavy-ion-induced reactions on nuclei. It is based on a coupled set of semi-classical kinetic equations, which describe the dynamics of a hadronic system explicitly in phase space and in time. The initial state of the hadronic system, either directly corresponds to the experimental conditions (meson–nucleus, hadron–nucleus, and heavy-ion collisions) or is obtained via external models (photon–, electron–, and neutrino–nucleus reactions). The relevant degrees of freedom are mesons and baryons, which propagate in the mean fields and scatter according to cross-sections, which are appropriate for the energy range from a few tens of MeV to more than 100 GeV. In the higher energy regimes the concept of pre-hadronic interactions is implemented in order to account for color transparency and formation-time effects.

In general the BUU equation describes the space–time evolution of a many-particle system under the influence of mean-field potentials and a collision term. More precisely, it is the time evolution of the Wigner transform of the real-time one-particle Green's function, which is a generalization of the classical phase–space distribution $f_i(\vec{r}, \vec{p}, t)$.

For each particle species (counted with the index i) an additional dif-

ferential equation is obtained. All these equations are coupled through the gain and loss terms, which represent scattering processes. Collisions undergo according to the differential cross-section $\frac{d\sigma}{d\Omega}$ and the relative velocity of colliding particles i, j: v_{ij}. The mean fields and collision terms are included in the Hamilton functions. The BUU transport equation is written as follows:

$$
\frac{\partial f}{\partial t} + \vec{v_i} \cdot \nabla_r f_i - \nabla_r U \cdot \nabla_p f_i = -\frac{4}{(2\pi)^6} \int d^3 p_j d^3 p_{j'} d\Omega \frac{d\sigma}{d\Omega} v_{ij}
$$
$$
\times \left[f_i f_j (1 - f_{i'})(1 - f_{j'}) - f_{i'} f_{j'} (1 - f_i)(1 - f_j) \right]
$$
$$
\times (2\pi)^3 \delta^3 (\vec{p_i} + \vec{p_j} - \vec{p_{i'}} - \vec{p_{j'}}) \qquad (2.45)
$$

The left side of the above formula describes the propagation of particle i of the velocity $\vec{v_i}$ in the mean nuclear field U. The collision term for the tested particles is on the right side of the equation. The term in square parentheses assure the Fermi-Dirac statistics for fermions. It blocks the interaction when final state conditions do not fulfill the Pauli exclusion principle. The Dirac's delta imposes the momentum conservation.

BUU equation is solved with the use of Monte Carlo technique by simulations of motion of involved particles [37].

Interesting technical feature of the BUU calculations is the way of simulations of the fate of the nuclear system. The real particles are approximated by the test particles. Each of reaction constituent is replaced by n test particles. Number n has to be of the order of 1000.

For creation of the phase space distributions or for calculation of the probabilities of the individual interactions the contributions from all test particles are summed up with appropriate weights.

In the GiBUU version of BUU method the time dependent evolution of the nuclear mean field has a form developed in [38]. The Skyrme potential (first two components of the equation below) is supplemented by a Yukawa term and the Coulomb potential (V_{Coul}):

$$
U(\vec{r}) = A \left(\frac{\rho(\vec{r})}{\rho_0} \right) + B \left(\frac{\rho(\vec{r})}{\rho_0} \right)^{\frac{4}{3}} + V_0 \int d^3 \vec{r} \frac{exp(-\mu|\vec{r} - \vec{r'}|)}{\mu|\vec{r} - \vec{r'}|} \rho(\vec{r}) + V_{Coul} .
$$
$$
(2.46)
$$

Coefficients A and B represent the attractive and repulsive part of the potential whereas the ρ_0 and ρ are ground state and current nuclear densities, respectively.

The selected parameters are as follows: $A = -141.62$ MeV, $B = 165.23$ MeV, $V_0 = -378$ MeV, $\mu = 2.175$ fm^{-1}, $\rho_0 = 0.168$ fm^{-3}.

Depending on the energy range of simulated reaction the relativistic or non-relativistic forms of mean-field potentials are foreseen.

In the GiBUU the initial spatial distribution of target nucleons has a shape of Woods-Saxon distribution:

$$\rho(r) \; = \; \frac{\rho_0}{1 \; + \; exp(\frac{r-R_0}{a})} \; , \tag{2.47}$$

with $\rho_0 = 0.168$ fm^{-3}, R $= 1.124$ A$^{1/3}$ fm and a $= 0.025$ A$^{1/3} + 0.29$ fm.

The initial momentum distribution of target nucleons is dependent on the spatial density distribution. It must be isotropic and homogeneous within the maximal Fermi momentum sphere of the radius $p_F(r)$:

$$p_F(r) \; = \; \left(\frac{3\pi^2\rho(r)}{2}\right)^{1/3} \; . \tag{2.48}$$

During simulation of the collision the particles move along straight lines according to their current momentum and field strength. The classical equations of motion are used for this purpose.

Interactions are probed if the shortest distance of two particles is smaller than that determined from the geometrical cross-section $\sqrt{\sigma_{tot}/\pi}$. Production and decay of nuclear resonances are included.

2.2   Problem of emission of complex particles

Mechanisms responsible for creation of composite nuclear products during first step of proton-nucleus or nucleus-nucleus collision are in fact not known. Various hypotheses are proposed and tested in this respect (see e.g. [39–44]).

It is commonly assumed that the source of light composite particles in the low and middle energy pA reactions is a coalescence mechanism.

Clusters could be created dynamically via surface coalescence still during the intranuclear cascade, as it is proposed in INCL++ model (c.f. chapter 2.1.1). In this way the dynamical construction of the composite particles of the masses $A \leq 8$ is possible [9]. The emission energies and momenta result from the energies and momenta of composing nucleons. Their binding energies and the relevant height of the Coulomb barrier are taken into account.

Unfortunately, both the GiBUU as well as the UrQMD models do not contain up to now the mechanisms permitting the simulation of creation and emission of nuclear clusters. Traditionally, in kinetic transport models, the formation of stable clusters is tried to be described by their coalescence but in the final states - it means after single nucleons were emitted from the target nucleus. The so-called afterburner methods are used. The conditions for the mutual distances in phase space of emitted nucleons are applied. In heavy-ion collision the coalescence is applied after so-called freeze-out moment [45–48].

Such methods however do not contribute to the dynamics of the first step of spallation reaction and are not considered in this thesis.

Promising and more theoretically advanced approaches are under development for the other version of QMD called PHQMD [49] and SMASH [50] models.

The origin of composite nuclear particles is also intensively studied and discussed in heavy ion collisions at very high energies. For the recent results see e.g. [51, 52].

2.3 Models describing the emission from equilibrated remnant

2.3.1 Generalized Evaporation Model - GEM2

The Generalized Evaporation Model (GEM2) model was developed by S. Furihata [23, 24]. It uses the statistical description of the excited remnant nucleus of first stage of reaction. The de-excitation of residual parent nuclei i of mass A_i, charge number Z_i and excited to energy E_i^* is performed using the evaporation processes.

The Weisskopf-Ewing formula (2.49) provides the probability P_j for the emission of particle j at kinetic energy between $(\varepsilon, \varepsilon + d\varepsilon)$ in center of mass system [53, 54]:

$$P_j(\epsilon) \ = \ g_j \sigma_{inv}(\epsilon) \ \frac{\rho_d(E_i^* - Q - \epsilon)}{\rho_i(E_i^*)} \ \epsilon d\epsilon \ , \qquad (2.49)$$

In the above equation the σ_{inv} is inverse reaction cross-section. ρ_i and ρ_d are parent and daughter nuclei level densities expressed in MeV^{-1}. The symbols S_j and m_j denote the spin and mass of emitted particle j, respectively. The g_j is equal to $2(S_j + 1) \cdot m_j/\pi^2\hbar^2$.

After emission of particle j of mass A_j and charge Z_j the remaining nucleus becomes the daughter nucleus d with mass A_d and charge Z_d.

The inverse reaction cross-section is calculated according to:

$$\sigma_{inv}(\varepsilon) = \sigma_g\alpha(1 + \frac{\beta}{\varepsilon}) \equiv \begin{cases} \sigma_g c_n(1 + b/\varepsilon) & \text{for neutrons} \\ \sigma_g c_i(1 + V/\varepsilon) & \text{for charged particles} \end{cases} \tag{2.50}$$

where:

σ_g - geometric cross-section;

c_n, c_i, b - parameters (cf. [23, 24]);

V - height of the Coulomb barrier.

The decay width Γ_j is calculated with the use of equation:

$$\Gamma_j = \frac{g_j \sigma_g \alpha}{\rho_i(E)} \int_V^{E-Q} \varepsilon\left(1 + \frac{\beta}{\varepsilon}\right)\rho_d\,(E - Q - \varepsilon)d\varepsilon \tag{2.51}$$

obtained by integrating of equation 2.49 and with the use of equation 2.50.

In the GEM2 Monte Carlo simulation, type of emitted particle j is selected according to the probability p_j calculated as:

$$p_j = \Gamma_j / \sum_k \Gamma_k \tag{2.52}$$

where Γ_j is given by equation 2.51 and summation is performed over all possible decay channels k.

Model GEM2 calculates the emission of 66 various nuclides which fulfill the following criteria:

- atomic number $Z \leq 12$;

- exists naturally or it is isotope close to the stability line;

- half-life is larger than 1 ms.

The list of isotopes considered as emission particles in GEM2 model is given in table 2.5.

In the GEM2 model the excited nuclei of the atomic number $Z_i \geq 70$ are probed for fission. The fission competes with neutron emission. The approach of Atchison [55] is used for calculation of fission probability.

The details of GEM2 model are available in [23, 24].

Table 2.5: The table of nuclides which satisfy the emission criteria in the GEM2 model.

Z_j	Isotopes					
0	n					
1	p	d	t			
2	^{3}He	^{4}He	^{6}He			
3	^{6}Li	^{7}Li	^{8}Li	^{9}Li		
4	^{7}Be	^{9}Be	^{10}Be	^{11}Be	^{12}Be	
5	^{8}B	^{10}B	^{11}B	^{12}B	^{13}B	
6	^{10}C	^{11}C	^{12}C	^{13}C	^{14}C	^{15}C	^{16}C
7	^{12}N	^{13}N	^{14}N	^{15}N	^{16}N	^{17}N
8	^{14}O	^{15}O	^{16}O	^{17}O	^{18}O	^{19}O	^{20}O
9	^{17}F	^{18}F	^{19}F	^{20}F	^{21}F	
10	^{18}Ne	^{19}Ne	^{20}Ne	^{21}Ne	^{22}Ne	^{23}Ne	^{24}Ne
11	^{21}Na	^{22}Na	^{23}Na	^{24}Na	^{25}Na	
12	^{22}Mg	^{23}Mg	^{24}Mg	^{25}Mg	^{26}Mg	^{27}Mg	^{28}Mg

2.3.2 Model GEMINI

GEMINI is a statistical model developed first in 1986 by R. Charity [21, 22] to describe complex fragment emission in fusion reaction. In the current version it is a multipurpose model allowing as well the simulation of symmetric fission, the evaporation of light charge particles and many binary decay modes.

The compound nuclei being the results of the various decay modes in the disintegration chain of the parent nucleus are sampled for subsequent decays as long as the probability for γ-decay become dominant or until the remaining excitation energy is insufficient for any another decay mode.

Sequential evaporation

For simulation of the sequential evaporation from excited compound nucleus the excitation energy of parent nucleus, angular momenta of nucleons, rotation energy and deformation of the parent nucleus are taken into account.

The decay widths Γ for different modes are calculated. Depending on the charge of emitted particles various formalisms are used for this aim. For $Z \leq 4$ the Hauser-Feshbach approach is is utilized [56]. For $Z > 4$ the formalism

developed by Moretto [57] is applied. In the Hauser-Feshbach method the angular momenta of the initial and final states are taken into account.

For example, in case of evaporation of particle i of the $Z \leq 2$ from the compound nucleus excited to energy E^* and having spin S_{CN} the decay width is calculated according to formula:

$$\Gamma_i^{HF} = \frac{1}{2\pi \rho_{CN}\left(E^*, S_{CN}\right)} \int d\varepsilon \sum_{S_d=0}^{\infty} \sum_{J=|S_{CN}-S_d|}^{S_{CN}+S_d} \sum_{l=|J-S_i|}^{J+S_i} T_l(\varepsilon)\rho_d\left(E^* - B_i - \epsilon, S_d\right)$$
(2.53)

where ℓ, J, S_i, are orbital, total and spin momenta of evaporated particle, respectively. S_d is the spin of the daughter nucleus. ε and B_i are kinetic and separation energies of evaporated particles, respectively. The symbols ρ_d and ρ_{CN} represent the level densities of daughter and parent compound nuclei, respectively. $T_l(\epsilon)$ is the transmission coefficient.

The demanded level densities are calculated in the framework of the Fermi gas model:

$$\rho(U, J) = (2J + 1) \left[\frac{\hbar^2}{2\xi}\right]^{3/2} \frac{\sqrt{a}\ exp(2\sqrt{aU})}{12\ U^2} \ ,$$
(2.54)

In the above formula the ξ is the moment of inertia of daughter nucleus, a is level density parameter equal to $A/8.5\ MeV^{-1}$ and U is the thermal excitation energy.

The angular distributions of the evaporated particles are sampled according to the absolute values of the Legendre functions:

$$\frac{dN}{d\Omega} = \left|P_\ell^\ell\left(\cos\theta\right)\right|$$
(2.55)

Fission and complex fragment emission

For these decay modes the Bohr-Wheeler transition-state decay width for symmetric fission is calculated:

$$\Gamma_{BW} = \frac{1}{2\pi \rho_{CN}\left(E^*, S_{CN}\right)} \int \rho_{sp}\left(E^* - B_f\left(S_{CN}\right) - \varepsilon\right) d\varepsilon$$
(2.56)

where ρ_{sp} and $B_f(S_{CN})$ are the level-density and spin-dependent energy at saddle-point, respectively, and ε is the kinetic energy of fragment.

Gamma-ray emission

For very low excitation energies, the partial decay widths for particle and γ decay are comparable. Thus, for such low excitation range it is important to include the gamma-ray emission as well.

The Blatt and Weisskopf equation is used for this purpose, which provides the value of the γ decay width for multipolarity l:

$$\Gamma_\gamma^l = F_l \frac{18(l+1)}{l(l+3)^2[(2l+1)!]^2} \frac{e^2}{\hbar c} \left(\frac{R}{\hbar c}\right)^{2l} \frac{1}{D_0} \sum_{s_d=|S_{CN}-l|}^{S_{CN}+l} \int \varepsilon \frac{\sigma(E*-\varepsilon, S_d)}{\sigma(E*, S_d)} d\varepsilon$$

$$(2.57)$$

Where $R = 1.2A^{1/3}$fm , D_0 is 1 MeV, ε is the gamma-ray energy and F_l is deviation from the Weisskopf estimates. The values of $F_1 = 0.0025$ and $F_2 = 9.0$ are taken from the ref [58].

The GEMINI model is used for various types of nuclear reactions. The specific applications and details of applied mathematical methods are available in [22].

2.3.3 Statistical Multi-fragmentation Model - SMM

The SMM model of Bondorf et al. [25] is rather a framework composed of more specific models relevant to simulation of the fate of the excited system according to its current conditions.

In the SMM the purely statistical treatment of the excited system is used. The thermodynamical formalism is applied with consideration of microcanonical, canonical and macrocanonical statistical ensembles. Their temperature, entropy and free energy are taken into account.

The specific channel j of nucleus de-excitation is selected according to its probability W_j calculated as an exponent of its entropy S_j:

$$W_j \propto \exp(S_j) \tag{2.58}$$

Entropy S_j depends on the number of fragments, excitation energy, mass, charge and freeze-out volume of the system. The decaying system attains the freeze-out volume when the nuclear forces between its constituents can be neglected and only electromagnetic interaction needs to be taken into account.

SMM model works in broad range of excitation energies E^* of the excited nuclei. The mode of their disintegration depends on the actual value of E^* or the system temperature.

At low temperatures where ($E^* < 5$ MeV/nucleon) the decay scheme is similar like in the case of evaporation - single large remnant and a few fragments of low masses are foreseen.

With increase of excitation energy the momentary thermal equilibrium of the system after the cluster emission could be not attained. Thus, the sequential evaporation becomes less probable and more violent processes are feasible. The excited system can break-up simultaneously into a few heavier fragments, which is referred as mulifragmentation.

The onset of mulifragmentation is predicted when the excitation energy E^* of the system attains ≈ 5 MeV/nucleon. It is characterized by the observation of a few intermediate mass fragments which are accompanied with more fragments of the low masses.

Further increase of the temperature results in increase of the number of fragments and decrease of their average masses.

At still higher excitation energies exceeding 10 - 15 MeV/nucleon the vaporization process is foreseen. It consists of simultaneous disintegration of the excited nucleus into nucleons and lightest nuclear clusters.

For heavy nuclei the competing process like the fission is also considered. The fate of the decay products in SMM model is controlled as well. If they are themselves excited compound nuclei their further disintegration is simulated.

For the detailed descriptions of implemented codes in the framework of SMM model and information about the parameters see [25, 59, 60].

2.3.4 Model ABLA07

In the ABLA07 model the sequential evaporation processes, the simultaneous breakup, and the fission processes are considered for the disintegration of the excited and thermalized nuclear system. The parameter, which governs the selection of the decay mechanism is the excitation energy E^*_{res} per nucleon of the residual nucleus of mass A_{res}, marked as ε_{res}:

$$\varepsilon_{res} = E^*_{res}/A_{res} \tag{2.59}$$

For excitation energy such that $\varepsilon_{res} < 4.2$ MeV/nucleon (the so-called $\varepsilon_{freezeout}$) the nucleus evaporates the light particles or undergoes the fission.

Otherwise, the simultaneous break-up is simulated.

The Weisskopf-Ewing formalism, which as in other models is used for calculation of probability of particle evaporation (cf. GEM2 model in sub-section 2.3.1), in ABLA07 model is extended by taking into consideration the angular momenta of the involved particles during the evaporation. It is done by random sampling (from Gaussian distribution) of the change of angular momentum when evaporation takes place.

Similarly as in GEM2 model the height of Coulomb barrier and the level densities are calculated. But in ABLA07 additionally the thermal expansion of the excited nucleus is taken into account.

For excited nuclei of high masses the probability of fission is calculated as it is described in [20].

For the breakup process occurring when $\varepsilon_{res} > \varepsilon_{freezeout}$ (4.2 MeV/nucleon) it is assumed that the excitation energy excess over the $\varepsilon_{freezeout}$ is used to produce the light fragments. From experimental parametrization the energy needed for emission of a 1 mass unit is known. From this fact the mass of the remaining heaviest fragment can be calculated. It is also assumed that the heaviest fragment has the same A/Z ratio as the parent nucleus. In this way the heaviest fragment is established. The rest of the mass is distributed according to the formula:

$$\frac{d\sigma}{dA_{LF}} \propto A_{LF}^{-\tau} \tag{2.60}$$

where A_{LF} is the mass number of fragments lighter than the heaviest one and the exponent τ is ~ 2.

The charges of the lighter fragments Z_{LF} are sampled from the Gaussian distribution of the mean value calculated according to the assumption of A/Z conservation and standard deviation of the fixed value calculated as:

$$\sigma_{Z_{LF}}^2 = \frac{5.5 MeV}{14.0 MeV} = 0.3929 \tag{2.61}$$

The method of calculation of kinetic energies of fragments depends on the ability of the system to attain the thermal equilibrium before the dis-integration. If the breakup occurs too fast (below 100 fm/c) the momenta of the decay products reflect the Fermi motion of nucleons in the decaying

system. Then the distribution of momenta of fragments is sampled using the Fermi-gas model. For the long-timescale process sufficient for thermalization of the system before its disintegration the thermal motion of fragments inside the breakup volume have to be considered.

The composite fragments of the breakup of the masses greater than $A = 4$ are checked for their excitation energy and could be probed for the further decay.

The details of the ABLA07 model are available in ref. [20].

Chapter 3

Mechanisms of proton-nuclear target interaction - studies with HADES spectrometer

In the present and in the following chapters the mechanisms of the production of fast particles emitted anisotropically in the laboratory reference frame will be discussed. According to the hypothesis that the reaction proceeds in two steps these particles are produced in the initial phase of the collision. Their distributions reflect the dynamics of the intranuclear cascade and the mechanisms acting in this reaction stage.

For this aim the reaction of the $p + {}^{93}Nb$ at 3.5 GeV proton beam energy has been studied in details. The raw data collected by the HADES Collaboration [61–67] in GSI Darmstadt have been used.

In the following the HADES detection system is presented. Also the methods used for data selection, particle identification and normalization of the resulting distributions are described.

The HADES detection system has been upgraded a few times in the last two decades. In this thesis the description of the experimental apparatus is given as it was in year 2008 when the data used here were collected. Moreover, the presentation of the apparatus will be restricted only to these parts of detection system which were utilized for registration of the particles of interest of the current study, namely charged pions and isotopes of hydrogen.

3.1   Description of experiment

The High Acceptance Dielectron Spectrometer HADES is installed in Heavy
Ions Research Laboratory (GSI) Darmstadt, Germany. It was constructed in
order to perform the research with proton and heavy ion beams. Later also
the pion beams have been used. The beams collide with the fixed targets,
which can be the solid material or the liquid. The HADES detection system
permits for registration of dileptons, mesons and barions and creation of their
energy and angular distributions.

The general view of the HADES apparatus is shown in fig. 3.1
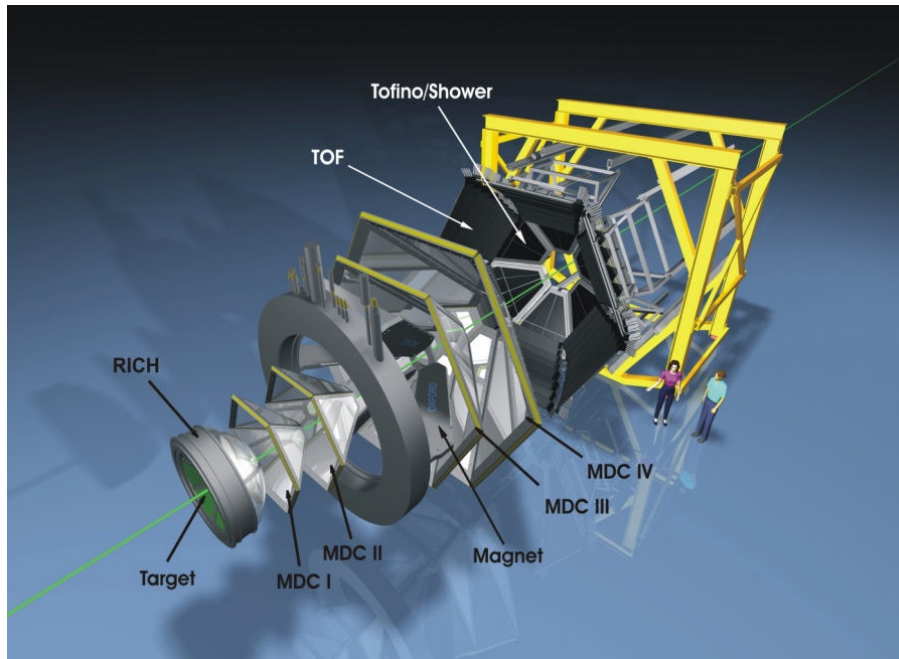
Figure 3.1: The schematic diagram showing HADES detector system. The
subsystems - RICH, MDC, TOF/Tofino, Shower are composed of 6 construc-
tionally equivalent sectors placed symmetrically around the beam axis. Such
solution permits the full coverage (360°) of the azimuthal angle. The accep-
tance in the polar angle is assured for $18° < \theta < 85°$.

In the HADES experiment the stationary targets are used. This fact
creates the need to extend the detection apparatus towards forward emission
angles in the laboratory reference frame. HADES detection system has full
symmetry along the azimuthal detection angle.
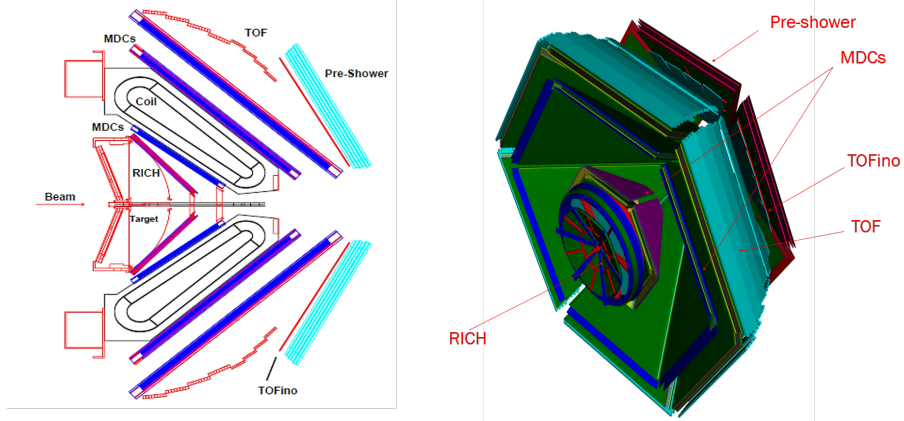
Figure 3.2: The cross-section of the HADES apparatus used for measurement
of $p + Nb$ reaction at 3.5 GeV. The most important detection subsystems for
registration of π^+, π^-, p, d, and t, are the Multiwire Drift Chambers (MDC)
and TOF/Tofino scintillating walls. MDC are the tracking detectors. They
provide also the information about the specific energy losses of particles.
Scintillators measure as well the energy losses but they work also as triggering
detectors. The momenta of particles are measured with the use of magnetic
field of a superconducting magnet. The toroidal magnet is installed between
the pairs of MDCs.

The target system is embedded by the construction of the Ring Imaging
Cherenkov detector (RICH) used for detection of leptons. For registration
of charged hadronic reaction products the set of Multiwire Drift Chambers
(MDC) and the scintillating walls called TOF and Tofino are utilized. Elec-
tromagnetic calorimetry is performed by the electromagnetic shower detector
installed at the end of detection system. Each of the detection subsystem
is composed of 6 equivalent sectors placed symmetrically in respect to the
beam axis.

In the HADES experiment the registration and identification of π^+, π^-,
p, d, and t created in the target is performed by the set of Multiwire Drift
Chambers (MDC) and the TOF/Tofino scintillating walls. The momenta of
particles are analyzed by magnetic field created by toroidal superconducting
magnet. The cross-section of HADES apparatus used for measurement of
$p + Nb$ reaction at 3.5 GeV is shown in fig. 3.2.

3.1.1 Target

The solid target of ^{93}Nb has been used. It consisted of 12 segments installed
coaxially along the beam axis. The diameter of each segment was equal to
2.5 mm and its thickness was of 0.45 mm. The distances between segments
were equal to 4.5 mm. Such construction of target was optimized in order
to enhance the total luminosity for the dilepton studies. The positioning of
the target in regard to the detection system allowed as well to register the
primary spallation products created in each of segments of the target. Fig.
3.3 shows the distributions of the reconstructed vertices of the charged pions
and H isotopes originated in the $p + Nb$ run. The continuous distribution
of vertices covering actual target position between -60 and 0 mm is visible.
Due to limited precision of position measurements and tracking the individual
target sectors cannot be resolved.
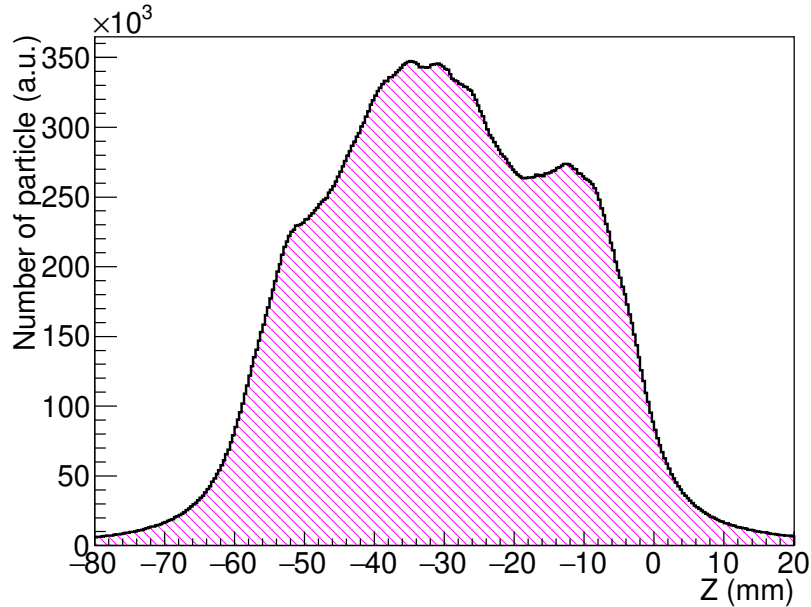
Figure 3.3: Distribution of track vertices of reconstructed primary charged
pion and H isotopes emitted during experiment in which 3.5 GeV protons
bombarded Nb target. Distribution covers the range of the segmented target
position along the beam axis. Contributions from individual segments of
target are not resolved.

3.1.2   Multiwire Drift Chamber

The tracking system of HADES is constructed from 24-trapezoidal Multiwire
Drift Chambers (MDC). They are arranged symmetrically in ϕ angle around
the beam axis. Each individual detection sector consists of 4 modules - two
of them are installed at front of the toroidal superconducting magnet and
two of them behind the magnet. The sizes of the modules increase when
proceeding to the forward direction.

The individual drift chamber (one module) is constructed of six layers.
The angular orientation of the sense (anode) wires of each layer is different.
The sensing wires are soldered at $+40°$, $-20°$, $+0°$, $-0°$, $+20°$ and $-40°$ with
respect to direction perpendicular to the beam axis. It is shown in fig. 3.4.
The sense wires are made of tungsten which is plated with gold. For MDC
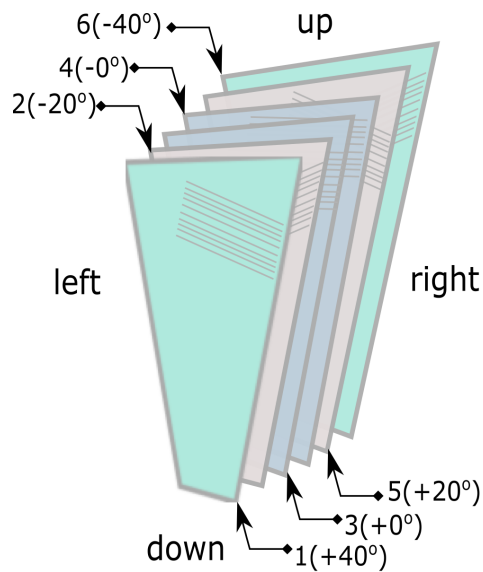
Figure 3.4: Schematic view of the sequence of six layers of each module of
drift chamber and the angular orientation of the sensing wires of each layer.

I-III the thickness of anode wires is 20 μm whereas for the last - IV MDC
the anode wire diameter is 30 μm. Constant mechanical wire tension of 40
cN and 50 cN, respectively, is used.

The cathode wires are made of 80 - 110 μm annealed aluminum (bare -
MDC I-III or gold plated - MDC IV). The exact diameter of cathode wires
increases with the size of chamber. The same concerns the mechanical tension

of cathode wires which varies between 150 cN and 180 cN.

The entrance windows of MDCs are made from $12\mu m$ aluminized Mylar foils.

Chambers were filled with helium-isobutane gas mixture in the proportion of 60:40. They work at atmospheric pressure.

Position resolution of MDC system is ≤ 100 μm in polar angle direction and ≤ 200 μm in azimuthal angle direction. This permits the precise tracking and momentum reconstruction with the resolution of of $\delta p/p = 4\%$.

The effective thickness of the whole set of MDC modules is of 0.5% of the radiation length. Despite of such small thickness the MDCs are able to provide precise information about particle's energy losses. The resolution of the measured energy loss per path length, $\mathrm{d}E/\mathrm{d}x$, is of 7%. The value of energy loss is measured by means of Time over Threshold of the detector signal [68]. The distributions of $\mathrm{d}E/\mathrm{d}x$ vs. *momentum* are crucial for particle identification by means of their specific energy losses.

3.1.3 Superconducting Magnets

The HADES detector comprises 6 coils of superconducting magnets surrounding the beam axis - one coil per one sector. The coils are kept in the individual vacuum chambers. Each coil can generate the maximum field of 3.6 T. The magnetic filed of each sector was mapped with the use of a Hall probe and a devoted optical positioning system.

3.1.4 TOF/Tofino

The TOF and Tofino detectors despite of their names were not used for Time-of-Flight measurement. In the measurement of the $p + Nb$ reaction the START detector installed in vicinity of the target could not be operated. For this reason the TOF and Tofino scintillating walls were utilized as a trigger and energy detectors. Since they are able to provide quite precise information about energy losses of registered particles this advantage has been utilized in this work in order to enhance the effectiveness of particle identification.

The TOF scintilating wall covers the θ angular range from 44° to 85°. Each sector comprises 8 modules of TOF detector. Each such detector consists of 8 strips of plastic scintillator. The thickness of the strips depends on their angular position and varies between 20 and 30 mm. The time resolution of TOF scintillators is equal to 150 ps. Their position resolution is equal to

3 cm. This results in the excellent dE/dx resolution of the TOF detector of
4%.

The Tofino scintillating plastic paddles cover the gap between $18°$ and
$45°$ of θ angle. There are only 4 individual detectors per one sector. Signals
of these detectors are readout only at one side of the paddle. This results in
the worse timing and energy resolution of Tofino walls than in case of TOF
detector. They are equal to 420 ps and 8% respectively. The double hit
resolution of Tofino is worse than this of TOF as well.

3.1.5 Triggering

Data Acquisition System (DAQ) in HADES experiment records the data in
the event-by-event regime. During the collection of the data from $p + Nb$
reaction at 3.5 GeV the two independent sequences of signals triggered the
(DAQ).

- The first trigger aimed in selection of hadronic reaction products. It
  required a signals of at least 3 charged particles were registered in TOF
  and/or TOFino detectors.

- The second trigger was constructed for identification of dileptons. The
  triggering condition were fulfilled if two electron signatures have been
  identified in the RICH detector.

Only the first trigger was sensitive for signals from charged pions and H
isotopes. Thus, only this trigger condition is important for the goal of the
present experiment. In the following always the first type of trigger is meant
when the term "trigger" is recalled.

3.1.6 Software tools for tracking and simulation of detector response

The acceptance of the total and each of the sub-detection systems is simulated
by the HGeant [69] which is a based on GEANT3 [70] simulation package from
CERN. The full geometry, correct material budget and an accurate magnetic
field map are included. Emulation of signal digitization is implemented as
well.

The simulation of response of of the detection system including the trigger conditions, the tracking algorithms, energy losses, efficiencies and demanded calibrations is provided by the HYDRA framework (Hades sYstem for Data Reduction and Analysis) [71], based entirely on the C++ class package ROOT [72].

The initialization of the apparatus geometry and setting of the calibration parameters are possible from an Oracle database and/or from the ROOT files.

The tracking algorithms of HADES take into account the mapped magnetic field of toroidal magnet. The reconstruction of the particle trajectories in the tracking system of HADES is accomplished in several steps as described below:

1. The tracking algorithm demands hits in the MDC cells located in two inner modules and in two outer ones. The centers of the cells create a four points in the space. Out of them the two track segments for inner and outer MDC modules are created. It is checked if they can be matched together within one detection sector at the so called "kick plane" as shown in figure 3.5.

2. For all tracks the outer track segments must match with relevant hit positions in the TOF or Tofino and the Pre-Shower detectors.

3. For identification of tracks created by electrons (not applicable in this work) the inner track segments are matched also with rings in the RICH detector.

4. For such track candidate the precise hit positions within the MDC cells are calculated with the use of drift time information and careful calibrations of position-drift time dependence.

5. The precise 3D fitting of the predefined functions describing the particle trajectory (partially in magnetic field) is applied.

The particle momenta are determined from the bending of their trajectories inside the magnetic field. Various algorithms are utilized in this respect ("kick MDC", splin line, Runge-Kutta - for details see section 4.3 in ref [73]).

The Ring Imaging Cherenkov (RICH) detectors and the Pre-shower detectors shown in fig. 3.2 have not been used for the current studies, thus their description is avoided in this thesis. The reader interested in these subsystems is asked to refer to [73].
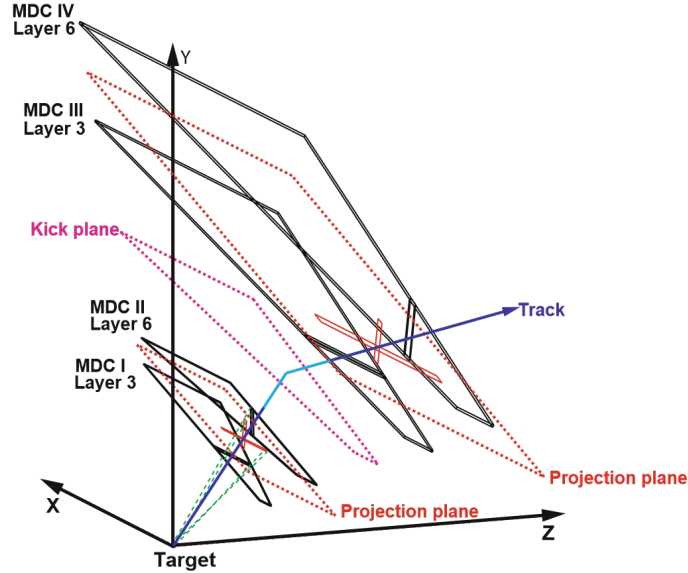
Figure 3.5: Schematic view of track reconstruction using MDC detectors. Only one layer of the MDC detector is shown to simplify the diagram.

3.2 Methodology of data analysis

For the examinations of mechanisms acting during the nuclear spallation and for the developments of accurate theoretical models the precise and possibly most exclusive observables are needed. The simple observables like particle multiplicity or the total production cross-section are less sensitive for details of interplaying mechanisms than e.g. the angular or energy distributions of the reaction products or their coincidences.

Of course, the most demanded would be the experiment allowing for complete registration of all reaction products in 4π geometry and in the whole kinematic range. Unfortunately such experiments are not planned. Thus, taking advantage of the broad acceptance of HADES apparatus and of its magnetic spectrometer it was decided that the double differential cross-sections ($d^2\sigma/d\Omega dE$) will be derived as a first portion of spallation data delivered by HADES experiment.

Three significant difficulties have been encountered when the selection and particle identification (PID) of primary spallation products from $p + Nb$ run at 3.5 GeV reaction have been performed.

1. At least 3 charged particles are demanded in the TOF/Tofino walls

in order to fulfill the trigger condition. This fact implicated that the
purely single distribution spectra were not registered.

2. The origin of triggering particles was disregarded by the trigger system.
It means that both the reaction products originating from the target as
well as the secondary particles created in the parts of apparatus could
contribute to the trigger.

3. Due to missing START detector the Time of Flight (TOF) measure-
ment could not be done. Thus, the PID based on the β value of particles
was significantly reduced. To some extent the particle TOF could be
estimated by comparison to the timing information of the identified
fastest particles contributing to the trigger. But as long as the single
distribution of reaction products are of interest the coincidences with
other particles have to be disregarded. In the present analysis the re-
constructed TOF values were used only for preselection of data. The
lack of actual TOF information significantly reduced the identification
energy ranges for π^+, d and t.

Such problems are not present during identification of leptonic or hadronic
products produced with much smaller cross-sections which are of main inter-
est of the HADES Collaboration.

3.2.1 Particle identification

As mentioned above the identification technique used in this thesis utilizes the
momentum dependency of the specific energy loss per particle path length in
the detector, dE/dx. However, only for the initial - most general definition
of identification cuts the *mass* dependence (calculated from reconstructed
TOF) on *momentum* were utilized.

The scheme of PID was as follows:

1. The *mass* distribution of the registered particles was calculated know-
ing theirs reconstructed TOF. The results in the function of particle
momentum is shown in figure 3.6 - left panel.

2. The *mass* vs. *momentum* distributions is projected onto *mass* axis
and initial slots of *mass* cuts are defined. The results are shown in
figure 3.6 - right panel.
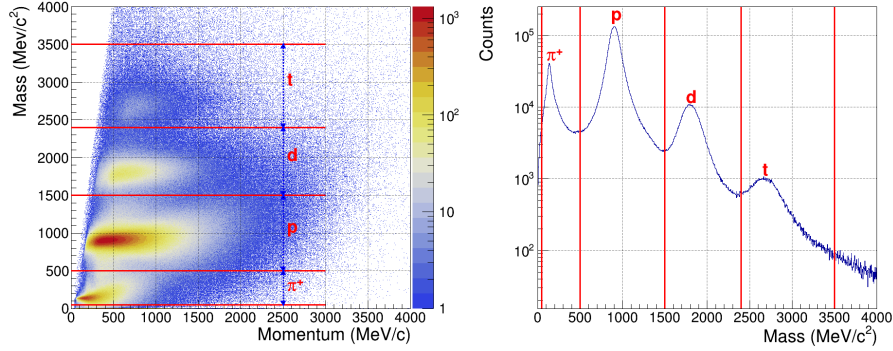
Figure 3.6: *Left panel:* the *mass* vs. *momentum* distribution of registered particles. The *mass* is calculated from the reconstructed TOF value. *Right panel:* projection of distribution of left panel onto *mass* axis.)
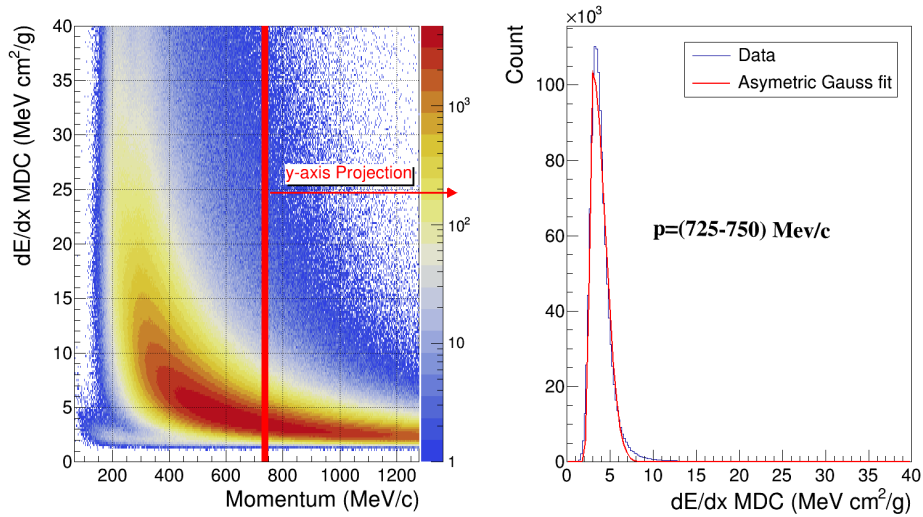
Figure 3.7: *Left panel:* The dE/dx vs. *momentum* distributions for protons registered in MDC. The distribution is created with the use of predefined *mass* cuts (see above). Distribution is divided into bins of the 25 MeV/c width. Slot for 725 - 750 MeV/c is marked with the red color vertical strip. *Right panel:* The projection of proton distribution of 725 - 750 MeV/c momentum bin onto the dE/dx axis. The superimposed distribution given in red color is the asymmetric Gaussian function (cf. formula 3.1).
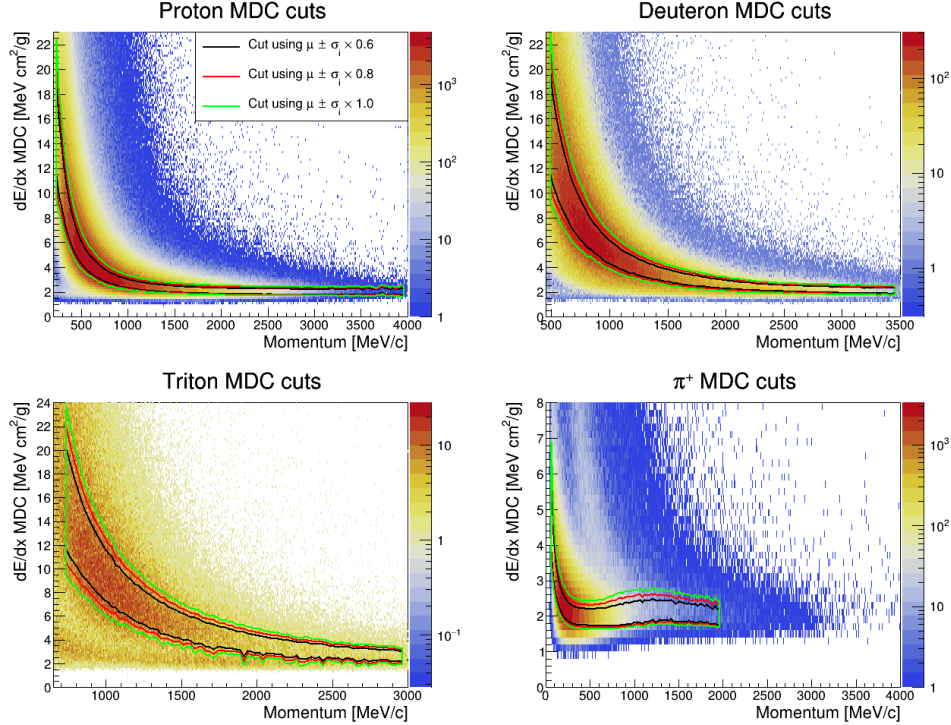
Figure 3.8: The scatter plot of dE/dx vs. $momentum$ for p, d, t and π^+
registered in MDC. The identification cuts of three widths (described above)
are superimposed.

3. Such defined $mass$ cuts are used for creation of dE/dx vs. $momentum$
   distributions for p, d, t, π^+ registered in MDC. The example of such
   scatter plot for protons is presented in fig. 3.7 - left panel.

4. The dE/dx vs. $momentum$ distributions are divided into 25 MeV/c
   $momentum$ bins as indicated in fig. 3.7 - left panel.

5. Part of distribution comprised in each 25 MeV/c $momentum$ bin is
   projected onto the dE/dx axis (cf. fig. 3.7 - right panel where the
   example for protons of the momenta 725 - 750 MeV/c is given).

6. Asymmetric Gaussian function of formula 3.1 is fitted for resulting
   distribution of every 25 MeV/c $momentum$ bin. Example of fitted
   function for protons of the momenta between 725- and 750 MeV/c

is superimposed on the particle distribution in fig. 3.7 - right panel.
Formula for asymmetric Gaussian function:

$$f_g(x) = \begin{cases} \frac{1}{\sigma_l \sqrt{2\pi}} e^{-\frac{1}{2}\left(\frac{x-\mu}{\sigma_l}\right)^2} & x - \mu \leq 0 \\ \frac{1}{\sigma_r \sqrt{2\pi}} e^{-\frac{1}{2}\left(\frac{x-\mu}{\sigma_r}\right)^2} & x - \mu > 0 \end{cases} \tag{3.1}$$
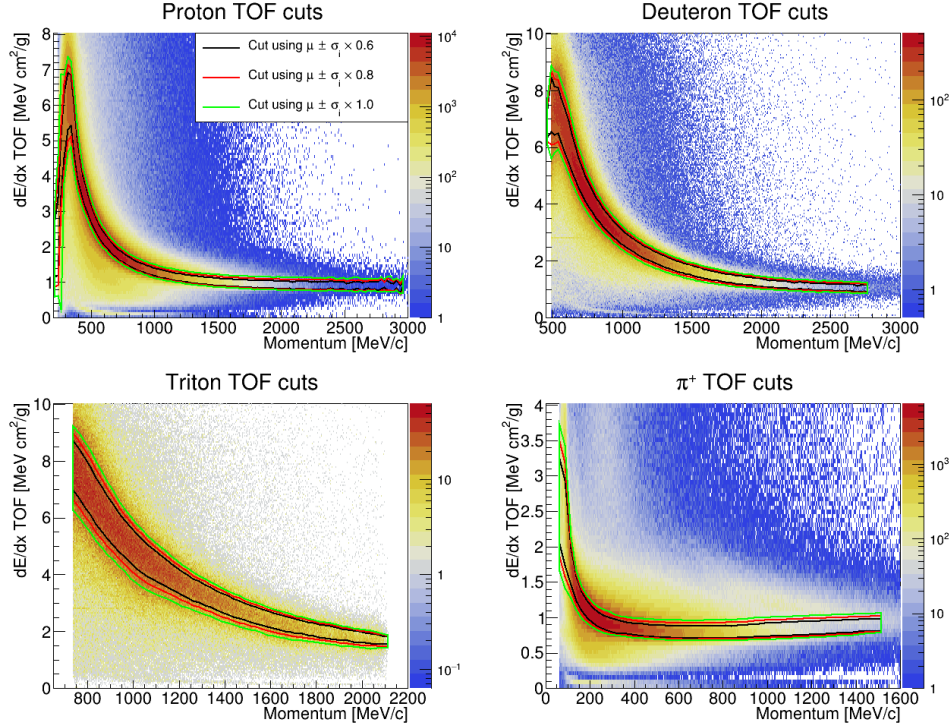
Figure 3.9: The same as in fig. 3.8 but for TOF detector.

7. The μ and σ of the asymmetric Gaussian fit are used to determine the
   various width of the MDC cuts. The widths of cuts are given by calcu-
   lated values of $[\mu - \sigma_l \times m, \mu + \sigma_r \times m]$ where m takes values of 0.6, 0.8,
   1.0, 1.2 and 1.5. The examples of MDC dE/dx vs. *momentum* distri-
   bution of p, d, t, π^+ with superimposed MDC cuts of three different
   widths are shown in fig. 3.8. Using of various cut widths is needed in
   order to estimate the systematic uncertainty of the PID method. This
   point will be recalled when the systematic error components will be
   discussed (see chapter 3.2.4).
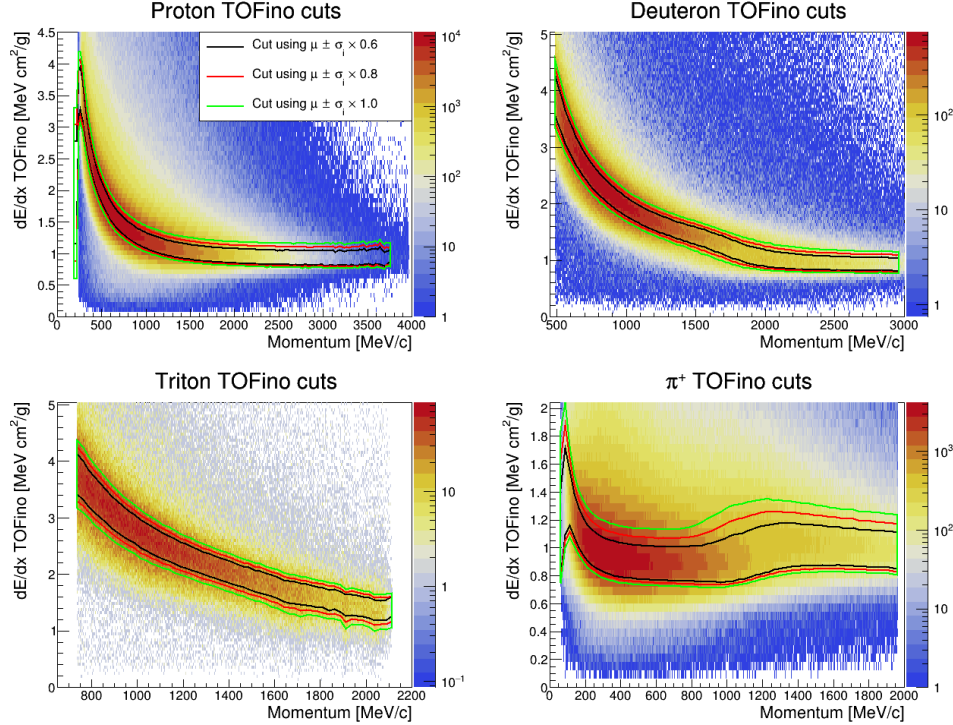
Figure 3.10: The same as in fig. 3.8 but for TOFino detector.

8. The particle distributions selected with the use of MDC cuts are further used to create the dE/dx vs. *momentum* distributions and the identification cuts but for reaction products registered in TOF/Tofino detectors. For this aim the points 3 - 7 of the analysis scheme are repeated. Multiplication factors m for TOF/Tofino cuts are equal to 0.6, 0.8, 1.0, 1.2, 1.5 and 1.8. These spectra are used for derivation of both the distributions containing the "signal" of the searched for cross-section as well as for identification of the background component. Examples of the dE/dx vs. *momentum* distributions for TOF and Tofino detectors are shown in fig. 3.9 and fig. 3.10.

In this three-level approach (after demanded smoothing) the most precise 2D identification cuts for dE/dx - *momentum* distributions are defined. Finally they are applied for the raw data distributions (disregarding the initial cuts on the *mass* distribution) in order to identify the reaction products of interest unbiased with the reconstructed TOF value.

The separation of negatively charged pions from other reaction products is provided by their opposite deflections in the magnetic field. For them the definition of identification cuts is not needed. The contamination of the π^- spectra with the K^- is insignificant and for this reason neglected in this analysis.

3.2.2 Signal and background identification

In the current work the emphasis is put on the kinetic energy and angular dependence of the production cross-section. (For now on when the term "energy" is used always the kinetic energy of the emitted particle is meant). In order to study the angular dependence of cross-section the dE/dx - *momentum* distribution of particles detected in TOF/Tofino detectors are prepared for the selected emission angles between 20° and 85°. The identification 2D cuts of different widths as defined above are applied. The example of identification cuts of three different width $\mu \pm \sigma_i \times m$ where m is multiplication factor equal to 0.6, 0.8, and 1.0 for deuterons detected at the emission angle of 18° - 45° is shown in fig. 3.11.

The resulting distributions (which should contain mainly identified reaction products) are bin-by-bin projected onto dE/dx axis. The *momentum* bin is equal to 25 MeV/c.

In effect the one dimensional distributions of energy losses in TOF or Tofino detectors are obtained. They comprise the component of the searched for particle superimposed on the background formed by the misidentified particles of the lower or higher mass. Fig. 3.12 presents examples of such distributions for p, d, t and π^+ registered at $\theta = (65 \pm 1.5)°$ and for various *momentum* bins. They are done as well for selected widths of identification cuts.

It is well visible that the particle identification scheme described above has limited strength. The selected distributions of reaction products of interest are still superimposed on the distributions of misidentified particles, which form the background.

In order to calculate both the signal and background components of the distributions the fitting of the appropriate functions is performed.

The functions which approximate the shapes both of the signals as well as the background distributions in principle should be the Landau functions. Landau function describes the best the distributions of energy losses in solids and in the gasses due to individual interactions of charged particles with

Deuteron TOFino cuts
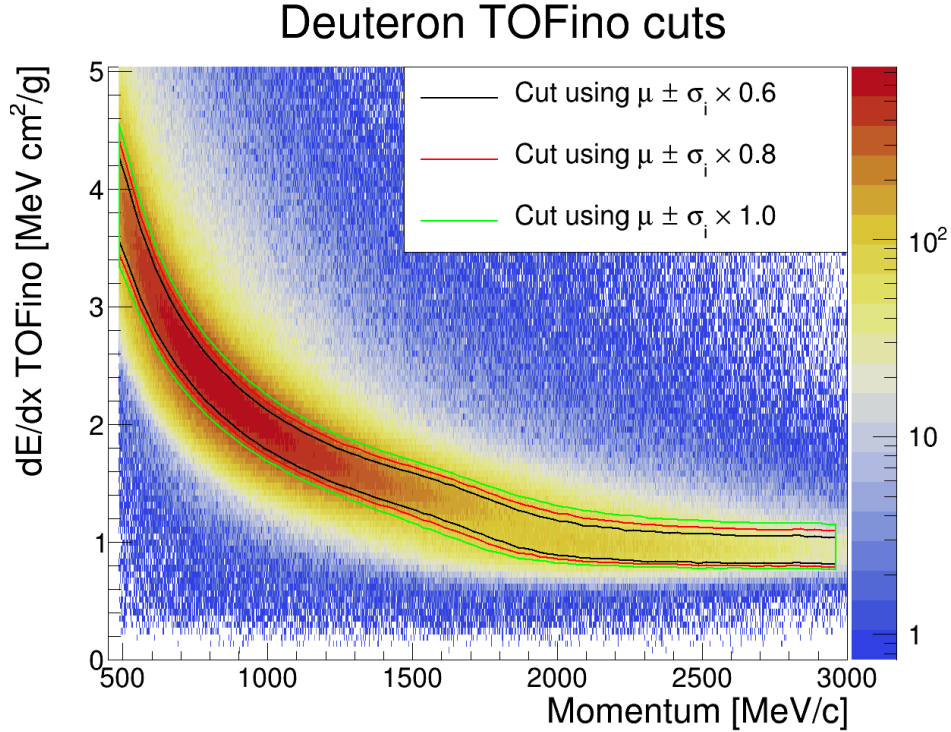
Figure 3.11: Example of the identification cuts applied for selection of
deuterons detected at θ laboratory angle of $18°$ - $45°$. Three different width
$\mu \pm \sigma_i \times m$ of the cuts are shown.

the atoms or molecules of the medium in the studied here energy range.
However in the case of this analysis it turned out that both the signal and
the background distributions do not follow the Landau function. It is due to
the multi-step cuts applied to the raw data, which caused the truncations of
the original experimental distributions of events.

Thus, in described here method the signal is fitted always as an asymmetric Gaussian. (In fig. 3.12 the fitted functions of the signal components are
given with green color and superimposed on the experimental distribution).
Efforts were made to fit the signal distribution in the range where the signal
component is clearly separated.

For the protons (fig. 3.12, *upper-left panel*) and pions (fig. 3.12, *lower-right panel*) the components of signal are dominant (in the latter case only
for the limited energy range). The background is small and easy to identify.

It can be approximated by the linear function fitted to the both sides of the signal distribution. (In fig. 3.12 the fitted contributions of background are given with red color).

Much worse signal to background ratio is obtained for deuterons (fig. 3.12, *upper-right panel*). However still the component formed by deuterons is clearly separated from the component originating from protons. The background is fitted as an exponent.

The most difficult was to separate the tritons from background components originating from other species, mainly from deuterons. In fig. 3.12, *lower-left panel*, the signal from tritons is small in comparison to well visible peak of d and traces of p distribution (most to the right).

Various efforts to separate the net component of triton from the dominant background were undertaken. The most effective one occurred to be the fitting of the proton background with the Landau function and two asymmetric Gaussian functions for the deuteron and triton distributions. Then the convolution of all three functions is fitted (cf. fig. 3.13) With the use of obtained parameters the signal and background functions are fitted again. In fig. 3.13 they are shown with green and red color, respectively. Finally the background component inside the region of the cut $\mu \pm \sigma \times m$ is calculated with the use of obtained signal and background fits.

The quality of separation of individual components of dE/dx distributions for positively charged reaction product varies with the momentum of particles. It is better for the lower momenta and deteriorates when particle momentum increases. The distributions of specific energy losses get closer each to other with the momentum rise.

At some momentum the signal to background ratio is so unfavorable that the identified signal component is charged with too high uncertainty. In this thesis it was arbitrary selected that the signal is separated from background if for the applied width of cut the background to signal ratio is smaller than 50% (for d and π^+) and 60% (for tritons). For clean p and π^- distributions such condition is not needed).

Fig. 3.14 shows the example of the distributions of background to signal ratio (in percent) for tritons detected at $\theta = (50 \pm 1.5)°$ and for different widths of the PID cuts. In this case the maximal momentum at which the signal distribution is considered as separated from the background is equal to 1500 MeV/c.

The net value of the signal component for the given momentum bin is calculated by subtracting the area of the fitted background function from
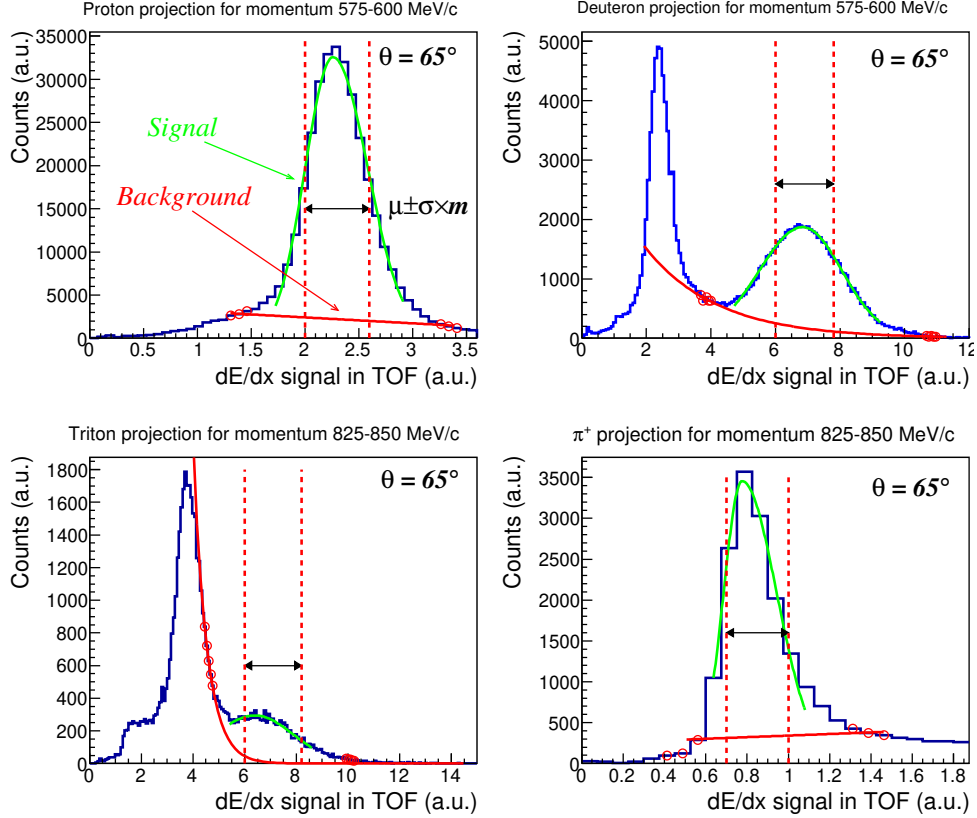
Figure 3.12: The dE/dx distribution for p, d, t and π^+ registered in TOF detectors at laboratory θ angle of $(65 \pm 1.5)°$. Examples show distributions for various energy bins and selected with various widths of identification cuts. These spectra provide the information both about the "signal" component of the cross-section as well as the background of misidentified particles. The fitted distributions of signal (green color) and background (red color) are superimposed. Calculation of the widths of identification cuts $m \times \sigma$ are explained in the text.

the area of the fitted signal functions. It is important to stress that the subtraction is done only in the selected limits, which are narrower than the range of fitted signal distribution. This limits are related to the mean value μ and the standard deviation σ of the fitted Gaussian function. They are calculated as: $[\mu - \sigma \times m, \mu + \sigma \times m]$ where $m = 0.6, 0.8, 1.0, 1.2, 1.5, 1.8$
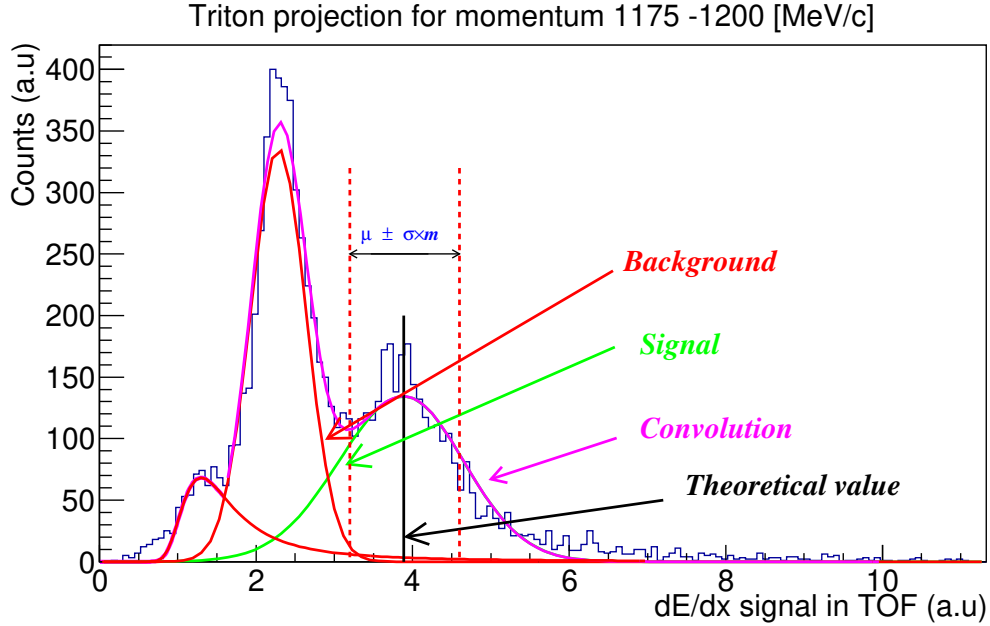
Figure 3.13: The dE/dx distribution for t registered in TOF detectors at laboratory θ angle of $(55 \pm 1.5)°$. Examples show background estimation of triton with the cut value $\mu \pm \sigma \times m$ These spectra provide the information both about the signal component of the cross-section as well as the background of misidentified particles. The fitted distributions of signal (green color) and background (red color) are superimposed.

The amount of events contributing to the searched for specific cross-section at given laboratory emission angle θ and for given energy bin is calculated as an average of the values obtained for all applied multiplication factor m.

The PID and the background separation for the π^- distribution is not necessary. They are well identified by the HADES apparatus itself.

3.2.3 Efficiency and acceptance corrections

Proper calculation of geometrical acceptance and the efficiency of the overall detection and acquisition system (DAQ) is crucial for correct calculation of absolute values of studied here cross sections. These quantities remain in complicated dependence on detection geometry, composition of the de-
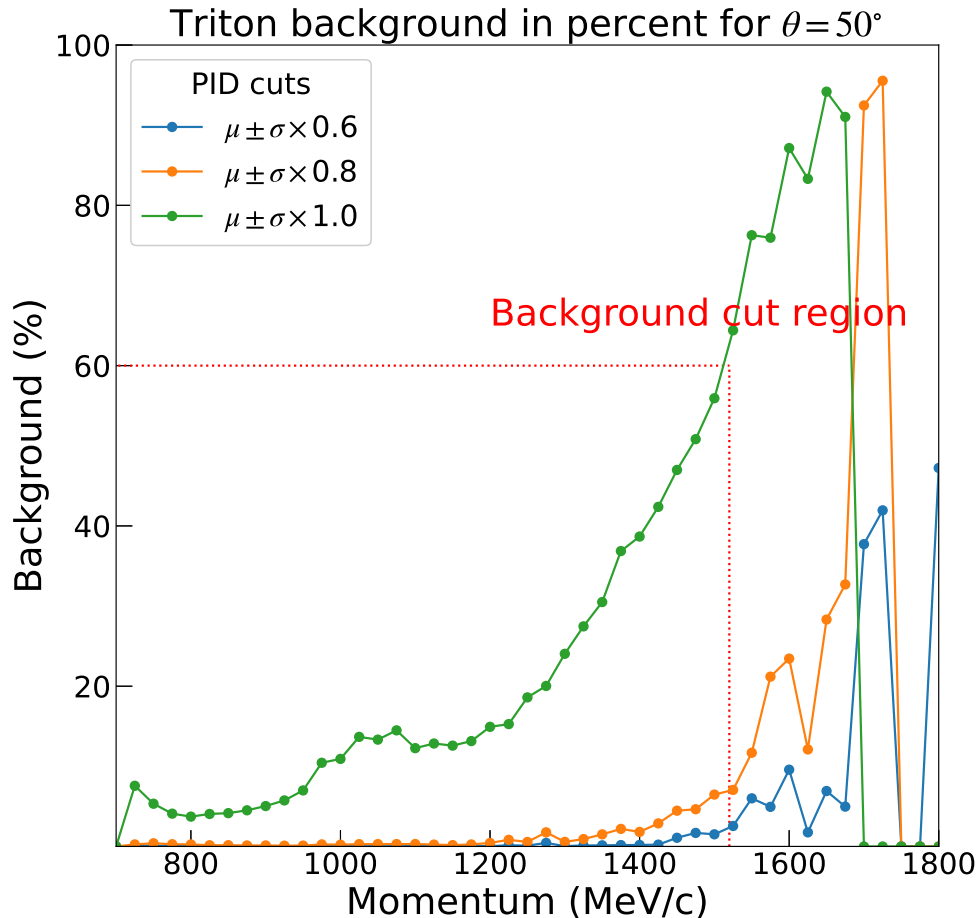
Figure 3.14: The distributions of background to signal ratio for tritons measured at laboratory angle $\theta = (50 \pm 1.5)°$ obtained for tree different widths of PID cuts. It is decided that in this case the reliable separation of tritons from background particles is possible for their momenta lower than 1500 MeV/c. Above this value the background to signal ratio gets higher than 60%.

tection system, types of primary particles and their energy- and angular distributions, the yields of secondary particles and their distributions, the efficiencies of individual detectors, condition of trigger, dead time of DAQ.

The calculation of the cross-section corrections caused by geometrical restrictions and finite efficiencies can be done only with the help of software tools explained already in subsection 3.1.6. The exact geometry of the ap-

paratus and the response of the detectors to the irradiation is implemented
into the HGeant package [69]. HGeant is based on the Geant3 toolkit [70].

The actual conditions present during the data taking are considered by
the HYDRA framework [71]. This package contains as well all needed calibra-
tions, tracking tools, electronics response to detected particles and emulation
of trigger logic (cf. 3.1.6).

In principle the acceptance and efficiency of the detection system has to
be calculated as a ratio of two distributions:

i) the so called *ideal* distribution - it is obtained by simulation of well
known and dominant processes with assumption that the 4π detection
geometry is available and the overall efficiency of the detection system
is equal to 100%;

ii) the *real* distribution - obtained by simulation of the same processes but
including the geometrical restriction and finite efficiencies of all com-
ponents of HADES detection system. These restrictions are included
to the HGeant and Hydra software.

Of course the product of efficiency and acceptance, (Efficiency x Accep-
tance - EA), is dependent on the energy, emission angle and the kind of the
emitted particle. It is given by the formula:

$$EA(Z, A, E, \theta) = \frac{real(Z, A, E, \theta)}{ideal(Z, A, E, \theta)} \qquad (3.2)$$

where the Z, A are the atomic and mass number of particle of energy E
emitted at laboratory angle θ.

Both the *ideal* as the *real* distributions are simulated as scatter plots θ vs.
Energy. They have to be divided bin by bin for reasonable selected angular
and energy bin widths. (Please, note that from now on instead of used former
momenta of the particles their energies are calculated. It is due to the aim of
presenting the resulting cross-sections distributions as a functions of energies
of the reaction products).

The examples of the *ideal* and *real* 2D distribution for proton as well as
the resulting EA distribution calculated for each energy-angle bin according
to formula 3.2 are shown in fig. 3.15 a, b and c, respectively.

For the specific case of the single spectra of spallation reaction studied in
this work, it was needed to test if EA calculated in such a way is independent
of the conditions applied in simulations.

(a) *ideal* distribution

(b) *real* distribution
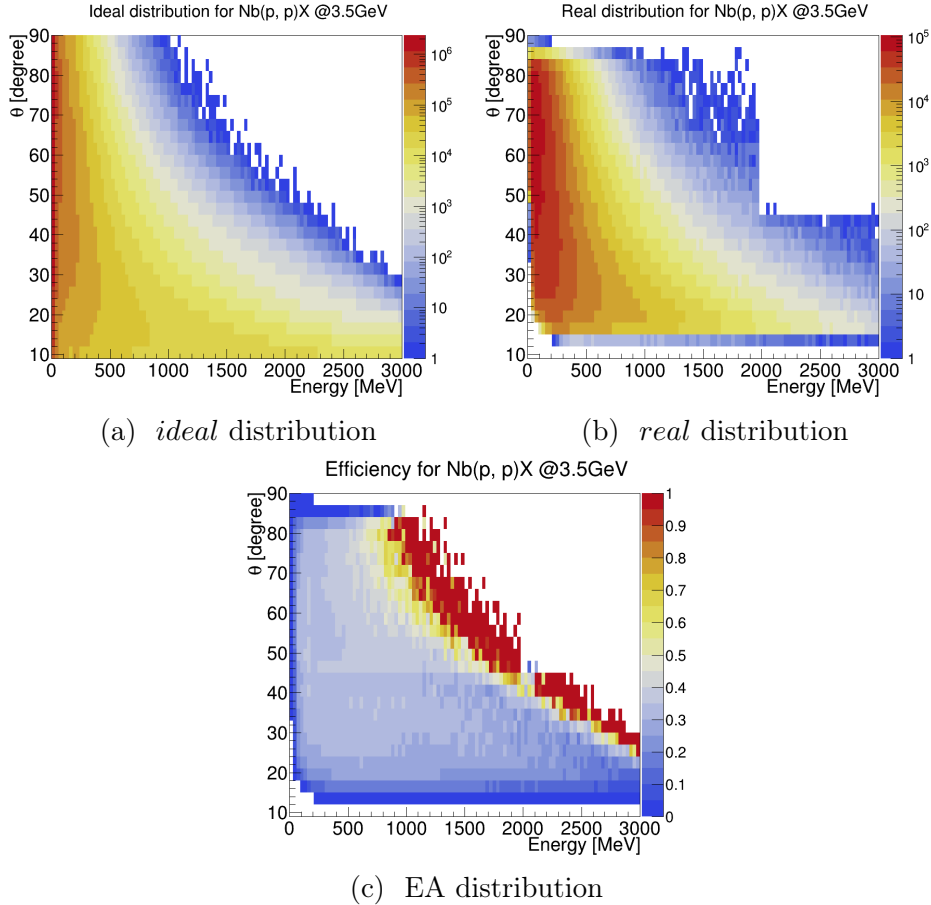
(c) EA distribution

Figure 3.15:   Example of distributions used for calculation of overall Efficiency and Acceptance, *EA* for detected particles: (a) *ideal* distribution
calculated for protons generated from INCL++ model; (b) *real* distribution
including the detection geometry and particular efficiencies of the HADES
system (generated using HGeant+ Hydra + dE/dx cuts for $\mu \pm \sigma \times 0.8$); (c)
resulting *EA* distribution obtained after dividing real distribution by ideal
one.

In the first step of *EA* calculation it was checked if this method is robust
against the kind of event generator used for simulations of ideal and real
distributions.

The simulations were done using the event generator which simulate the
isotropic emission of protons of the energy sampled from the range [0,3500]

MeV into the full solid angle. It turned out that when the initial multiplicity of protons is equal to 8 the resulting EA is smaller than when the multiplicity of generated protons is equal to 16. Examples of such calculation of EA for registration of protons at the laboratory emission angle $\theta = 37.5° \pm 1.5°$ are shown in fig. 3.16. EA values obtained when multiplicity of initial protons are equal to 16 (fig. 3.16 (b)) are larger by $\sim 9\%$ from those for isotropic event generation with multiplicity of 8 (fig. 3.16 (a)).

(a) Mutiplicity 8.

(b) Mutiplicity 16.
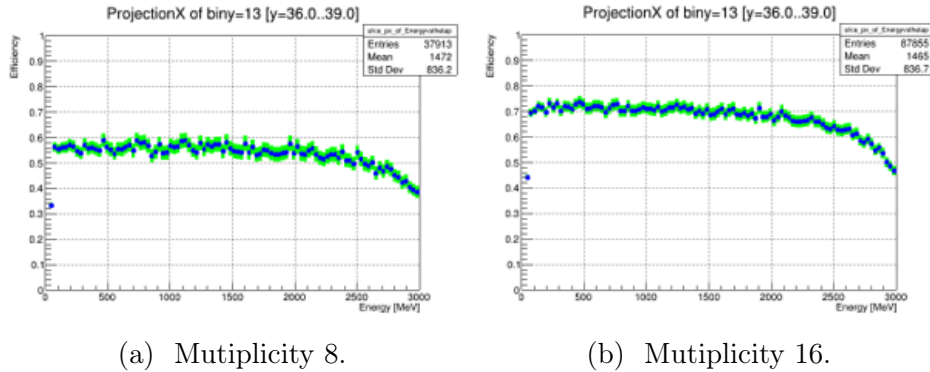
Figure 3.16: Product of Efficiency and Acceptance, EA, for detection of protons at laboratory angle $\theta = 36°$ - $39°$. Event generator simulating the isotropic emission of protons with multiplicity 8 (a) and 16 (b) into the full solid angle were used. Kinetic energies of generated protons were ranging from 0 to 3.5 GeV. For details see text.

This finding indicated that the calculation of EA might be biased by improper selection of the event generator. The reliable value of EA must be calculated with the use of the event generator which approximates sufficiently precise at least the dominant production and emission processes in the target. This include both the types and the yields of particles emitted from the target as well as their energy and angular distributions.

For these reason it was decided to use the INCL++ model as an event generator. It was many times confirmed that this model reproduces the multiplicities, energy and angular distributions of dominant spallation products with the precision of factor about 2, what was anyway the best achievement among the spallation reaction models [10].

The correctness of the INCL++ model used as an event generator for calculation of overall EA values in the present studies is confirmed by the good

agreement of experimental and simulated multiplicities of detected particles for $p + Nb$ reaction measured at HADES. It is shown in fig. 3.17.
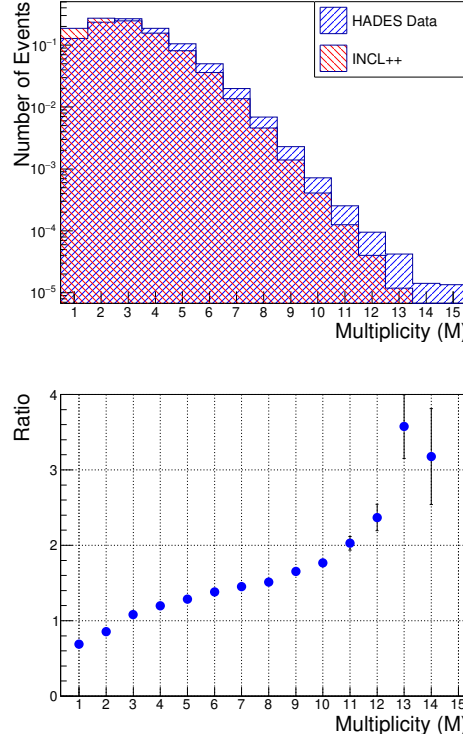
Figure 3.17: Upper panel: multiplicity distribution of primary particles obtained by simulations with the use of HGeant + Hydra software and the INCL++ model as a event generator. The theoretical distribution is compared to the experimental one registered in HADES with the use of the same software tools used for tracking and EA corrections. Both distributions are normalized to the same total number of events. Lower panel: ratio between the experimental and simulated distributions.

The experimental distribution there comprises only those particles which tracks could be reconstructed back to the target position. It means that only primary particles produced in the target contribute to the multiplicity distribution. The secondary particles, which contributed to the trigger (trigger condition demands at least 3 charged particles in the TOF/Tofino scintillating walls) are suppressed. For this reason experimental distribution contains

the contribution from multiplicity equal 1 and 2.

Simulated distribution (marked in fig. 3.17 as "INCL++") is obtained with the use of the same HGeant and Hydra environment and parameters as it was used for creation of experimental distribution of multiplicity in $p + Nb$ reaction. In simulations the energy of bombarding protons used for generating the particles entering the detection system was set the same as energy of beam protons, i.e. 3.5 GeV.

For the most dominant multiplicities of events (between 1 and 7) the ratios of experimental/simulated distributions varies between 0.7 and 1.4. It is a proof that an INCL++ is an sufficiently realistic event generator for the studied reaction. Experimental conditions can be reasonably well reproduced by INLC++ + HGeant + Hydra combined frameworks. EA values calculated with use of these tools are reliable.

The problem of possible bias of the calculated efficiency for registration of single spectra in HADES by the trigger conditions, which required coincidences of at least 3 charged particles will be addressed in subchapter 3.2.4.

The *ideal* and *real* distributions were simulated for each of reaction products studied in this thesis and the scatter plots of θ vs. *Energy* were created. In order to assure the smooth dependence but also the sufficient resolution the binning of both axes has been optimized. Finally the width of energy bin was selected as 30 MeV and the bin of θ angle is equal to 3 degrees.

In order to obtain the energy dependence of efficiency for the selected emission angle the demanded angular slit is defined and the two dimensional EA distribution is projected onto energy axis. Such example is given in fig. 3.18 where product of overall efficiency of the system and its geometrical acceptance is shown for detection of single distribution of deuterons emitted from target at $43.5\pm1.5°$ laboratory θ angle. The EA values calculated without the PID cuts applied for *real* distribution is given with red dots whereas the EA distribution reduced due to selection of fraction o experimental distributions defined within the PID cut is shown by blue dots. As described in 3.2.1, for assessment of systematic uncertainty of cross-section due to PID, it was calculated with the use of various widths of PID cuts. The widths of PID cuts applied for simulations were always the same as those defined for experimental distributions. In case of reduced EA distribution of fig. 3.18 the width of the PID cut was equal to 0.8 σ.
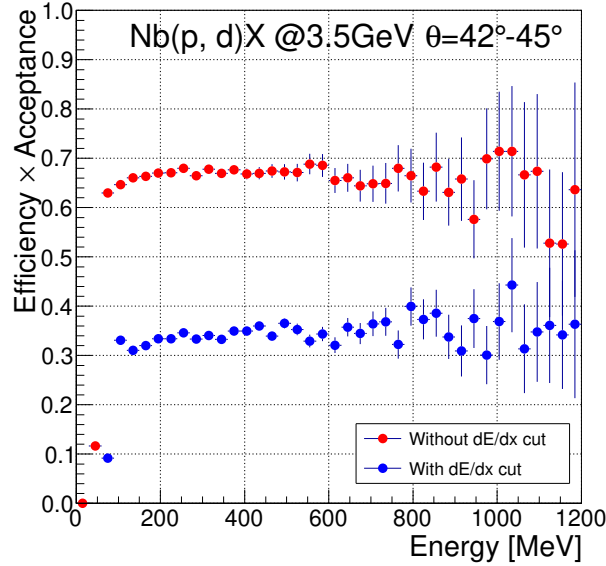
Figure 3.18: Example of HADES efficiency for registration of deuterons at
$42° < \theta < 45°$ laboratory angle. The red dots represent the efficiency ob-
tained when the PID cuts were not used whereas the blue dots show the final
energy dependence of efficiency used for correction of absolute cross-section.
In this case the PID cut of the width equal to 0.8 σ is applied to the *real*
distributions of deuterons.

3.2.4 Experimental uncertainties

The broad acceptance and overall high luminosity for the experiment when
$p+Nb$ at 3.5 GeV reaction was measured provided huge statistics of collected
events. For the aim of present study 10^8 events have been analyzed. Thus, the
statistical error of the measurement is insignificant and will not be considered
in this work.

The components of systematic uncertainty are discussed below. They
origin from:

- misidentification of signal and background particles due to imperfect-
  ness of PID cuts, the limited quality of fits for the signal and back-
  ground distributions and the uncertainty of background dispersion;

- calculations of efficiency and acceptance of the apparatus

- deviations in the performance of individual sectors of HADES detection system;

- uncertainty of absolute normalization of the data used in HADES experiment.

The last component of the systematic error is constant and equal to 15%. This value is adopted from the data analysis performed in the HADES collaboration already in the past with the use of the same data but for other reaction products [62, 74]. In that case the comparison of the HADES results to the pion data measured by HARP-CDP collaboration [74] were done.

The particle (P)- energy (E)- and angle (θ) dependent systematic uncertainty ($\sigma_{sys}(P, E, \theta)$) is calculated for individual particle, its selected emission angle and for each energy bin of 30 MeV width. It is taken as a square root of sum of squares of individual components of error:

$$\sigma_{sys}(P, E, \theta) = \sqrt{\sigma_{PID/backg}(P, E, \theta)^2 + \sigma_{EA}(P, E, \theta)^2 + \sigma_{sec}(P, E, \theta)^2} \quad (3.3)$$

where $\sigma_{PID/backg}(P, E, \theta)$, $\sigma_{EA}((P, E, \theta))$, $\sigma_{sec}(P, E, \theta)$ are PID and background error, efficiency + acceptance error and sector error, respectively. They are discussed below.

Error due to PID/background

In the above subsection 3.2.2 the method of identification of individual charged reaction products among the raw data distribution is explained. Due to the lack of *mass* identification based on TOF measurement only the PID method utilizing the specific ionization losses can be utilized. As shown in figs. 3.9, 3.10, 3.12 and 3.14 despite good energy resolution of HADES detectors the effectiveness of this kind of PID is restricted only to the lower range of energy spectra. Even then the contribution of misidentified particles to the background is significant.

As mentioned already the systematic uncertainty of combined PID and background subtraction method is estimated with the use of multiple PID and background identification with application of various widths of identification cuts. The widths of used cuts were calculated by multiplying the standard deviation σ of the fitted asymmetrical Gaussian function. Factor m equal to

± 0.6, ± 0.8, ± 1.0, ± 1.2, ± 1.5 and ± 1.8 is used for this aim. The limits of cuts were fixed symmetrically around the mean value of fitted function.

As the systematic error of the method the value equal to the standard deviation of all obtained results is taken.

PID/backgground error is calculated by following formula:

$$\sigma_{PID/backg} = \sqrt{\frac{\sum_m (x_m - \mu)^2}{N}} \tag{3.4}$$

where x_m represents the double differential cross-section obtained by each cut with factor m having values ± 0.6, ± 0.8, ± 1.0, ± 1.2, ± 1.5 and ± 1.8. The symbol μ represents the mean of all cross-sections. N is number of cuts applied with all m values.

The usual value of ($\sigma_{PID/backg}$) remains below 5%. For some energy bins of triton distribution it can reach several percent.

Efficiency and Acceptance uncertainty

In order to perform the absolute normalization of the cross-section the overall efficiency and acceptance, EA, distributions for particles studied in this work i.e, for p, d, t, π^- and $\pi+$ have been determined (cf. subsection 3.2.3 and examples in figs. 3.15, 3.18). In the case of the current study, the actual EA value is a convolution of detection efficiencies of various components of the HADES system, the effectiveness of the data acquisition system, the trigger conditions and the distributions of secondary particles created in the HADES setup and contributing to the triggering of event. The total efficiency is dependent on energy, emission angle and type of particle.

For calculation of EA two theoretical distributions (*real* and *ideal*) are divided. Thus, the possible deficiencies of the theoretical model and software tools used for simulation of the HADES response cancel out.

It was proven during long term operation of HADES and from the other performed up to now analyses that the EA distributions of HADES varies smoothly with the emission angle of detected particle and with its energy. Observed significant fluctuations of EA in neighboring bins of energy (or angle) indicate that in this region of energy PID of particles is not effective enough or the statistics of simulations is not sufficient. In example given in fig. 3.18 significant fluctuations of EA for deuterons detected at the given angle are observed above 750 MeV. This energy region is not considered for calculations of cross-section.

In the energy regions where EA distributions change monotonically the resulting correction factors were smoothed by applying the running average over 3 consecutive energy bins. The standard deviation of the running average is assigned as a measure of the systematic error of the efficiency correction.

It has to be remarked that the dominant limitation of the energy ranges where the production cross-sections could be determined in this studies comes from the limited PID strength for highest energies of detected particles. The energy limits resulting from not monotonic distributions of EA are usually less important.

The modification of EA due to contribution of secondary particles and thus to the single spectra measured in this work is suppressed by the tracking procedure. Also for calculation of EA the secondary particles from events generated by INCL++ are "created" by HGeant and effectively tracked by Hydra. In effect the simulated distribution of multiplicity very well agrees with experimental one (c.f. fig. 3.17). This is sufficient for reliable determination of EA by dividing the *real* by *ideal* distribution. Thus, the uncertainty from production of secondary particles do not need to be considered here.

It has to be also checked if the trigger condition demanding more than two charged particles detected in TOF/Tofino walls can influence the efficiency for registration of single spectra. Special care in this respect has to be put on the events, which comprise only one or two primary particles emitted into HADES acceptance. The DAQ would be insensitive for such events if these particles do not contribute to creation of secondary products. They would not give sufficient contribution to the multiplicity of trigger.

It was checked that simulations of the *real* distributions with the combinations of the event generator, HGeant and Hydra take into account such cases. It means that the reduction of efficiency due to disregarded events of the low multiplicity emitted towards the HADES apparatus (so called trigger bias of the single spectra) is included into EA calculation and does not need to be treated separately.

Thus, the total uncertainty σ_{EA} of EA consists of the component which comes from small fluctuations of calculated EA distributions. It depends on the kind of registered particle, its energy and emission angle. This uncertainty varies in the range of 2 - 5%.

Differences in sectors performance

HADES detection system consists of six equivalent sectors, which cover the
forward emission cone and provide the detection acceptance in 360° range of
the azimuthal angle ϕ. The ϕ angle coverage of individual detection sectors
is presented in fig. 3.19.
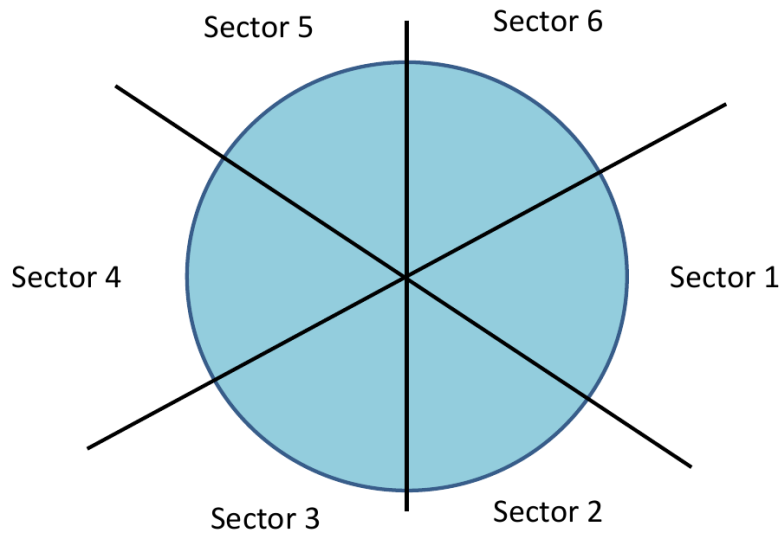
Figure 3.19: Azimuthal position of individual detection sectors in HADES
forward cone.

The construction of the sectors should provide the full detection symmetry
in the forward acceptance range of HADES.

The distributions of measured cross-sections can be however affected if
performance of individual sectors departs from the assumed equivalence.

For this reason the same kind of analysis as described above for the global
setup has been performed for the particles detected in each individual sector.

First it was checked if there are difference in the shapes of the cross-section
distributions obtained for individual sectors for all the reaction products of
interest. It was done by application of the Pearson coefficient ρ used to test
the linear correlations among the discrete sets of variables and given with
the formula:

$$\rho(X,Y) = cov(X,Y)/\sigma(X)\sigma(Y) \tag{3.5}$$
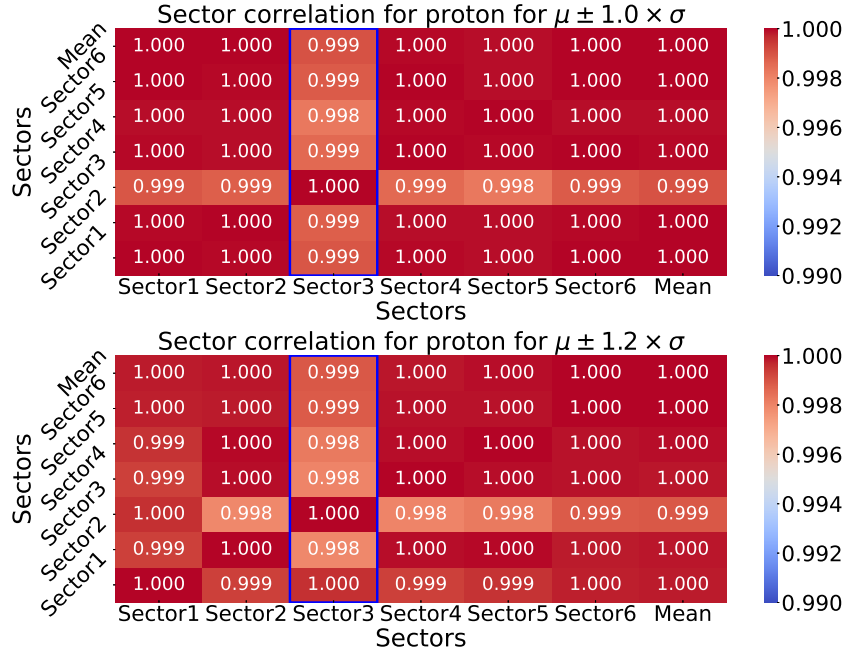
Figure 3.20: The estimator of the Pearson correlation coefficient ρ (cf. equation 3.5) was calculated by means of the Python data frame PANDAS. Experimental distributions obtained for different detection sectors of HADES were used in order to check the possible differences in the shapes of the obtained cross-sections. Given example is for the proton distributions obtained when the width of identification cut was of 1.0 σ (upper panel) and 1.2 σ (lower panel). For description of the width calculation of the identification cuts please, refer to section 3.2.1. The values of coefficient for all combinations of sector results are practically equal to 1. This indicate that their linear correlation is maximal and discrepancies in the shapes of the cross-sections distributions for individual detection sectors do not exists.

In the examined case the X and Y are the distributions of cross-sections provided by individual sectors, the $cov(X, Y)$ is their covariance and $\sigma(X)$, $\sigma(y)$ are their standard deviations.

As it is shown in fig. 3.20 where example of the ρ coefficient calculated for proton cross-sections obtained for individual sectors are given, for each combinations of sector pairs the value of ρ is almost equal or equal to 1. It means that shapes of cross-sections distributions for individual sectors are
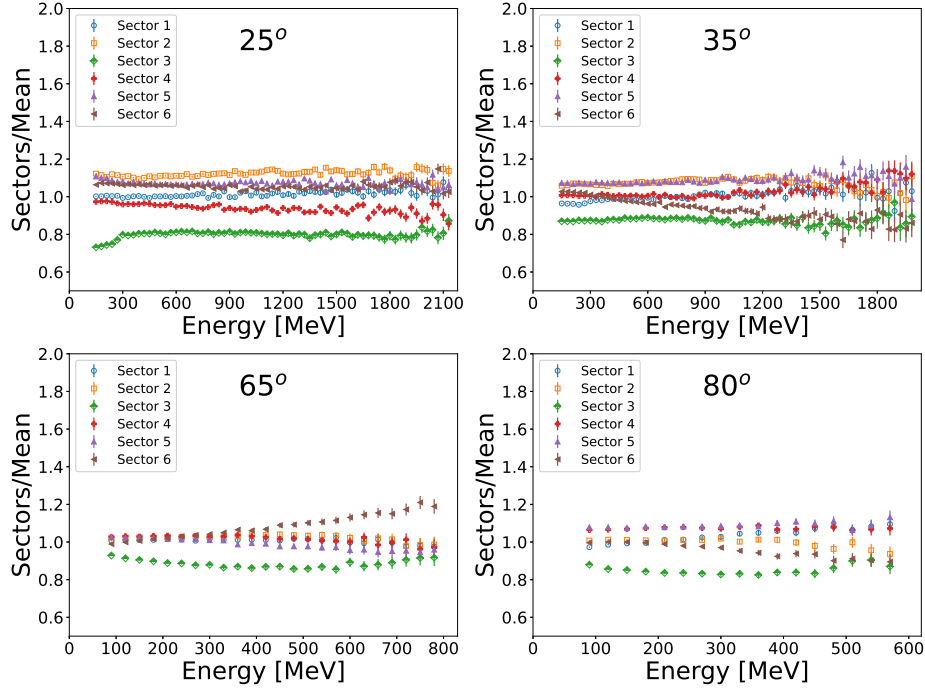
Figure 3.21: The example of the ratio R given by the formula 3.6 calculated
for cross-section distributions obtained for individual sectors at four selected
emission angles. Here the sum of cross-sections for all positively charged
particles is taken into account. The most significant deviation of the cross-
section is visible for sector 3.

identical.

In this way it was proven that the individual sector does not influence
the shapes of the measured distributions. Unfortunately the variation in the
values of cross-sections obtained for individual sectors has been realized.

The differences among values of cross-sections provided by individual sec-
tors are quantified in following way:

The ratio R_i of the value of cross-section σ_i measured in sector i to the
average of cross-section of measured in all sectors $(j = 6)$ is given with the
formula:

$$R_i = \frac{\sigma_i}{\sum_{j=1}^{6} \sigma_j / 6} \tag{3.6}$$
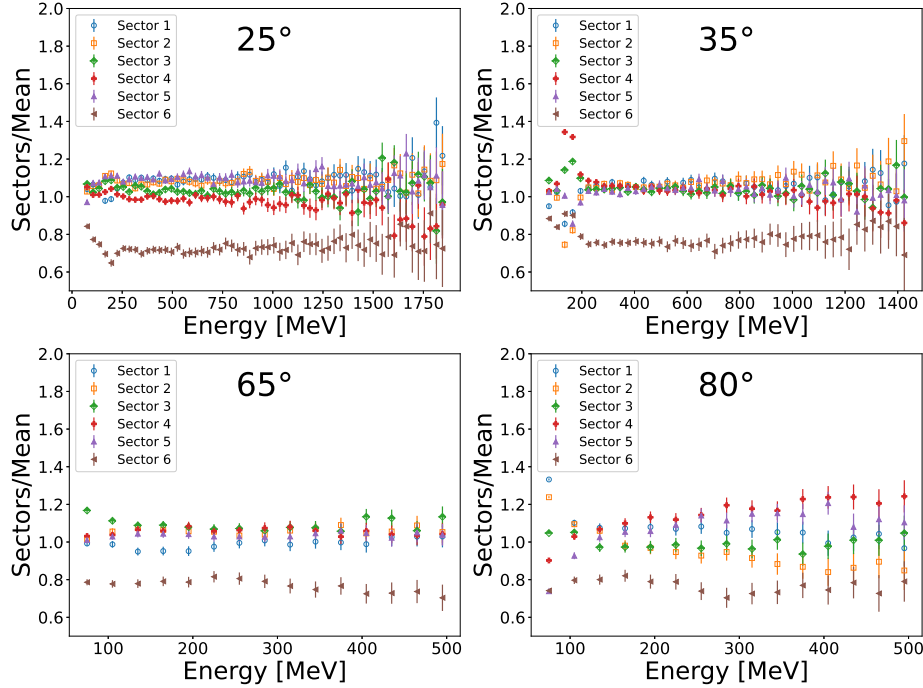
Figure 3.22: The example of the ratio R given by the formula 3.6 calculated for π^- production cross-section for individual sectors at four selected emission angles. The most significant deviation of the cross-section is visible for sector 6.

As it is shown in fig 3.21 and 3.22, the most significant differences in the absolute values of cross-section in comparison to the average values are observed for sector 3 (for positively charged particles) and for sector 6 (for π^-).

In order to estimate the component of cross-section uncertainty (in percentage) due to variation in results of the individual sectors $(\sigma_{sec(i)})$ the following formula has been used:

$$\sigma_{sec(i)} = (100/6)(\frac{\sigma_i - \sigma_{mean}}{\sigma_{mean}}) \tag{3.7}$$

where σ_{mean} is the average cross-section over the sectors for the given particle, emission angle and the energy bin.

The examples of $\sigma_{sec(i)}$ are shown in 3.23 and 3.24.

Considering the deviations in the magnitude of the results of individual
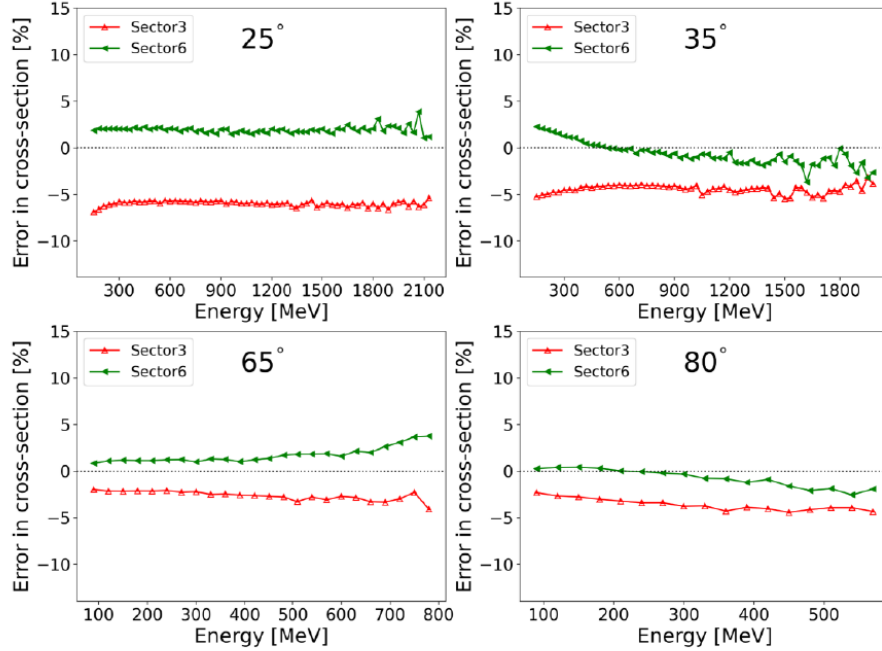
Figure 3.23: The example of the distribution of the uncertainty $\sigma_{sec(3)}$ and $\sigma_{sec(6)}$ resulting from the deviation of the results for sector 3 and sector 6. $\sigma_{sec(i)}$ is calculated according to formula 3.7 for protons detected at four selected angles.

sectors the error of the "whole" cross-section caused especially by sector 3 and sector 6 is not lager than 7%.

Uncertainties calculated in the way as explained above for each kind of detected particle, all selected emission angles and for each of energy bin are considered as a component of the systematic uncertainty of the measured cross-sections.

3.3   Verification of results

In order to verify the results obtained in present studies and gain confidence about the applied data analysis scheme the relevant experimental results have been searched for in literature. The same cross-sections as shown in this work are not available. Thus, the verification has to be based on the rare data of
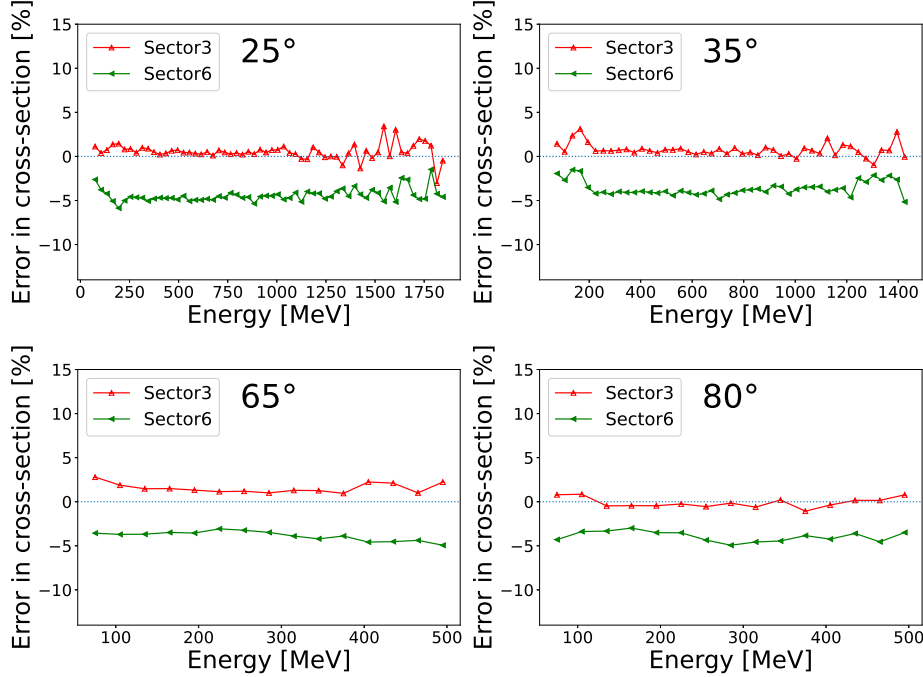
Figure 3.24: The example of the distribution of the uncertainty $\sigma_{sec(3)}$ and $\sigma_{sec(6)}$ resulting from the deviation of the results for sector 3 and sector 6.. $\sigma_{sec(i)}$ is calculated according to formula 3.7 for π^- detected at four selected angles.

proton induced spallation but measured for different target masses and at different bombarding energies than those used in present study. It is allowed since the shapes of the spallation distributions in the energy and mass range of interest are similar. It means that independently of the target mass and the proton beam energy the shape of resulting spectra are the same or change very slowly. The magnitude of cross-section is both the energy and target mass dependent. It rises with the beam energy and the mass number A of the target. But this rise is also moderate. Thus, taking into account mass and energy dependence of the cross sections the comparison of the results for similar target masses and similar beam energies is justified. Moreover, usually the compared spectra are biased with experimental errors of the similar range as the expected differences in the cross-sections.

As it is shown below the samples of double differential cross-sections ob-

tained in the current analysis are compared to the other experimental results of this type. It is possible for all particle species studied in this thesis but only for limited energy and angular ranges where the similar data exist.

At first the consistency check of the current and earlier analysis of HADES data is shown.

3.3.1 Former HADES results for negatively charged pi-ons

The data collected for collision of $p + Nb$ at 3.5 GeV at HADES have been partially utilized earlier for studies of various reactions. Among them the inclusive pion and η production has been examined [62]. In that analysis the transverse momentum distributions $dN/p_\perp$ of π^- have been derived. This permits to perform the partial comparison of the results obtained in this thesis with the former HADES results derived from the same raw data but with completely different methodology. For this aim the transverse momenta $p_\perp$ of π^- resulting from the present analysis have been calculated.

Fig. 3.25 shows the comparison of the $p_\perp$ distributions obtained in the former and in the current analysis. Both $p_\perp$ distributions are integrated over rapidity range of $0.2 < y_{lab} < 1.8$. The good agreement between these two distributions proves that the analysis scheme applied in this thesis provides correct results.

It has to be remembered that for the π^- the selection cuts were not needed. Thus, agreement of the results presented here proves the correctness only of the analysis steps used after the PID/background selection.

3.3.2 Mid-energy pion spectra

Double differential cross-section of similar type have been measured in HARP-CDP experiment. The HARP-CDP collaboration provided the proton and pion spectra for proton induced reaction on some atomic nuclei from Be to Pb at 4.1 GeV proton bombarding energy [75–81] . Among them the cross-section for π^+ production in $p+^{64}Cu$ [78] and $p+^{181}Ta$ [77] reactions can be compared with the present results. It is done in fig. 3.26 where present π^+ data collected at θ laboratory angles of 65° and 80° are presented together with HARP-CDP results. Whereas HADES data are measured at 3.5 GeV proton energy the beam energy of HARP-CDP experiment was equal to 4.1 GeV.
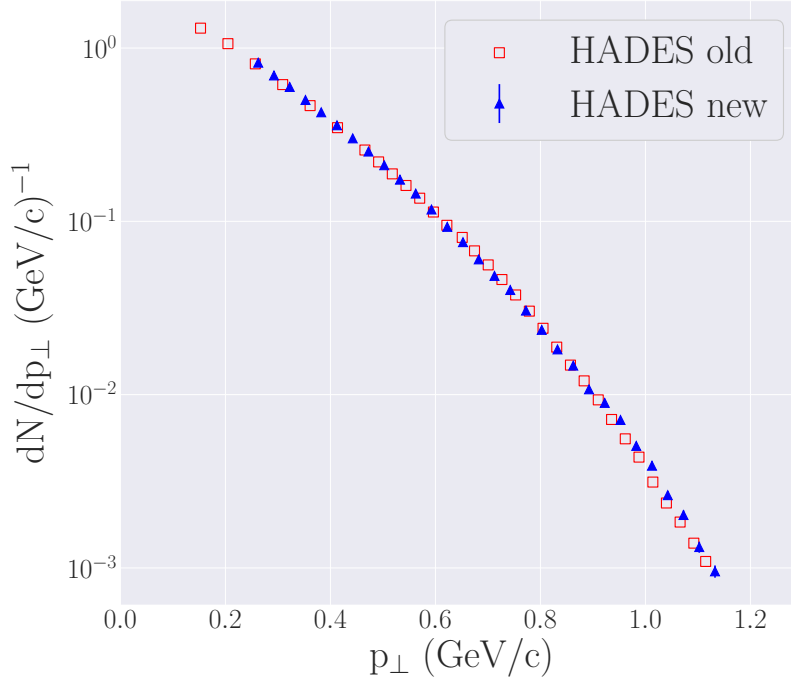
Figure 3.25: The transverse momentum, $p_\perp$, distribution of π^- for the selected rapidity of $0.2 < y_{lab} < 1.8$ measured at HADES in $p + Nb$ at 3.5 GeV proton beam energy. Comparison of the results of current analysis (blue triangles) with the former studies of inclusive π production performed at HADES (red rectangles) [62]. Despite of the various analysis schemes used the results of both of them agree very well.

The shapes of energy distributions of π^+ are practically the same for all three targets. Since the proton beam energies in both experiments were similar the observed differences in the magnitudes of cross-sections are practically only due to target masses. Presented spectra follow expected sequence of increase of the production cross-section with increase of the target mass.

This fact allows the conclusion that the double differential cross-sections for production of π^+ measured at HADES agree well with the similar results obtained by HARP-CDP collaboration.
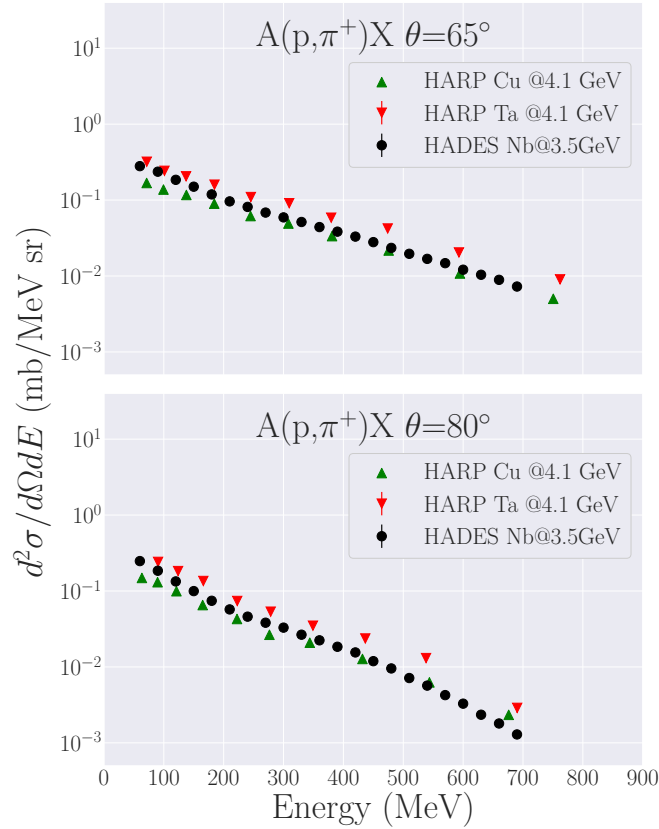
Figure 3.26: Examples of double differential cross-sections measured at two
emission angles ($\theta = 65°$ - upper panel, and $\theta = 80°$ - lower panel) at HADES
for production of π^+ in reaction $p +^{93} Nb$ @3.5 GeV (black dots). They are
compared to the similar results of HARP-CDP collaboration but measured
for 4.1 GeV proton beam impinging on ^{64}Cu (green triangles) [78] and ^{181}Ta
(red triangles) [77] targets. Taking into account the expected cross-section
differences due to various target masses the good agreement of distributions
obtained in both experiments is confirmed.

3.3.3   Low energy spallation data

HARP-CDP collaboration provided also the double differential cross-sections
for proton production in proton induced reactions. This data will be utilized
here to confront the HADES result with the data available in the literature.

In this respect also the results of PISA collaboration [82] are of interest. Data provided by PISA cover broad range of target nuclei (from C to Au) bombarded by protons of 1.2, 1.9 and 2.5 GeV energy [26, 82–86]. PISA experiment registered isotopically identified charged reaction product from ^1H to ^{12}C and heavier intermediate mass fragments identified only by their atomic number. For the aim of performed verification of the HADES results only the hydrogen isotopes of PISA data can be utilized.

Comparison of production cross-section for H isotopes measured in HADES and in PISA is given in fig. 3.27. The examples of production cross-sections for p (upper panel), d (middle panel) and t (lower panel) measured at HADES for $p+^{93}Nb$ @3.5 GeV and registered at laboratory emission angle $\theta = 65°$ are presented. The PISA results shown there as well were measured for reaction of $p +^{nat.} Ag$ @2.5 GeV [82]

The HADES results for protons (upper panel) are compared also to the results of HARP-CDP registered for $p +^{64}Cu$ reaction at 4.1 GeV impinging proton energy [78].

The data of PISA and HARP-CDP are shown in their full available energy range which only partially overlaps with the detection energy range of HADES experiment.

Taking into account the target mass dependence of the cross-sections and the similar beams energies the results of HADES experiment are in very good agreement with those published by PISA and HARP-CDP collaborations.

The agreement of the magnitudes and the slopes of PISA, HARP-CDP and HADES distributions for all registered H isotopes proves the correctness of the data selection and analysis used in this work.

Since the detection conditions during the $p +^{93}Nb$ run at 3.5 GeV beam energy in HADES were not optimized for registration of the single spectra of charged pions and hydrogen isotopes it was demanded to undertake the efforts in order to test if the applied analysis scheme including the particle identification, the background reduction and subtraction, the efficiency and acceptance corrections, the absolute normalization and the error estimation are sufficiently powerful and reliable. Very good agreement of the present data with those published in the literature and obtained in the experiments, which used completely different methods of measurements proves reliability of the present data processing.
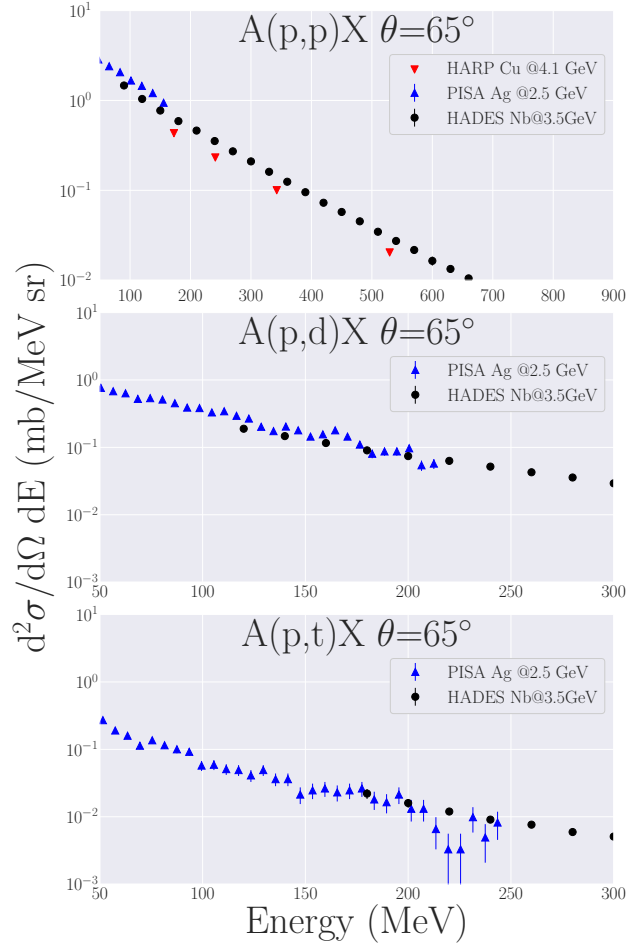
Figure 3.27: Examples of double differential cross-sections for p (upper
panel), d (middle panel) and t (lower panel) measured at HADES at $\theta = 65°$
laboratory emission angle in reaction $p+^{93}Nb$ at 3.5 GeV beam energy. They
are confronted with the former results of spallation experiment PISA [82] for
the same isotopes and detection angle. The double differential production
cross-sections for p are compared also to the results obtained in HARP-CDP
experiment [78].

Chapter 4

Results of HADES experiment

4.1 Double-differential cross-sections from reaction of p+Nb at 3.5 GeV

The double differential cross-section for production of charged pions and isotopes of hydrogen in p+Nb reaction at 3.5 GeV proton beam energy resulting from the analysis of data registered in HADES experiment are shown in figs. 4.1, 4.2 and 4.3. These distributions are effect of the analysis explained in chapter 3.

For the aim of current work the 10^8 events were analyzed. Such high statistics of collected and analysed events permitted to create the $d^2\sigma/d\Omega dE$ distributions for the whole angular range of HADES acceptance, i.e. from $20°$ to $80°$ of the emission angle θ with the angular step of $5°$.

The experimental errors are calculated according to formula 3.3, where only the components depending on PID/background error, efficiency + acceptance error and sector error are considered.

Such defined uncertainty is calculated for each particle type, selected emission angle θ and for each energy bin of 30 MeV of the relevant distributions.

The constant component of systematic uncertainty equal to 15%, resulting from absolute normalisation of HADES data is not included into error bars presented in figures 4.1, 4.2 and 4.3. Statistical uncertainties are insignificant and neglected.

In the following the obtained cross-sections are discussed together with their comparison to the distributions obtained with the use of three theoret-
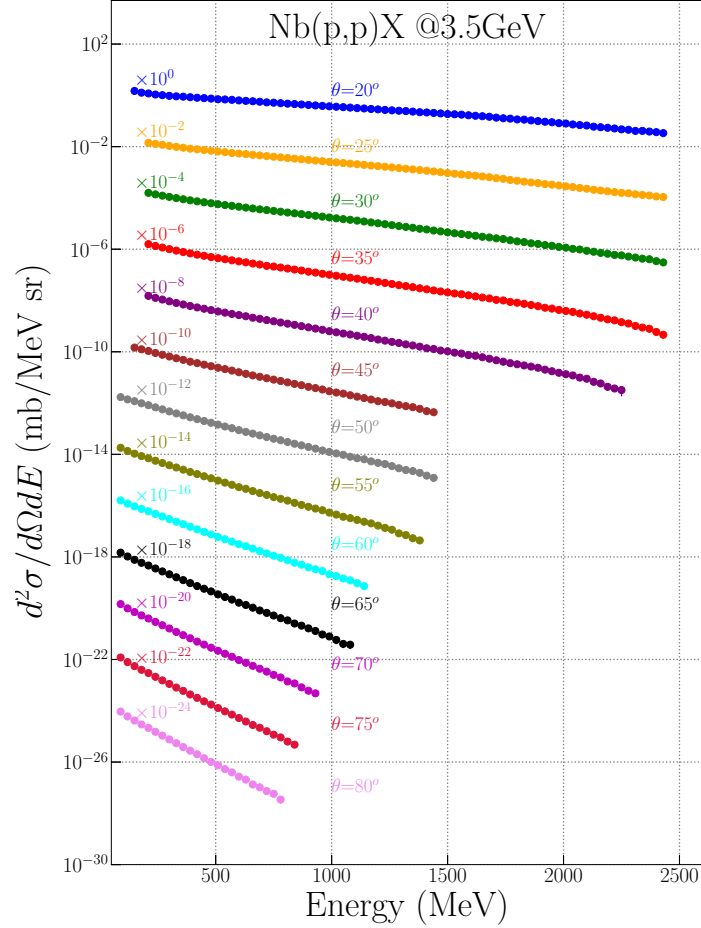
Figure 4.1: Double differential cross-sections of p measured at HADES in $p+^{93}Nb$ reaction at 3.5 GeV incident proton energy (full circles). The distributions measured at emission angles of $20° \leq \theta \leq 80°$ with the step of $5°$ are shown. In order to facilitate the comparison each distribution at higher angle is multiplied by factor of 10^{-2}.

ical models. Provided here huge set of new and precise experimental data extending to the energies beyond of those available up to now in the literature may put strong constraints to each theoretical model which aspires to reasonably well reproduce mechanism of this stage of the reaction process.
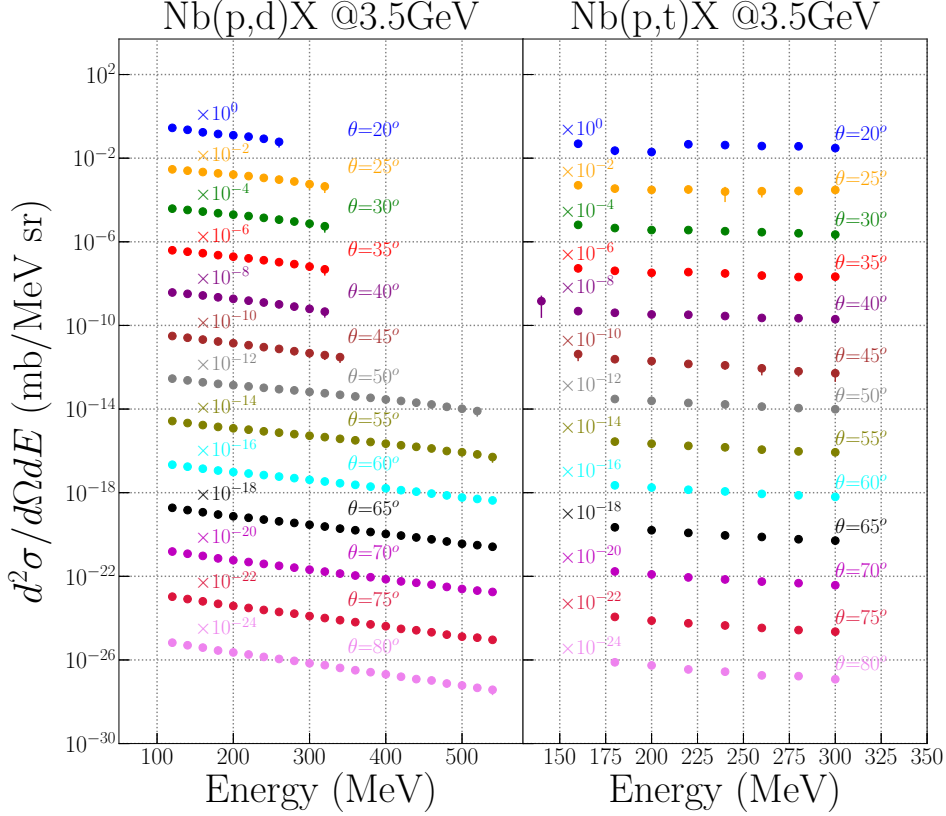
Figure 4.2: Double differential cross-sections of H isotopes: d (left panel) and t (right panel) measured at HADES in $p+^{93}Nb$ reaction at 3.5 GeV incident proton energy (full circles). The distributions measured at emission angles of $20° \leq \theta \leq 80°$ with the step of 5° are shown. In order to facilitate the comparison each distribution at higher angle is multiplied by factor of 10^{-2}.

4.2 Comparison with the models

The processes governing the first stage of proton-target nucleus collision must be reflected in the kinematical distributions of the main reaction products. They are nucleons and pions. In case of this works particle which carry the information about the proceeding of the intranuclear cascade are protons and charged pions. Moreover, the available single particle spectra of the dominant cross-sections are supplemented with the production cross-section
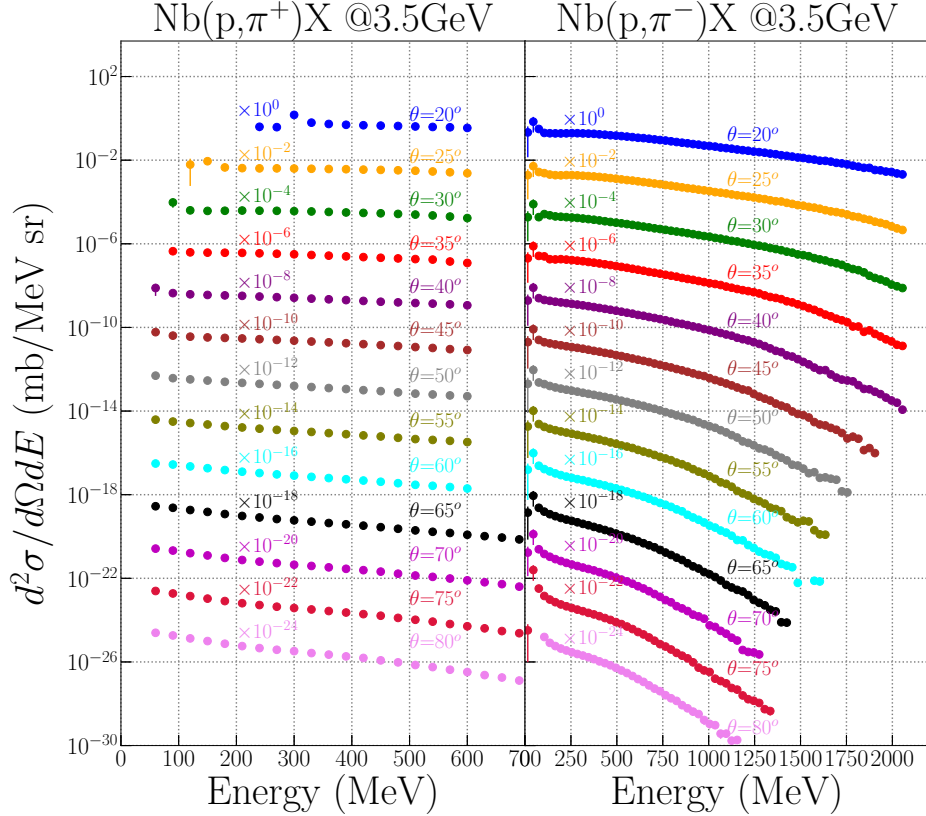
Figure 4.3:   The same as in fig. 4.2 but for π^+ (left panel) and π^- (right panel).

of the composite nuclear products, namely the deuterons and tritons. Their rather high energies and forward emission angles indicate that those clusters are created during dynamical phase of the reaction.

In order to extract the important information about the process of intranuclear cascade the experimental - angular and energy distributions of charged participants of this process, i.e. protons, pions and complex hydrogen isotopes - deuterons and tritons are compared to the predictions of the theoretical models. They are GiBUU [11], UrQMD [13] and INCL++ [10]. These models are commonly used in investigations of nucleus-nucleus collisions at GeV/A energies.

As described in chapter 2 the recalled here models differ in the level of approximation of the physical phenomena appearing in the quantum-

mechanical realm of nuclear systems. They contain some different physics ingredients, and use specific solutions, but in fact they all assume that the intranuclear cascade is a sequence of binary interactions among the involved nucleons and pions.

It has to be stressed here that INCL++ model foresees the mechanism for light composite particle production (surface coalescence - cf. chapter 2.1.1 and [9]) whereas both GiBUU and UrQMD are not equipped with the mechanisms allowing for creation of nuclear clusters.

The most up to date versions of the models were used. It was release 2021 (Feb 8, 2021) of GiBUU, V3.4 for UrQMD and version v6.29-9198542 of INCL++. Also the default settings of each respective model were assumed during all numerical calculations performed in the present study.

4.2.1   Protons and pions

The main charged reaction carriers inside the struck target nucleus available for the analysis in this thesis are the protons and charged pions.

In order to facilitate comparison of their experimental distributions with the theoretical ones their angular and energy distributions of cross-sections are given in this subsection for only three detection angles of $\theta = 25°$, $55°$ and $80°$. It is justified by the fact that the angular dependence of the data is monotonic and smooth.

The uncertainties indicated for all presented here experimental data include only the energy and angle dependent components of systematic error - similarly as it was done for complete sets of the HADES results shown above in the section 4.2 (cf. as well the section 3.2.4). The absolute normalization uncertainty which is constant an equals to 15% is not included to the plots. The insignificant statistical errors are neglected.

Protons

The advantage of the magnetic spectrometer HADES has been fully utilized for selecting the protons emitted from the $p+Nb$ reaction. Achieved here range of their measured momenta extends to much higher values than it was possible in earlier experiments dedicated to measurement of production cross-sections of light nuclear products.

Also their identification suffered the least among all reaction products from the limitation of the identification method based on measuring of the

specific energy losses of particles in the detector medium.

In effect the energy range of the cross-sections presented in this work significantly exceeds the energy limits of proton distributions available in the literature.

Obtained distributions are shown in fig. 4.4. They vary monotonically in the whole detected energy range and their slopes increase with the emission angle θ.

The experimental errors are small. For the logarithmic scale used at the plots mostly they are hidden within the size of the markers.
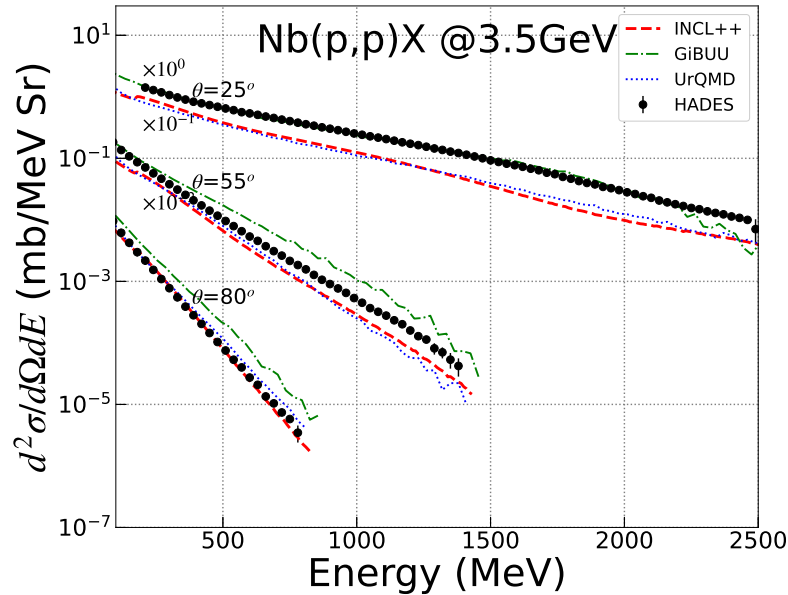
Figure 4.4:   Double differential cross-sections of p measured at HADES in $p+^{93}Nb$ reaction at 3.5 GeV incident proton energy (full circles). Cross-sections are shown for three laboratory emission angles of $\theta=25°$, $\theta=55°$ (multiplied by factor 10^{-1}) and $\theta=80°$ (multiplied by factor 10^{-2}). The experimental distributions are compared to the results of theoretical models: GiBUU (dash-dotted lines), UrQMD (dotted lines) and INCL++ (dashed lines). Constant normalization error of experimental data equal to 15% is not included.

For the forward emission angles all three models provide the proton distributions of the shape which is similar to the experimental ones. But the best agreement with the data is provided by GiBUU model. The theoretical curve follow the data at 25° in the whole presented energy range. The UrQMD and INCL++ model underestimate the magnitude of the data by factor larger than 2. The disagreement of the UrQMD and INCL++ models with the cross-sections measured for protons is largest for highest available energies and decreases with decrease of the kinetic energy of emitted proton.

The GiBUU starts to overestimate the data when the emission angle increases. But predictions of UrQMD and INCL++ get closer to the experimental distribution for larger angles.

For the largest presented here emission angle of 80° the best description of the proton data is provided by INCL++. The worst agreement is observed for GiBUU model. It overestimates the experimental cross-section and the discrepancy increases with the proton energy. Disagreement of factor of $\sim$2 is attained at the end of available data range.

Charged pions

The experimental energy spectra for charged pions are shown in fig. 4.5 (for π^+) and in fig. 4.6 (for π^-).

In general their energy ranges are broader than those provided up to now in experiments performing similar research. The exception is observed for the forward detection angles of π^+. In the present analysis - due to limitation of particle identification (PID) based on dE/dx measurement - these particles can't be effectively identified among other reaction products when their energies exceed $\sim$600 MeV.

At most forward emission angles of π^+ (see fig. 4.5) the theoretical distributions of all three models underestimate the experimental cross-sections. It is most significant for lowest energy. Discrepancies decrease when energy of pions increase. For energies greater than $\sim$500 MeV, results of INCL++ almost follow the data.

The agreement improves with increase of emission angle. All three models follow approximately the shape of experimental spectrum. Theoretical distributions are closest to the data in the range of 250 - 500 MeV of pion energies. In general, for the the mid-angular range of HADES, the models agree with the data within the limit of factor 2.

For the highest detection angles of HADES almost ideal description of
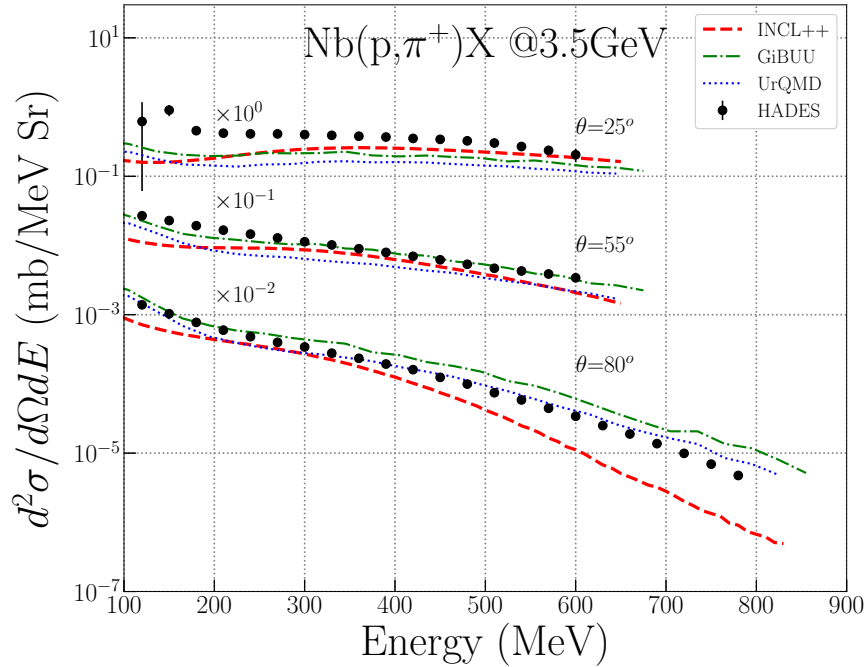
Figure 4.5:   The same as in fig. 4.4 but for π^+.

experimental cross-sections for π^+ is provided by UrQMD model. The most pronounced disagreement is visible for results of INCL++ when the energies of pions are greater than $\sim$500 MeV.

From inspection of fig. 4.6 it can be concluded that the best description of differential production cross-section for π^- is provided by UrQMD model.

It is especially visible at most forward emission θ angle where the agreement is nearly ideal for almost whole available energy range. Only at pion energies smaller than ~ 400 MeV the UrQMD underestimates the pion data.

INCL++ is also rather successful in reproduction of the experimental π^- cross-section. But it is observed only at middle and highest emission angles. However even there, for the lowest and highest energies of detected pions the agreement with the data deteriorates.

The GiBUU model overestimates the π^- data for all their emission angles and energies available in the present work. Except the smallest energies the
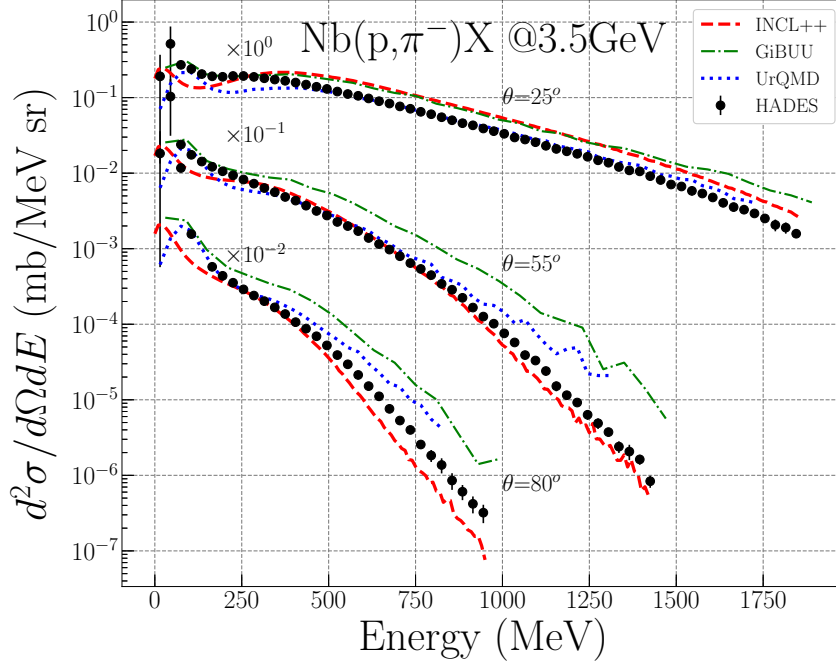
Figure 4.6:   The same as in fig. 4.4 but for π^-.

discrepancies are at least of factor 5.

4.2.2   Composite nuclear particles

The origin of the light composite particles studied in this work (deuterons and tritons) is not understood. The mechanisms responsible for creation of nuclear clusters during the intranuclear cascade are not known. Various hypotheses of more or less theoretically justified background are proposed (see e.g. [39–43]).

In INCL++ model the hypothesis of surface coalescence is applied. It assumes the coalescent origin of composite particles (at least H and He isotopes) which are created still during the pre-thermalization phase of the pA collision.

Surface coalescence of INCL++ model permits the dynamical construc-

tion of the stable nuclear clusters of the masses A$\leq$8. They can be emitted from the target nucleus according to the conditions implied by the values of their binding energies and the height of the Coulomb barrier.

Unfortunately, among the tested theoretical models both GiBUU as well as UrQMD do not contain the mechanisms responsible for creation of composite nuclear particles.

The HADES experimental double differential cross-sections for both the deuterons as for the tritons are limited in energy. It is due to overlapping of their dE/dx distributions with other H isotopes at higher particles energy. Identification of tritons have been especially challenging issue during current analysis. Nevertheless the obtained results (fig. 4.7 for deutrons and for tritons) show the cross-section energy dependence in broader range than that for other deuteron and triton data available up to now.

The results of simulations of the deuteron distributions with the use of INCL++ model (cf. fig. 4.7 - upper panel) overestimate the experimental data. Such disagreement is most pronounced at large emission angles were surface coalescence overestimates the d data by factor $\sim$3.

At most forward emission angles available in HADES the disagreement is small for low energies of deuterons. But it increases towards larger energies attaining factor of $\sim$3 at the energies >300 MeV. In this way the slope of theoretical curve is more flat than for experimental distribution.

The best description of experimental data the INCL++ model and the surface coalescence mechanism provides at middle angles. For the $\theta = 55°$ discrepancy is of factor $\sim$2.

HADES results for t are shown in fig. 4.7 - lower panel. Astonishingly the surface coalescence of INCL++ model predicts better the triton differential production cross-sections than the one for lighter deuterons. The best agreement of experiment and theory is observed tor t emitted at $\theta = 55°$. The theoretical curve agrees with the experimental one for the whole range of registered energies. For lower emission angle the agreement of the model predictions and the data remains quite good but with slight increase of absolute values of discrepancies. At highest detection angles available in this analysis the model starts to overestimate the experiment more visibly. For $\theta = 80°$ the disagreement reaches a factor $\sim$2. In the whole angular range of HADES the slopes of experimental and theoretical distributions are in good agreement.
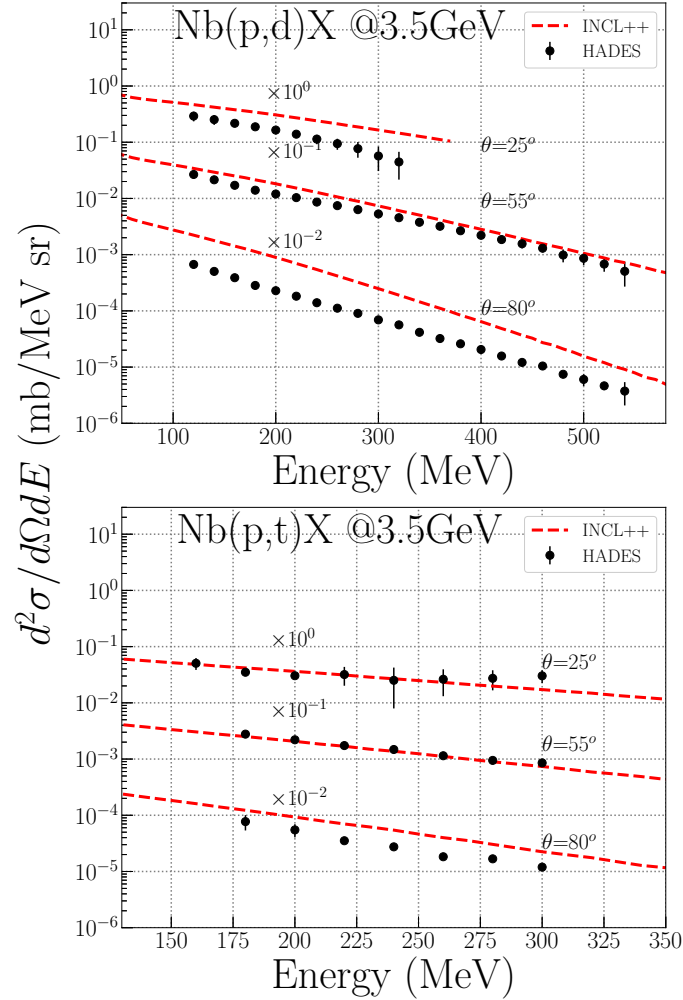
Figure 4.7: Double differential cross-sections of deuterons (upper panel) and triton (lower panel) measured at HADES in $p+^{93}Nb$ reaction at 3.5 GeV incident proton energy (full circles). Cross-sections are shown for three laboratory emission angles of θ=25°, θ=55° (multiplied by factor 10^{-1}) and θ=80° (multiplied by factor 10^{-2}). The experimental distributions are compared to the results of theoretical model INCL++ (red dashed lines). Constant normalization error of experimental data equal to 15% is not included.

4.3 Interpretation of results

The general comparison of the HADES experimental cross-sections for hydrogen isotopes and charged pions and the relevant theoretical distributions of three models has been performed in previous section.

It was found that the shapes of experimental distributions are in most cases reproduced by the models. The absolute values of differences are usually kept within a factor of 2.

Also the expected behaviour of the theoretical distributions like a smooth decrease of the cross-sections with increasing of the scattering angle and the energy of emitted particles is confirmed. Unfortunately, in the whole available kinematic range, no any systematic behaviour of the relationships between experiment and theories can be observed.

In order to perform more detailed assessment of the abilities of theoretical models to predict the experimental data the quantity called A-factor developed in [27, 87] has been applied.

The great advantage of A-factor is that its value quantify the deviation between two discreet distributions of the cross-sections by the number between 0 and 1.

The original formula for A-factor is as follows:

$$A \equiv \frac{1}{N} \sum_{i=1}^{N} \frac{\left| \sigma_i^{exp} - \sigma_i^{th} \right|}{\sigma_i^{exp} + \sigma_i^{th}} \tag{4.1}$$

where σ_i^{exp} and σ_i^{th} are the values of experimental and theoretical cross-section in i-th histogram bin, respectively, and N is the number of histogram bins.

For the aim of the current analysis, where theoretical models are benchmarked both in the domain of laboratory emission angle, θ, as well as in their dependence on the kinetic energy, E, of particles, the A-factor was calculated for each bin of two dimensional histogram θ vs. E:

$$A \equiv \frac{\left| \sigma_i^{exp} - \sigma_i^{th} \right|}{\sigma_i^{exp} + \sigma_i^{th}} \tag{4.2}$$

Averaging over several bins as it is done in formula 4.1 is avoided here. The properties of factor A are as follows:

- it takes values between 0 and 1;

- for $A = 0$ the ideal agreement between compared distributions is observed;

- for $A = 1$ one of the compared cross-sections vanishes or its value become infinite;

- value of A is asymmetric depending on the sign of differences between distributions;

- for the small differences between the compared distributions the mentioned above asymmetry is small;

- in such case the value of calculated A-factor can be interpreted as the approximate of the half of relative distance between the data and theoretical cross-sections;

- when $A = 0.1$ the average relative distance between experimental and theoretical cross-sections is close to 20%;

- for $A = 0.2$ the average deviation of the cross-sections is close to 40%.

In the present studies the experimental and theoretical distributions differ usually within the limits of factor 2. But the individual values of measured cross-sections are charged with uncertainty below 20%. Thus, for this specific analysis, it is reasonable to introduce gradation of quality of predictive power of the models:

- for the calculated value of A-factor below 0.1 (maximal difference of the distribution ~20%) the agreement of two examined distributions is called as "good";

- when $0.1 < A < 0.2$ (maximal difference of the distribution is in the range of ~20% to ~40%) the agreement between distributions is called as "moderate";

- values of $A > 0.2$ call for the conclusion that the agreement between the model and the data is not satisfactory.

The uncertainty of A-factor itself in the current analysis remains below value of 0.1. This uncertainty is due to the experimental errors of measured HADES cross-sections which are usually below 20%.

In figure 4.8 the effect of analysis with the use of A-factor is presented. The contour plots of the A-factor in the kinetic energy (E) - emission angle (θ) plane are shown for emission of protons and charged pions. They were evaluated by means of three models: GiBUU, UrQMD and INCL++.
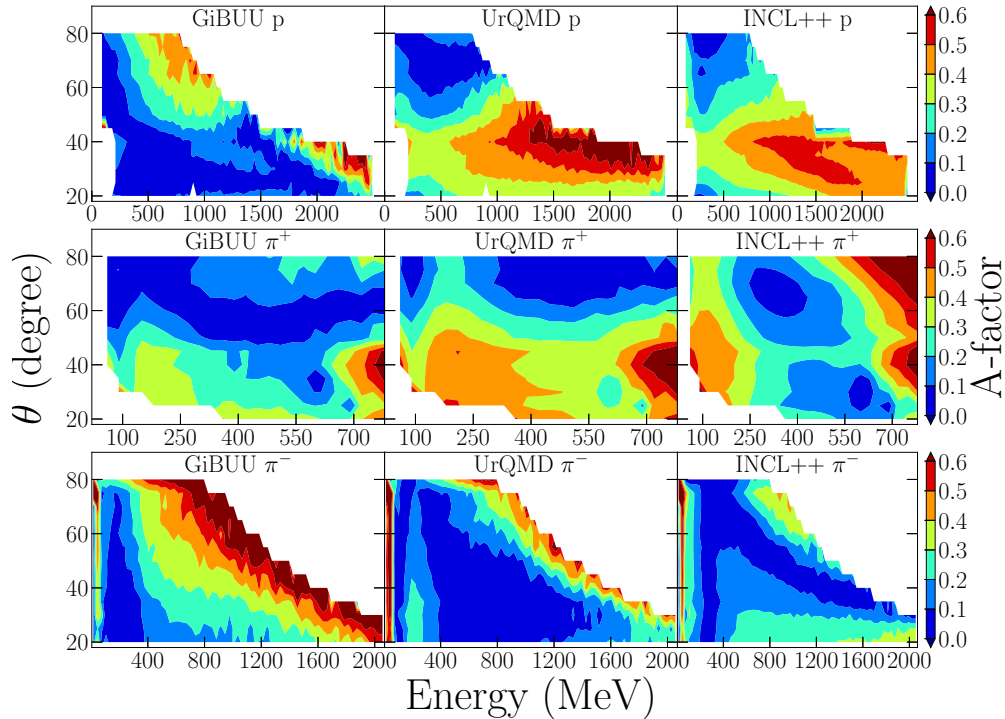
Figure 4.8: Laboratory θ emission angle and kinetic energy E dependent distribution of A-factor (see text) for double differential production cross-section of p (upper row), π^+ (middle row) and π^- (lower row). It is calculated according to formula 4.2 for theoretical models of GiBUU (left column), UrQMD (middle column) and INCL++ (right column) compared to the experimental values of relevant production cross-section measured at HADES. For ideal agreement of the model and the data $A = 0$ and rises with the discrepancy between the data and the model. Good and moderate agreement is observed if $A \leq 0.2$. Note the different energy scales for the figures in different rows.

In the most upper three panels of the figure 4.8 the A-factor values of three models for proton data are shown. The areas of dark-blue and blue colours corresponding to good and moderate agreement between model and

experimental cross-sections are clearly larger for GiBUU than for two other models. It shows that GiBUU is able to provide satisfactory agreement with the data for significantly larger kinematic range of HADES than two other models.

GiBUU reproduces well the data both, at small and large angles and for much broader range of energies for these angles. However at angles larger than 50° it works satisfactory at smaller energy range - up to 400 - 500 MeV.

The regions of small values of the A-factor of UrQMD and INCL++ corresponds only to angles larger than 50° and relatively small energies - smaller than 1000 MeV.

The middle three panels of fig. 4.8, are devoted to data of positively charged pion and their analysis by the same three theoretical models as for protons. Inspection of these panels indicate that the regions of angles and energies well described by GiBUU and UrQMD are very similar. They cover kinematic range for angles larger than 50° (for GiBUU) and larger than 60° (for UrQMD) and for full range of energies (up to 800 MeV).

INCL++ model describes satisfactorily the data for almost all angles, however in limited range of energies. At angles larger than 50° the good and moderate agreement with the data is observed for energies from about 200 MeV to 500 MeV whereas at angles smaller than 40° it is a case for energy span from about 300 MeV to 700 MeV.

The lowest three panels of fig. 4.8 show the analysis with A-factor for negatively charged pions π^- again simulated with GiBUU, UrQMD and INCL++ models (from the left to the right panel of the figure, respectively).

It is clear that each of the models describes well different kinematic regions of reaction. In contrast to emission of protons, GiBUU model reproduces smallest part of the data among other models. The GiBUU simulations of π^- distributions reproduce the data in the whole angular range of HADES only for small energy range which additionally decreases when the emission angle gets larger. At smallest angles of 20° - 25° this energy interval of good and moderate agreement extends from 100 MeV to 600 - 700 MeV. At largest available angles it ranges from about 100 MeV to 250 MeV.

HADES cross-sections of π^- in the broadest kinematical range are reproduced satisfactory well by UrQMD model. Areas with $A < 0.2$ covers full range of the angles whereas range of energies decreases with increasing angle. For smallest angles the energies of satisfactory agreement extend from about 100 MeV to 1700 MeV and at largest angles - from 100 MeV to about 500 MeV.

INCL++ describes well and moderately the π^- data at angles larger than 30° for broad interval of kinetic energies. It extends from 200 MeV to 2000 MeV at 30° but decreases when emission angle increases. At the largest angle of 80° the energy span of satisfactory agreement of model and data ranges only from 200 MeV to 650 MeV.

Conclusions derived from inspection of A-factor distributions for p, π^+ and π^- obtained for three theoretical models are in the perfect agreement with those from the analysis of single distributions of these particles where experimental spectra are compared to model predictions at three angles: 25°, 55° and 80° (cf. figs. 4.4 and discussion in subsection 4.2.1). Such an agreement proves reliability of the present method of reasoning based on two-dimensional maps of the A-factor values.

Similar analysis of A-factor value as a function of energy and emission angle of the reaction product can be performed also for deuterons and tritons. However, the data for emission of these particles can be compared only with predictions of the INCL++ model. As it was informed already in chapter 2 both in GiBUU as in UrQMD models the mechanisms permitting the creation of nuclear clusters during the intranulcear cascade are not implemented.

The maps with A-factor dependence on the product energy and emission angle for deuterons and tritons produced in $p + Nb$ collision at 3.5 GeV in HADES are presented in fig. 4.9. Distribution of the A-factor calculated for INCL++ predictions for deuterons confronted with the HADES data indicates that good and moderate agreement is observed for the all energies of d but emitted in the narrow angular range from about 50° to about 60° of θ laboratory angle. Besides these regions the satisfactory reproduction of d data INCL++ provides for the highest energies and emission angles and for low energies below 250 MeV but only for emission angles between 30° - 45°.

For tritons good and moderate agreement is obtained for all angles larger than about 40°. Additionally the predominantly moderate agreement is visible for energy smaller than approximately 270 MeV and at angles smaller than 40°.

The two dimensional distributions of A-factor allows for extraction further credible information, namely the predictive power (PP) of given theoretical model for selected set of observed particles.

This can be obtained by observation how big is the part of studied kinematic space of energy - emission angle for which the model describes the data in good and moderate manner (A-factor values are smaller or equal to 0.2). The ratio of number of such bins to number of all observed bins is used as
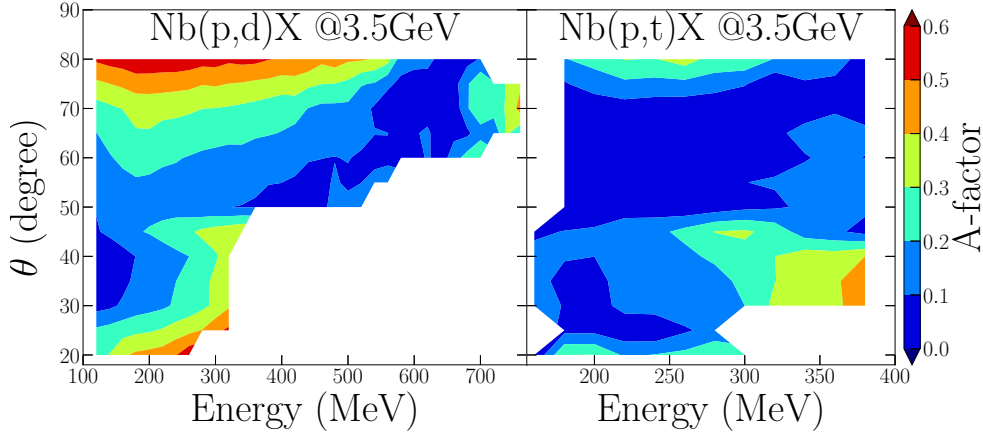
Figure 4.9:   Dependence of A-factor (see text) on the deuteron (left panel) and triton (right panel) emission angle θ and kinetic energy E. A-factor is calculated according to the formula 4.2 for comparison of experimental double differential cross-sections of HADES with the results of theoretical model INCL. For ideal agreement of the model and the data $A = 0$ and rises with the discrepancy between the data and the model. Good and moderate agreement is observed if $A \leq 0.2$.

numerical measure of the predictive power (PP) of given model for selected set of observed particles.

Table 4.1 contains the appropriate percentages of such calculated correctness of individual models for selected individual particles and for their particular and total yields.

From inspection of the table 4.1 the following conclusions can be derived:

- none of the applied theoretical models is able to reproduce "well" (i.e. with $A < 0.1$) at least a half (i.e. 50%) of the full examined in this thesis E-θ space. It is a case both for each individual of observed ejectiles (p, d, t, π^+, π^-) as well as for their combinations ($p + \pi^+ + \pi^-$, $d + t$ and $p + \pi^+ + \pi^- + d + t$);

- GiBUU model reproduces with "good and moderate" quality 65% of p, 58% π^+ but only 28% of π^-. In average over all these particles such quality of description is reached for 49% of E-θ area under investigation;

- UrQMD and INCL++ models reproduce "well and moderately" the p and π^+ distributions in less than 50% situations;

Table 4.1:   Measure of predictive power (PP) of GiBUU, UrQMD and INCL++ models for double differential cross-sections of p, π^+, π^-, d and t measured at HADES. PP is equal to fraction of area (in [%]) of the θ vs. E distributions presented in figs. 4.8 and 4.9 where the agreement of the theoretical model and the experimental specta of HADES is good ($A < 0.1$) or good and moderate ($A < 0.2$). The predictive power for the simulation of intranucelar cascade is given for the sum of p, π^+ and π^- ejectiles. The correctness of reproduction of composite particle production is calculated for the sum of d and t (only for INCL++). The overall agreement of the INCL++ model with the data for all detected in HADES particles is given for the sum of them. The number corresponding to several emitted types of particles were calculated as percentage of "good" bins for given set of particles among all bins corresponding to this set of particles.

Ejectile	GiBUU		UrQMD		INCL++	
	$A < 0.1$	$A < 0.2$	$A < 0.1$	$A < 0.2$	$A < 0.1$	$A < 0.2$
p	39%	65%	13%	25%	5%	19%
π^+	28%	58%	19%	33%	27%	35%
π^-	12%	28%	45%	68%	33%	63%
d					18%	52%
t					43%	76%
$d + t$					27%	60%
$p + \pi^+ + \pi^-$	26%	49%	27%	43%	16%	39%
$p + \pi^+ + \pi^- + d + t$					19%	43%

- π^- data are reproduced "well and moderately" in more than in 50% by UrQMD (68%) and INCL++ (63%) whereas GiBUU is less efficient in this respect. It describes in acceptable manner only 28% of the cross-sections.

It was recently announced [88] that the version of UrQMD model used in this analysis is biased with the error influencing the absolute values of pion spectra by about 15%. Since before completing and submission of this thesis the corrected version of UrQMD has not been provided it was decided to keep here the results of the simulation with the use of UrQMD model in its currently available state.

Taking into account the values of discrepancies between the UrQMD results and the experimental pion data shown in this work the correction of the theoretical results in the range of 15% will not change significantly the conclusions about predictive power of this model.

The studies of the $p + Nb$ reaction at 3.5 GeV based on the data collected in HADES experiment and presented in the last two chapters aimed at better understanding of the dynamics of initial phase of proton - target nucleus reaction and mechanisms acting during this phase of collision. Due to complication of the examined type of reaction the reasoning in this respect is difficult. The derivation of meaningful conclusions is possible only by means of comparison of the shapes and magnitudes of experimental distributions with the theoretical prediction. The examined observable must be sensitive to the mechanisms of interest.

For this aim the angular dependence of energy distributions of the main reaction carriers (p, π^+ and π^-) and the lightest composite particles (d and t) have been measured and compared to the leading contemporary theoretical models (GiBUU, UrQMD, INCL++).

These models differ in the range of approximations of the physical phenomena. Also the level of quantum-mechanical description of the colliding system is different in all these models. But all of them assume that the initial phase of collision proceeds as a sequence of binary interactions among the reaction participants whereas the probability and the final states of individual interactions are governed by the cross-sections measured for interactions

in the vacuum.

The presented above comparison of the experimental and theoretical cross-sections indicates that in general all models are able to reproduce the shapes of the experimental distributions. But they differ in magnitudes and these discrepancies remain usually within a factor of ~ 2. Moreover, the discrepancies of data description, for each model, varies incoherently with the type of produced particle, its energy and emission angle.

Mechanism of surface coalescence responsible for clustering in INCL++ models, which anyway suffers from usage of an arbitrary selected and tuned free parameters is only partially able to reproduce the experimental distributions of d and t spectra.

In general it seems that the assumption about intranuclear cascade as a sequence of binary interactions supplemented with a coalescence for cluster production is to some extent justified. But such scenario of the first step of spallation reaction does not fulfill all the degrees of freedom needed for reproduction of the experimental data.

Thus, it has to be concluded that at the current stage of the theoretical examination of intranuclear cascade the precision of the models is still not sufficient in order to define all mechanisms responsible for energy dissipation, particle production, their emission and clustering of nuclear matter.

Chapter 5

Mechanisms of isotropic emission of IMF and heavy target remnants

It was shown in the chapter 4 that all examined models of the first reaction stage, i.e. INCL++ [10], UrQMD [12, 13] and GiBUU [11] are almost equivalent in description of the double differential cross-sections for production of light charged particles (LCP). Among these models, the INCL++ has the technical advantage that it can be easily coupled with the de-excitation models such as ABLA [20], GEMINI [21, 22], GEM [23, 24] and SMM [25]. Moreover, a hypothesis of coalescence is included for the formation and emission of lighter composite particles (A<8) during the first stage of reaction.

In this chapter, presented are the results of the analysis of $^{136}Xe+p$ reaction at energy of 1 GeV/nucleon [89], confronted with the model predictions for the emission of intermediate mass fragments (IMF) and heavy target residues.

The present analysis was performed in the framework of the two-step microscopic models. The first step of the reaction was simulated by INCL++ (v5.3), which describes the intranuclear cascade of nucleon-nucleon and pion-nucleon collisions. This process leaves an excited heavy remnant in the equilibrium stage. Later, the de-excitation of the equilibrated heavy remnant is simulated by 4 different theoretical models [20, 22, 24, 25].

The data studied here cover a very wide range of produced elements, from Li (Z = 3) to Ba (Z = 56). This work is a continuation of the recent study [87], where the same reactions were analyzed at lower energy (0.5

GeV/nucleon). At that time, the examined data [90] included only heavy reaction products, i.e. nuclei from Nb (Z = 41) to Ba (Z = 56). It was found that all the used theoretical models provided reasonable qualitative agreement with the data, although perfect quantitative agreement was not achieved.

5.1   Analysis of isotopic cross-sections

The calculations of the isotopic production cross-sections measured by Napolitani et al. [89] for the system $^{136}Xe+p$ at 1 GeV per nucleon were performed with default values of the parameters of all the models. Therefore it was possible to judge about the predictive power of the applied models. Results of the calculations are presented in figures 5.1, 5.2 and 5.3 for light (2 < Z < 15), intermediate mass (14 < Z < 33) and heavy (32 < Z < 57) reaction products, respectively. The qualitative agreement of the theoretical cross-sections with the data will be discussed below for each range of the products separately.

It is obvious from the inspection of fig. 5.1 that the GEM2 model underestimates systematically all the data. Furthermore, the theoretical cross-sections decrease much faster with increasing of the atomic number Z than the data. In result the theoretical cross-sections of GEM2 are negligibly small for Z > 9.

The isotopic cross-sections predicted by other models do not deviate so significantly from the data. Especially, there is not visible such a systematic underestimation of the data as well as its increase with the atomic number. All the models produce bell shaped mass distributions of the isotopic cross-sections similar to the distributions of the experimental cross-sections. However, none of the models reproduces exactly the behaviour of the data.

Absolute values of the cross-sections predicted by ABLA07 for Z < 9 are smaller than those of the data (with exception of the carbon and oxygen isotopes which seem to be well reproduced). The shape of the mass distributions is reasonably well reproduced for given element with exception of fluorine, where the distribution is shifted towards small masses, and aluminium as well as silicon, where the theoretical distributions are too broad.

The SMM model systematically under-predicts the cross-sections for heaviest isotopes whereas it overestimates the cross-sections for lightest isotopes (with exception of nitrogen where all the models do not work well).

GEMINI++ seems to produce proper width and position of the cross-section distributions, however, it usually under-predicts values of the cross-sections.

The situation is different for elements with $14 < Z < 33$. The experimental and theoretical mass distributions of the isotopic cross-sections are presented for these elements in fig. 5.2. As can be seen there the GEM2 model does not produce any elements with $Z < 30$ (Zn). Starting from Zn the theoretical cross-sections evaluated with GEM2 appear to be non-negligible but they are more than one order of magnitude smaller than the experimental ones. Thus, the GEM2 cross-sections for the discussed range of elements are completely unrealistic.

Other models predict the cross-sections which are of the same order of magnitude as the data and, furthermore, the shapes of the mass distributions of the theoretical cross-sections are similar to the shapes of experimental distributions. Nevertheless the systematic deviations of the theoretical cross-sections from the data are observed.

The mass distributions produced by ABLA07 are too broad in the comparison to the experimental ones. This always leads to the overestimation of the isotopic cross-sections for all isotopes with mass larger than the most populated one and frequently also for isotopes with the smallest masses.

The opposite situation is observed for the cross-sections predicted by the SMM model. In this case the cross-sections for isotopes with the smallest mass are systematically overestimated whereas those for the largest masses are systematically underestimated. Thus, in spite of the similarity of the shape of the mass dependence produced by the SMM model and that observed in the experiment, the absolute values of the cross-sections are systematically overestimated or underestimated by the model.

Position of the maximum of the mass distribution of the isotopic cross-sections as well as its width is in most cases well reproduced by GEMINI++, however, this model systematically under-predicts the absolute values of the cross-sections. This is most pronounced in the neighbourhood of the maxima of the distributions.

The following qualitative conclusions may be derived from inspection of fig. 5.3 which presents the isotopic cross-sections measured and calculated for the elements with $32 < Z < 57$. The magnitude of the cross-sections predicted by GEM2 model increases with increase of the atomic number of the products. At $Z = 33$ the model cross-sections are an order of magnitude smaller than the experimental ones but starting from $Z = 40$ they start to
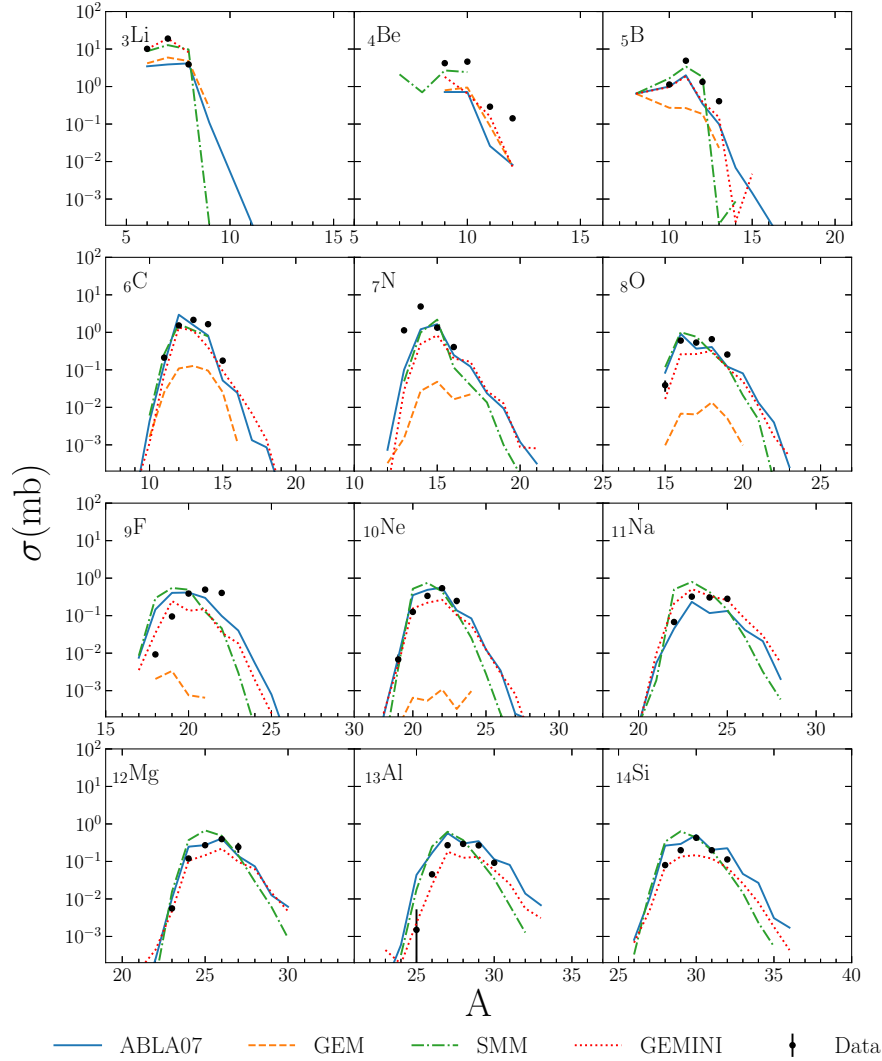
Figure 5.1: Isotopic cross-sections of IMFs with Z = 3–14 from $^{136}Xe+p$ collisions at energy $T(^{136}Xe) = 1000$ A MeV [89] (black dots) together with predictions of the INCL++ (version 5.3) model for the first stage of the reaction coupled to four models of the second stage of reaction: ABLA07 (blue solid line), GEM2 (orange dashed line), GEMINI++ (red dotted line) and SMM (green dashed-dotted line). Note the absence of the theoretical values provided by GEM2 for elements with Z > 10.
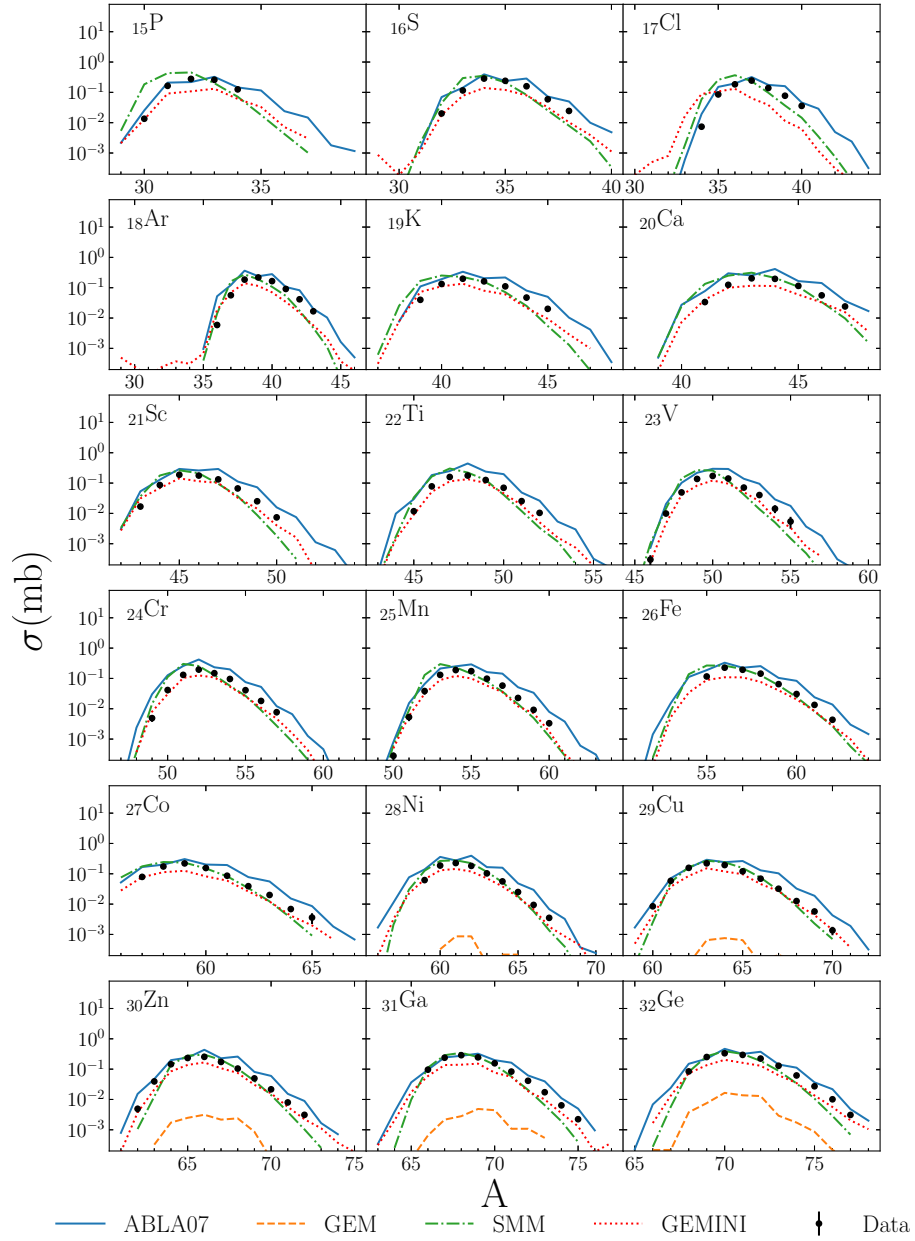
Figure 5.2: The same as in fig. 5.1, but for Z = 15–32. Note the absence of the theoretical values provided by GEM2 for elements with Z < 28.
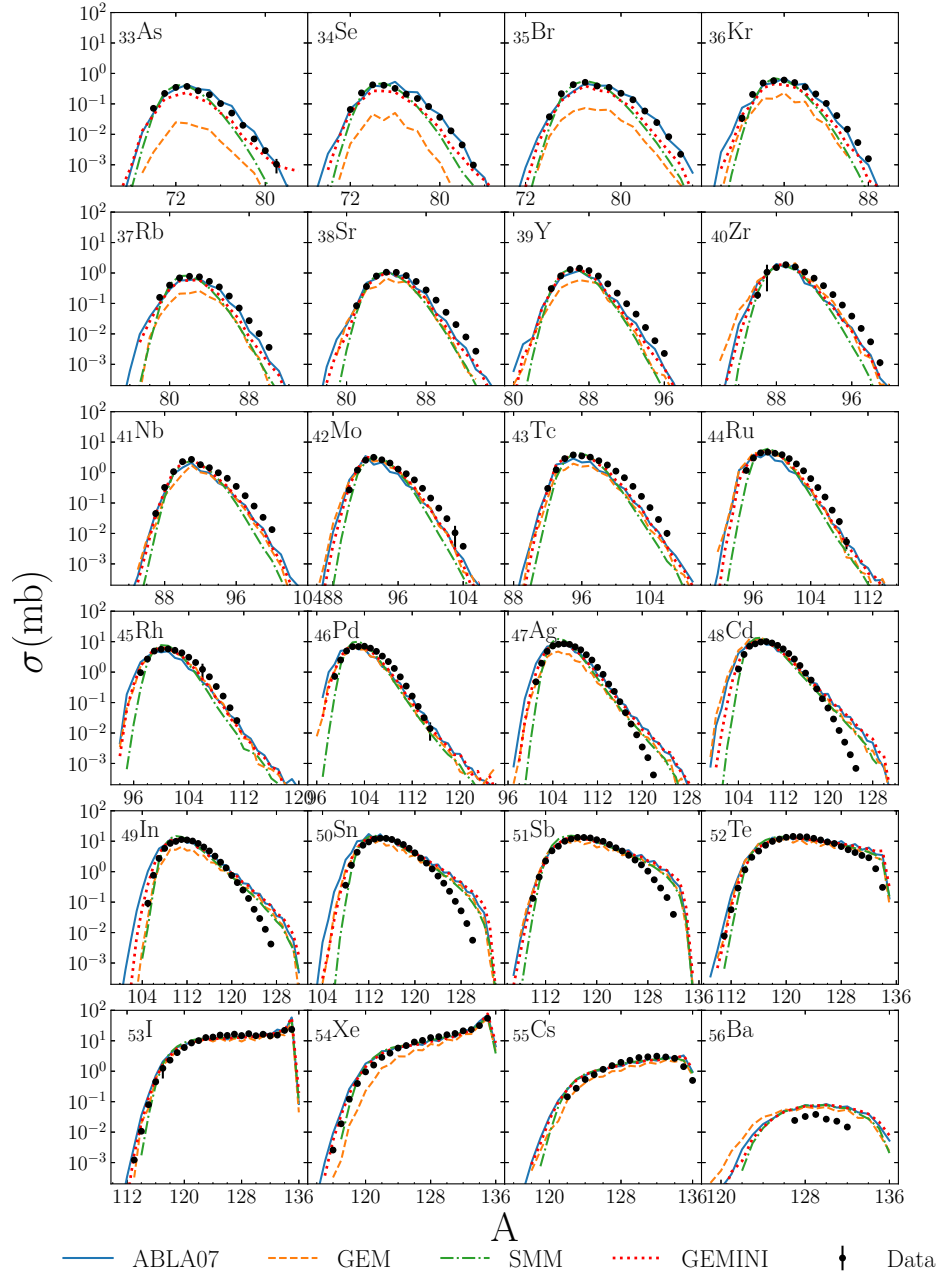
Figure 5.3: The same as in fig. 5.1, but for Z = 33–56.

agree quite well with the data. The shape of the mass distribution of the isotopic cross-sections predicted by GEM2 for Z > 40 becomes quite similar to that of the experimental one which is smooth and almost symmetrical up to Z = 47 (Ac).

The other models, i.e., ABLA07, SMM and GEMINI++ reproduce well the shape of the mass dependence and position of its maximum for all elements starting from Z = 33 (As) up to Z = 46 (Pd). However, the width of the mass of theoretical and experimental distributions agrees only for ABLA07 and GEMINI++. The SMM model usually produces too narrow distributions.

The experimental mass distributions for the range of Z = 47 to Z = 52 of atomic numbers of nuclides (i.e., $Ac - Te$) become asymmetric with the larger values of the cross-sections for the isotopes with large mass number. This behaviour is only partly reproduced by the theoretical models. All of them predict too flat distributions in comparison to the experimental ones.

As a consequence the values of the experimental cross-sections agree well with the model cross-sections for the lightest isotopes of a given element. They are slightly underestimated for isotopes with average masses and are significantly overestimated (even two orders of magnitude) for the heaviest isotopes.

The situation changes for reaction products with the largest atomic numbers, i.e., for Z = 53 and Z = 54 (I and Xe). In this case the distribution of the isotopic cross-sections monotonically increases with the mass of the isotopes. All the models reproduce this change of the character of the distributions as well as the magnitude of the cross-sections. The GEM2 model seems to be the poorest in reproduction of Xe (Z = 54) isotopic cross-sections, however it describes well the isotopic cross-sections for I (Z = 53) and Cs (Z = 55). The experimental distribution of the isotopic cross-sections for the element with the largest Z (Z = 56), i.e., for Ba, is systematically overestimated by all theoretical models.

5.2 Predictive power of the de-excitation models

The detailed discussion of the agreement between model and experimental isotopic cross-sections presented above does not permit to make a simple,

general overview of the quality of description of the data by all examined models. To allow for such an overview the following procedure was applied.

All isotopes for which the production cross-sections were determined in the experiment [89] are presented as empty circles in the two dimensional plot (Z-N) in fig. 5.4. The isotopes for which the model cross-sections do not deviate more than 10% from the data are shown as full circles.

This specific value of the relative deviation was chosen somewhat arbitrary taking into consideration that the typical relative errors estimated for the most abundant isotopes in the experiment [89] are equal to 5%–6% and do not overcome 20%.

It may be concluded after inspection of fig. 5.4 that such a representation allows to observe characteristic behaviour of the quality of data reproduction by different models:

i) The number of well described data is rather small. About 12% of the experimental cross-sections are well reproduced by ABLA07, SMM and GEMINI++ whereas only about 4% in the case of the GEM2 model.

ii) The cross-sections for products with large atomic number Z are more frequently reproduced by the models than those for products with small Z. This is especially pronounced in the case of GEM2 where the only reproduced experimental cross-sections are those for large Z.

iii) In the case of GEMINI++ several neighbouring isotopes of the same element with the large Z are very well reproduced. This is however not the case for other models. It indicates that for these elements GEMINI++ well reproduces the shape of the N-dependence of the experimental cross-sections (at least for the largest N values, cf. fig. 5.3). A quite different situation is present for SMM where two or three lines of well reproduced (Z-N) cross-sections are visible. It is caused by the fact that the shape of the mass dependence of isotopic cross-sections predicted by SMM is different than the experimental shape. Due to this fact the experimental and theoretical N distributions for given Z are crossing at two or three N values (cf. fig. 5.3).

iv) The data for elements with $30 < Z < 40$ are not reproduced by GEMINI++ and GEM2 but the ABLA07 and SMM predictions agree well with the data.

v) The data for elements with $20 < Z < 30$ are not described by GEM2 and ABLA07 whereas SMM and GEMINI++ work well for this range of the atomic number.

vi) Isotopic cross-sections for elements with $10 < Z < 20$ are not reproduced by GEM2 but some of them are well described by other models.

It is worth emphasizing that different models describe well different isotopes for this range of atomic number: GEMINI++ is good for the smallest N-values whereas ABLA07 and SMM for average N. ABLA07 and SMM reproduce well the maximal isotopic cross-sections for given Z. This specific behaviour is caused by the shift of the mass distributions produced by ABLA07 and SMM towards small N values with respect to the experimental distributions - cf. fig. 5.1.

Another representation of the quality of the model predictions for the isotopic cross-sections is application of the A-factor (defined in chapter 4, formula 4.1). As it was discussed there values of the A-factor for well predicted cross-sections are close to zero.

The A-factor values calculated in this investigation for all the data and for corresponding combinations of models are presented in fig. 5.5.

As can be seen in this figure the A-factor evaluated for the GEM2 model cross-sections differs strongly from all others cases. It has values close or equal to one for all elements with Z between 9 and 30. This is due to the fact that GEM2 does not produce ejectiles in this range of the atomic number Z.

Other models, which better reproduce the data provide smaller values of A-factor varying between 0.1 and 0.6.

The following interesting conclusions may be derived from inspection of fig. 5.5:

i) The data with $47 < Z < 55$ are equally well reproduced by all the models. This is the range of elements which are mainly produced by the evaporation of nucleons from the excited remnant of the intranuclear cascade.

ii) For products with $40 < Z < 47$ the GEMINI++ model is the best in reproducing the data. The SMM is the worst one in this respect. Results of ABLA07 are randomly better or poorer than those of GEM2.
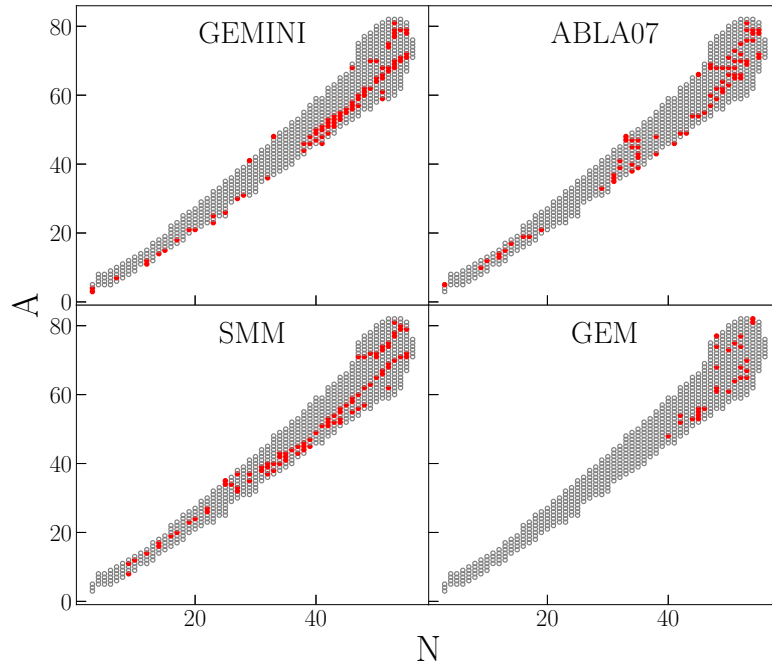
Figure 5.4: The values (Z,N) of experimentally obtained isotopic cross-section in [89] for $^{136}Xe+p$ reaction at energy 1 GeV/nucleon (empty circles). The values (Z,N) at which the relative deviation between theoretical (σ^{th}) and experimental (σ^{exp}) cross-sections calculated as $2 \cdot \left|\sigma^{th} - \sigma^{exp}\right| / (\sigma^{th} + \sigma^{exp})$ is smaller than 10% are marked with full red circles. The left upper panel contains results of GEMINI++, the right upper panel contains results of ABLA07, the left lower panel contains results of SMM and the right lower panel contains those of GEM2.
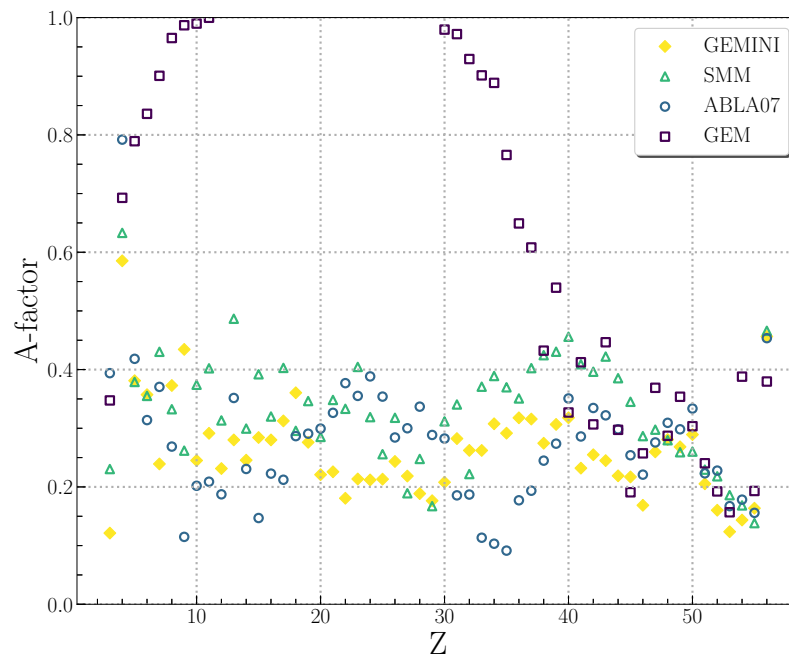
Figure 5.5: Values of the A-factor evaluated according to equation 4.2. Blue, open circles represent results obtained for ABLA07, violet open squares correspond to GEM2, green open triangles to SMM whereas yellow solid diamond show values calculated for GEMINI++ results.

iii) The ABLA07 gives distinctly the best description of the products with $30 < Z < 40$. GEMINI++, SMM and GEM2 lead to the poorer reproduction of the data with the quality decreasing in the indicated sequence.

iv) The situation changes for products with $18 < Z < 30$ where the GEMINI++ offers the best description of the data. ABLA07 and SMM compete to provide second the best reproduction of the experimental cross sections. The GEM2, which does not produce ejectiles for this range of atomic number is completely not applicable.

v) The lowest range of atomic numbers, i.e., $Z < 19$ seems to be the best described by ABLA07 whereas GEMINI++ and SMM give comparable, slightly poorer description.

Table 5.1: Ranks of theoretical predictions of examined in this study models for isotopic distributions of residua from $Xe+p$ collisions at 1 GeV/nucleon [89] according to values of the A-factor. For explanation see text.

Ejectile	The ranks of the models			
	ABLA07	GEM2	GEMINI++	SMM
$_3$Li	4	3	1	2
$_4$Be	4	3	1	2
$_5$B	3	4	2	1
$_6$C	1	4	2	3
$_7$N	2	4	1	3
$_8$O	1	4	3	2
$_9$F	1	4	3	2
$_{10}$Ne	1	4	2	3
$_{11}$Na	1	4	2	3
$_{12}$Mg	1	4	2	3
$_{13}$Al	2	4	1	3
$_{14}$Si	1	4	2	3
$_{15}$P	1	4	2	3
$_{16}$S	1	4	2	3
$_{17}$Cl	1	4	2	3
$_{18}$Ar	1	4	3	2
$_{19}$K	2	4	1	3

Continuation of Table 5.1				
Ejectile	ABLA07	GEM2	GEMINI++	SMM
$_{20}$Ca	3	4	1	2
$_{21}$Sc	3	4	1	2
$_{22}$Ti	3	4	1	2
$_{23}$V	2	4	1	3
$_{24}$Cr	3	4	1	2
$_{25}$Mn	3	4	1	2
$_{26}$Fe	3	4	2	1
$_{27}$Co	3	4	2	1
$_{28}$Ni	3	4	1	2
$_{29}$Cu	3	4	2	1
$_{30}$Zn	3	4	1	2
$_{31}$Ga	1	4	3	2
$_{32}$Ge	1	4	3	2
$_{33}$As	1	4	2	3
$_{34}$Se	1	4	2	3
$_{35}$Br	1	4	2	3
$_{36}$Kr	1	4	2	3
$_{37}$Rb	1	4	2	3
$_{38}$Sr	1	4	2	3
$_{39}$Y	1	4	2	3
$_{40}$Zr	3	2	1	4
$_{41}$Nb	2	3	1	4
$_{42}$Mo	2	3	1	4
$_{43}$Tc	2	4	1	3
$_{44}$Ru	3	2	1	4
$_{45}$Rh	3	1	2	3
$_{46}$Pd	3	2	1	3
$_{47}$Ag	1	4	1	3
$_{48}$Cd	3	2	1	3
$_{49}$In	3	4	1	1
$_{50}$Sn	3	3	2	1
$_{51}$Sb	2	4	2	2
$_{52}$Te	3	3	3	1
$_{53}$I	3	1	3	2
$_{54}$Xe	3	4	2	1

Continuation of Table 5.1				
Ejectile	ABLA07	GEM2	GEMINI++	SMM
$_{55}$Cs	2	4	2	1
$_{56}$Ba	2	4	2	2
Sum of ranks	116	195	91	138
Average rank:	2	4	1	3

To summarize this analysis quantitatively, the ranks of the models based on values of the A-factor were collected in table 5.1. A smaller rank of the model for a given element means that the model leads to a smaller value of A-factor, thus provides the better description of the data.

If two models give practically the same value of the A-factor then the arithmetic average of their ranks is quoted in table 5.1 for both models.

The sum of the ranks for a given theoretical model for all observed elements can be treated as a quantitative measure of the quality of its data description.

As can be learn from table 5.1 the quality of the overall description of the examined data is the best for GEMINI++ (sum of the ranks is equal to 91). The second place in the description of experimental data is granted to ABLA07 (sum equal to 116). The third in this respect is SMM (sum equal to 138) and the poorest description of the data is obtained with the use of GEM2 model (sum of ranks equal to 195).

5.3 Conclusions about examined second step reaction models

A very rich set of production cross-sections (over 600) measured by Napolitani et al. [89] with isotopic identification of the products for $^{136}Xe+p$ collisions at 1 GeV per nucleon was compared with predictions of a two-step reaction scenario simulated with microscopic theoretical models.

The first stage of the reaction was analyzed in the frame of the INCL++ model [9]. It treats the proton-nucleus collision as a sequence of nucleon-nucleon and nucleon-pion collisions leaving the equilibrated, excited remnant nucleus.

The description of the second stage of the reaction was tested with the use of four different models: ABLA07 [20], GEM2 [23, 24], GEMINI++ [21, 22]

and SMM [25]. They assume different scenarios of the de-excitation process of the intranuclear cascade remnant.

All calculations were performed using the default values of the applied theoretical models with the aim to study the predictive power of the models in respect to the determination of isotopic cross-sections.

It was found that ABLA07, SMM and GEMINI++ reproduce the main properties of the Z and A dependence of the cross-sections for reaction products which cover very broad range of elements (from $_3Li$ to $_{56}Ba$) whereas the GEM2 gives comparably good predictions only for lithium and for the elements with large atomic number (Z > 40).

This is illustrated by figs. 5.1, 5.2 and 5.3, which present the data and the theoretical cross-sections for separate ranges of atomic number Z of the products. Inspection of these figures allows to estimate qualitatively the agreement between the data and the model predictions.

A very good quantitative reproduction of the experimental isotopic cross-sections, i.e., such which results in the relative deviation between the data and the model cross-sections smaller than 10%, was achieved only for a small part of all the cross-sections as it is shown in fig. 5.4.

The models ABLA07, SMM and GEMINI++ offer such a perfect reproduction of data for approximately 12% of the products whereas GEM2 only for approximately 4%. This suggests that the models under consideration cannot be approved if the main criterion would be the perfectness of the cross-sections prediction for isotopically resolved reaction products.

Better but also not perfect prediction of the cross-sections was found when the average agreement over isotopes of given element is considered. Such a quantitative comparison of the model and experimental cross-sections was achieved by the application of the *A*-factor which was described in chapter 4.

The Z-dependence of the *A*-factor presented in fig. 5.5 shows that the production cross-sections of elements with largest atomic numbers are equally well reproduced by all applied models. The situation changes for smaller atomic numbers. Then the different models assure the best description for different ranges of the atomic number of products.

The ranking of models based on achieved values of the *A*-factor was made (cf. table 5.1) which clearly shows that the averaged over isotopes and elements agreement between the data and experimental cross-sections is the best for GEMINI++. The ABLA07 and SMM produced poorer average agreement and the GEM2 is the worst.

These conclusions agree with result obtained in the work [87] in which the analysis of the data measured at lower energy, i.e., 500 MeV per nucleon for the same nuclear system were investigated. But then only elements with Z > 40 were studied.

Chapter 6

The yields of non-equilibrium and equilibrium processes in spallation reactions (IMF)

6.1 Introduction

In chapter 4 the predictive capabilities of the different spallation models describing the first stage of reaction were tested with a new measured data set for production of p, d, t, π^+ and π^- in reaction of $p+Nb$.

In chapter 5 the models of de-excitation of products of the first stage of reaction are validated. It is done by means of simulations of the isotopic total production cross-section of IMF and heavier residues of atomic number from Z = 3 to Z = 56. They were produced in the reaction of $^{136}Xe+p$ at Xe beam energy of 1 GeV/nucleon.

In all the above studies a two-step mechanism of the reactions was postulated. The first stage of the collisions proceeded as non-equilibrium process - cascade of nucleon-nucleon and nucleon-pion interactions which lead to a single, equilibrated but excited heavy remnant nucleus. This nucleus in the second stage of the process could evaporate nucleons, light and heavy particles and could as well undergo the fission or (multi-)fragmentation.

As it was described in the previous section, such scenario of the reaction was able to reproduce the main properties of the mass dependence of total isotopic cross-sections.

Furthermore, two specific observations might be done as concerns models

of the second step of the reaction:

(i) the best reproduction of the data is assured by GEMINI++ model, and (ii) the GEMINI++ is the only model which provides the cross-sections values not overestimating the experimental ones.

Very similar observations were published in [91] after investigation of huge set of experimental data for $p+Ag$ collisions at beam energy of 480 MeV, measured by Green et al.[29].

The first observation may lead to the conclusion, that the mechanism realized in GEMINI++ is the closest to reality. The second observation may indicate that some additional mechanisms besides the equilibrium processes are necessary in the second stage of the spallation reaction.

Such non-equilibrium processes were indeed observed in proton induced spallation on many target nuclei starting from Al [86] , Ni [85], to Ag [82] and Au [26].

Unfortunately, no microscopic models of such processes exist. Thus, the observed phenomena were described by phenomenological models of moving source which parameters must be adjusted to the experimental double differential cross-sections $d^2\sigma/d\Omega dE$.

In the present chapter the extension of the studies described in the previous chapters is proposed. It consists in supplementing of the microscopic contributions realized by INCL++ (for the first stage of reaction) and GEMINI++ (for the second stage of the process) by the phenomenological moving source contribution. The properties of moving source are determined from the fit to the experimental double differential cross-sections $d^2\sigma/d\Omega dE$ of $p+Ag$ collisions at 480 MeV proton energy, provided by [29].

The main motivation of this chapter is to further investigate the same data in order to search for the missing contribution of the possible processes, understand their nature and their dependence on the properties of the emitted particles in terms of A, Z and the third component of the isospin T_3.

To achieve this goal, it is of utmost importance to calculate the total production cross-section of the IMF with possibility to extract the contribution of the non-equilibrium stage.

In the experiment of Green *et al.* [29], the double differential cross-sections ($d^2\sigma/d\Omega dE$) were measured for different scattering angles ranging from 10° to 160°. The differential cross-section has a smooth energy and angle dependence, so interpolation and extrapolation of the cross-sections for different emission angles were performed in order to determine the total cross-section.

6.2 Extracting the experimental total production cross-sections

The source of missing mechanism and its contribution to the total cross-section can be evaluated using the phenomenological models. To reconstruct the total production cross-section from experimental data, the simulated cross-section values of GEMINI++ ($d^2\sigma/dEd\Omega$) were supplied by incoherent addition of isotropic emission from highly excited Maxwellian source (or two sources) moving along the beam direction.

The source parameters: velocity, an apparent temperature T, its contribution to the total cross-section, and the parameters responsible for the Coulomb barrier that hinders the emission of ejectiles from the source were chosen to reproduce the experimental spectra of the given ejectiles at all scattering angles simultaneously. Details of the moving source model and the interpretation of its parameters can be found in the appendix of Ref. [83].

The data were reproduced very well, with most of the data achieved using only one moving source contributions. This is illustrated by fig. 6.1 in which experimental (filled circles) and model (lines) energy spectra of ^{18}O particles are depicted at three scattering angles: 20°, 90° and 160°. As can be seen, the equilibrium emission evaluated according to GEMINI++ [21, 22] coupled to INCL++ [10] model (solid, blue line) gives practically isotropic contribution whereas the non-equilibrium emission represented by single moving source (dashed, red line) dominates at forward scattering angles but it is much smaller than equilibrium cross-sections at backward angles. The sum of both contributions (solid, black line) satisfactorily well reproduces the data.

Only the 10 lightest IMF among all 39 studied particles, *i.e.*, $^{6,7}Li$, $^{7,9,10}Be$, $^{10,11,12}B$ and $^{11,12}C$ needed application of two moving sources for the good reproduction of energy spectra at all investigated scattering angles from 20° to 160°. An example of obtained quality of the data reproduction is presented in fig. 6.2 where the energy spectra of ^9Be emitted at the same scattering angles as in fig. 6.1, i.e., 20°, 90° and 160° are shown.

The equilibrium emission contribution represented by solid, blue line is in this case significantly smaller than the data for all scattering angles. For forward scattering angle and small energies the slower of both moving sources gives dominating contribution - shown as a dashed, red line - whereas the contribution of faster of the moving sources - depicted as a dotted, magenta
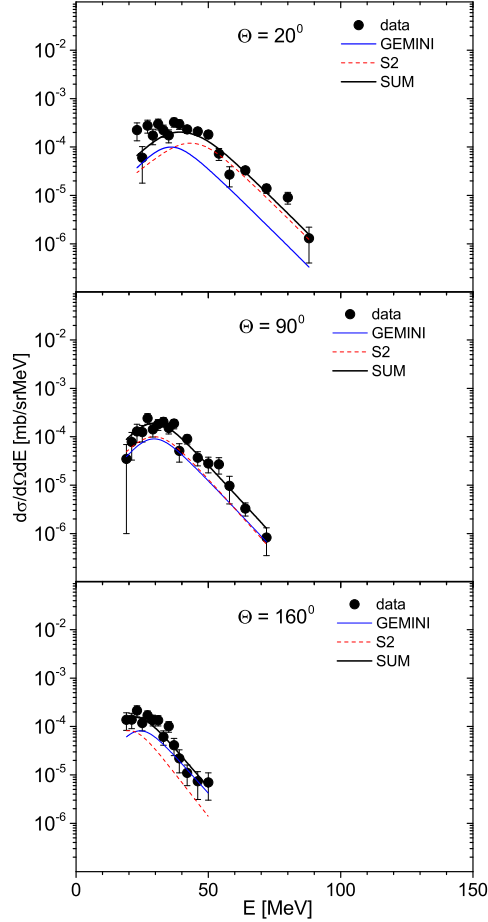
Figure 6.1: Experimental data (dots) and theoretical spectra for $Ag(p,^{18}O)$ at three scattering angles: 20° (top panel), 90 ° (middle panel) and 120° (lower panel). The blue (solid) line represents GEMINI++ spectra, the red (dashed) line depicts contribution from additional moving source (S2), whereas the black (thick solid) line shows sum of both contributions.

line - reproduces the high energy tail of the spectrum.

The situation is different for large scattering angle where the slower moving source dominates again for small energies but it gives comparable to the faster source contribution to the cross-section at high energies. This is a typical situation for all analyzed spectra for which introduction of two moving
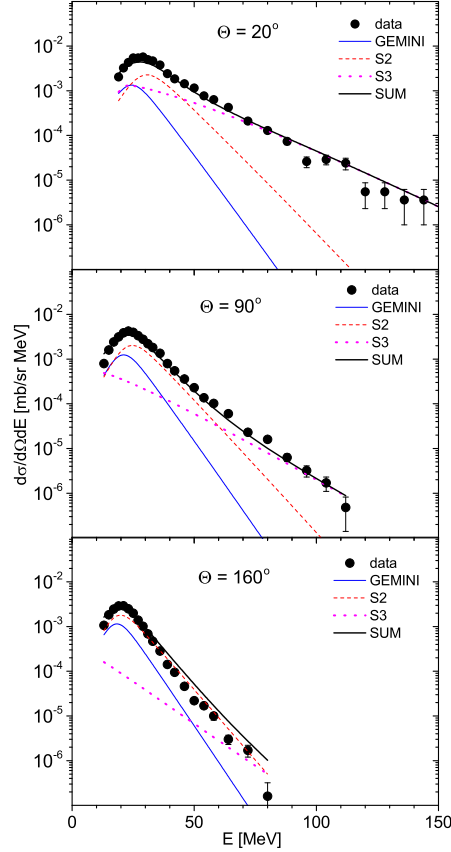
Figure 6.2: Experimental data (dots) and theoretical spectra for $Ag(p,^9Be)$ at three scattering angles: $20°$ (top panel), $90°$ (middle panel) and $120°$ (lower panel). The blue (solid) line represents GEMINI++ spectra, the red (dashed) line depicts contribution from slower moving source (S2), the magenta (dotted) line shows contribution of the second, faster source (S3) whereas the black (thick solid) line shows sum of all contributions.

sources was necessary.

The procedure described above enables to obtain the non-equilibrium production cross-section of IMF equal to the parameter σ_2 of the slow moving source (or to the sum of σ_2 and σ_3 - the appropriate parameters of both moving sources). Furthermore, sum of the equilibrium production cross-section evaluated by means of GEMINI++ and the above non-equilibrium

cross-section provided value of the total production cross-section.

The total cross-sections due to INCL++ [10] coupled to GEMINI++ [21, 22] as well as the total cross-sections obtained by fit of moving sources are presented together in fig. 6.3 as a function of the atomic mass number of ejectiles. In the lower panel of the figure the equilibrium emission cross-sections σ_{GEMINI} are shown. In the middle panel the non-equilibrium cross-sections parameterized by slower of the moving sources σ_2 are depicted, whereas that due to the faster moving source σ_3 are shown in the upper panel of the figure. The cross-sections for individual elements are presented by the same symbols and are connected by lines.

It is clear that the cross-sections decrease in average as a function of the atomic mass number, however, this dependence of the cross-sections is non-monotonic, parabola - like for each individual element.

6.3 Ratio of $\sigma_{\text{NEQ}}/\sigma_{\text{TOT}}$ as a function of atomic mass number A

It is important to note that the mass number A of the maximal cross-section determined by the INCL+GEMINI model for given element is not always the same as the mass number A at which the maximal cross-section of the non-equilibrium emission appears. Furthermore, variation of the equilibrium cross-sections with the mass number seems to be more rapid than variation of the corresponding non-equilibrium cross-sections.

Therefore it is quite difficult to predict how complicated may be the mass dependence of the ratio of non-equilibrium cross-sections to the total production cross-sections $\sigma_{\text{NEQ}}/\sigma_{\text{TOT}}$, i.e. to the sum of the equilibrium and non-equilibrium cross-sections.

The quantified values of the ratios are shown in fig. 6.4 as a function of the atomic mass number A of produced IMF. Different symbols connected by thin lines indicate the values of the ratio for the corresponding elements listed in the description on the right side of the figure.

The same symbol depicts results obtained for various isotopes of a given element. The horizontal line placed at 0.5 value of the ratio divides the set of all isotopes into two groups: one with the ratio corresponding to the dominance of the equilibrium processes and the second of the opposite property.

The following properties of the ratio of the non-equilibrium cross sections
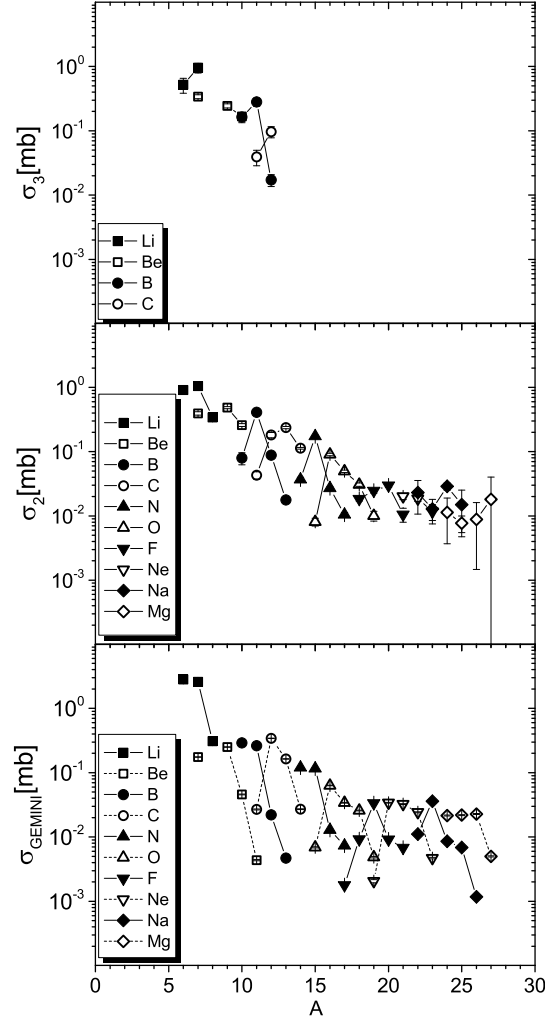
Figure 6.3: Production cross-sections of intermediate mass fragments evaluated by means of the INCL++ model coupled to the GEMINI++ one (lower panel), production cross-sections σ_2 from the phenomenological slow moving source (middle panel) and those (σ_3) due to the fast moving source (upper panel). Different elements are distinguished by using different symbols whereas various isotopes of the same element are represented by the same symbol.
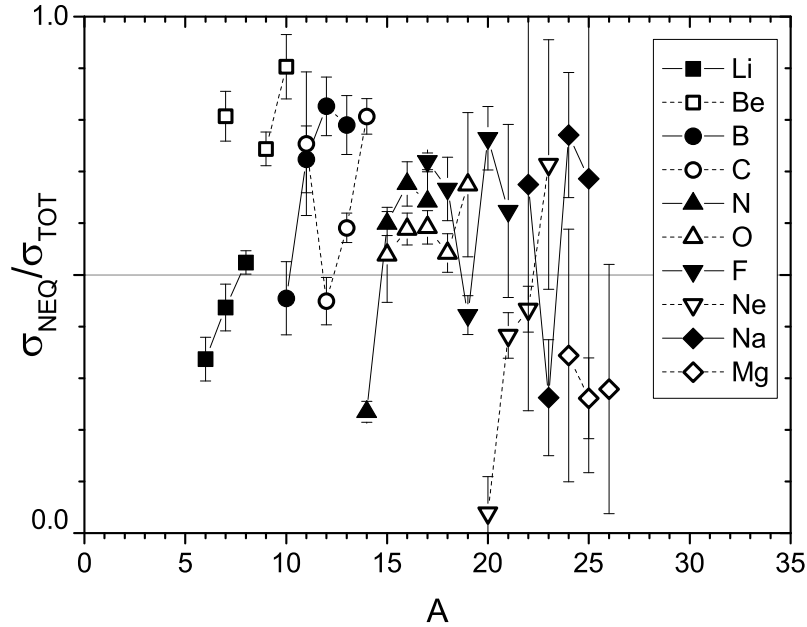
Figure 6.4: Atomic mass number A dependence of the ratio of non-equilibrium production cross-section to the total production cross-section for intermediate mass fragments emerging from $p + Ag$ collisions.

to the total cross-sections may be easily derived from this figure:

- The ratios larger than 0.5 are about 2 times more abundant than those smaller than 0.5. This is true for both small and large values of the atomic mass number A.

- Values of ratios close to 0.5 appear mainly at average mass number (A ~ 17) whereas those at smaller as well as at larger mass numbers are grouped into two separate sets. One set of the isotopes with the ratios smaller than 0.5 and the second set with the ratios larger than 0.5 for the same A values.

Such a specific dependence of the ratio $\sigma_{\mathrm{NEQ}}/\sigma_{\mathrm{TOT}}$ indicates that there exists no single monotonic trend of this ratio versus mass number A for all studied isotopes. One has to find some additional criterion which might
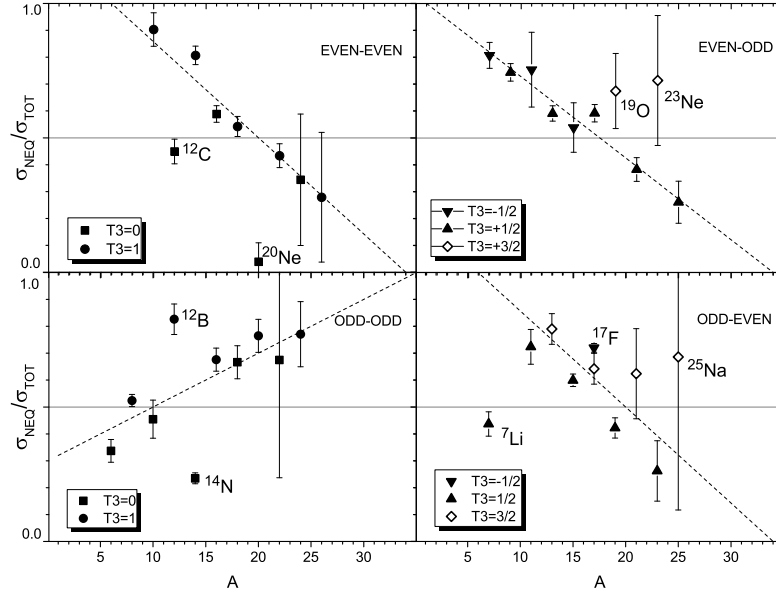
Figure 6.5: Atomic mass number A dependence of the ratio of non-equilibrium production cross-section to the total production cross-section for intermediate mass fragments emerging from $p + Ag$ collisions. Left upper panel of the figure presents the results for even-even (Z,N) products whereas other panels (in clockwise direction) contain results for even-odd, odd-even and odd-odd products. Different symbols are attributed to values of the ratio corresponding to different values of the third component of the isospin $T_3 = (N-Z)/A$ of ejectiles. Dashed lines are drawn to guide the eye.

select the isotopes into groups behaving in the same way when treated as a function of the mass number.

Two specific properties of the emitted intermediate mass fragments were applied for this purpose:

(i) the even/odd number of protons and neutrons - constituents of the IMF, and

(ii) the third component of the isospin of the fragment $T_3 \equiv (N-Z)/2$ representing excess (deficiency) of the number of neutrons in respect to the number of protons.

For this purpose all reaction products were divided into 4 subgroups of definite (Z,N): (even - even), (even - odd), (odd - even) and (odd - odd). The atomic mass dependence of the ratio $\sigma_{\mathrm{NEQ}}/\sigma_{\mathrm{TOT}}$ was presented for these subgroups in separate panels of the fig. 6.5: the upper-left panel for even-even (Z,N), the upper-right one for even-odd, *etc.*, in the clockwise direction. It turned out that the ratio $\sigma_{\mathrm{NEQ}}/\sigma_{\mathrm{TOT}}$ behaves in a very regular way for
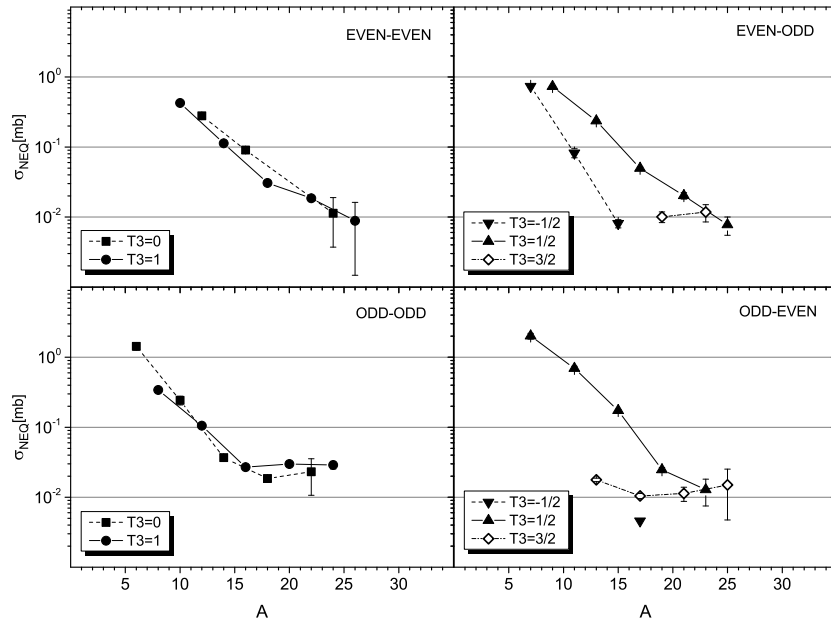
Figure 6.6: Atomic mass number dependence of the production cross-sections of intermediate mass fragments emerging due to non-equilibrium processes from $p + Ag$ collisions. Left upper panel of the figure presents the results for even-even (Z,N) products whereas other panels (in clockwise direction) contain results for even-odd, odd-even and odd-odd products. Different symbols are attributed to values of the cross-sections for fragments with different values of the third component of the isospin T_3=(N-Z)/A. The solid, dashed and dot-dashed lines are drawn to guide the eye.

each of these selected groups of isotopes (cf. fig. 6.5). Especially, it may be stated that this ratio decreases in average linearly with the mass number A of emitted fragment for even-even, even-odd and odd-even intermediate mass

fragments whereas it increases in average linearly for odd-odd ejectiles.
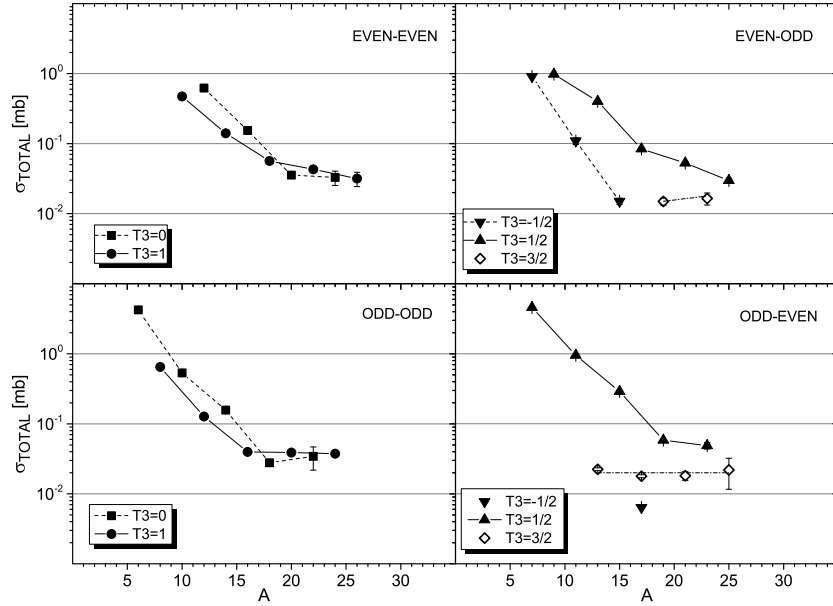
Figure 6.7: The same as in fig. 6.6 but for the total production cross-sections, i.e. for the sum of equilibrium and non-equilibrium production cross-sections. The solid, dashed and dot-dashed lines are drawn to guide the eye.

Furthermore, some deviations from such a regular behaviour may be observed for specific values of the third component of the isospin $T_3 \equiv (N\text{-}Z)/2$ of the emitted particles. For example, two of the four even-even ejectiles with $T_3=0$, namely ^{12}C and ^{20}Ne have much smaller ratio $\sigma_{NEQ}/\sigma_{TOT}$ than other even-even IMF with $T_3=0$ and all $T_3=1$ particles (cf. upper, left panel of fig. 6.5).

Second of such deviations is the fact that all $T_3=3/2$ nuclides for even-odd and odd-even ejectiles have larger $\sigma_{NEQ}/\sigma_{TOT}$ ratio than that which characterizes the $T_3=\text{-}1/2$ and $T_3=1/2$ nuclides (cf. upper-right and lower-right panel of the fig. 6.5).

The third example consists in the systematic deviation toward smaller ratio values of $T_3=0$ ejectiles in respect to the straight line averaging behaviour

of the odd-odd group of ejectiles whereas the IMF with $T_3=1$ deviate toward larger ratio values (cf. lower-left panel of the fig. 6.5).

While no physical model has been implied by the dependence presented in the fig. 6.5, the extremely regular behaviour achieved in this analysis certainly merits further consideration. The above regular variation of the $\sigma_{\mathrm{NEQ}}/\sigma_{\mathrm{TOT}}$ ratio indicates that the total cross-sections as well as the cross-section of equilibrium and non-equilibrium processes must behave in a regular way for the selected groups of IMF.
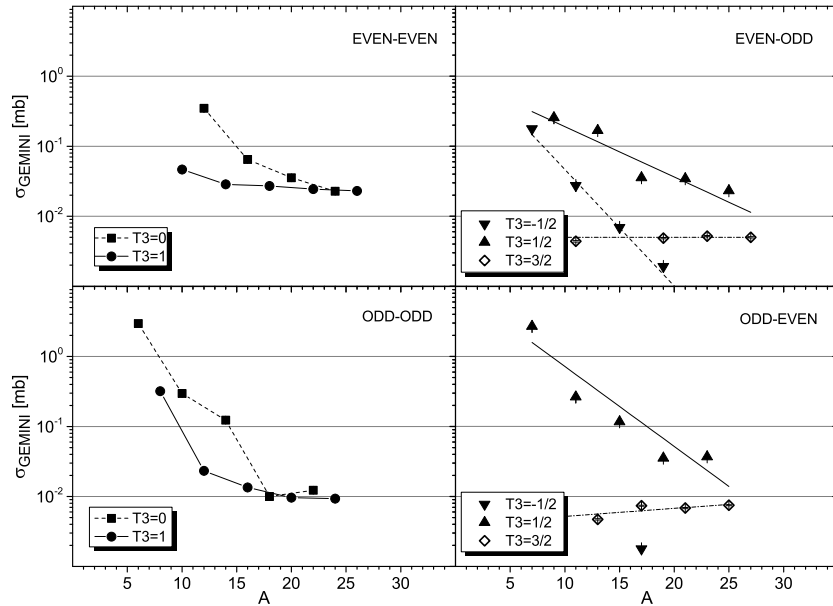
Figure 6.8: The same as in fig. 6.6 but for the equilibrium emission cross-sections evaluated by means of the INCL++ plus GEMINI++ models. The solid, dashed and dot-dashed lines are drawn to guide the eye.

To check the above statement the mass number dependences of the cross-sections for even-even, even-odd, *etc.*, reaction products are depicted in four panels (ordered in the same manner as in fig. 6.5) of figs. 6.6, 6.7 and 6.8 for pre-equilibrium processes, for sum of pre-equilibrium and equilibrium processes and for equilibrium emission, respectively.

As can be seen, the production cross-sections of different mechanisms behave in very similar manner, when the group of even-odd or odd-even fragments is taken into consideration (cf. right-upper and right-lower panels of figs. 6.6, 6.7 and 6.8).

Three well separated groups of the cross-sections are visible corresponding to T_3=-1/2, T_3=1/2, and T_3=3/2. Those representing particles with $T_3 = -1/2$ and T_3=1/2 show fast, exponential decreasing of the cross-sections versus the mass number A whereas the cross-sections of products with T_3=3/2 are almost independent of the mass number.

It should be also noted that the decreasing of the cross-sections for particles with T_3=-1/2 is much faster than that for particles with T_3=1/2.

The situation for even-even and odd-odd particles is different in respect to that described above (cf. left-upper and left-lower panels of figs. 6.6, 6.7 and 6.8). The mass dependence of the cross-sections for particles with T_3=0 and T_3=1 does not differ as strongly as that of the cross-sections for fragments with T_3=-1/2, T_3=1/2 and T_3=3/2, however, this difference changes from mechanism to mechanism.

For non-equilibrium processes (cf. left-upper and left-lower panels of fig. 6.6) the difference is almost negligible. It increases for total cross-sections (cf. corresponding panels of fig. 6.7) and becomes quite significant for equilibrium cross-sections (cf. fig. 6.8).

Chapter 7

Odd-even staggering of total production cross-section in spallation reactions

In the chapter 6 the dependence of the total production cross-sections of intermediate mass fragments (from Be to Mg) in $p + Ag$ collisions at proton energy of 480 MeV on mass number A was discussed for different values of the third component of the izospin of fragments. This total cross-sections were model independent because they were extracted from integration of the experimental differential cross-sections $d^2\sigma/d\Omega dE$. Furthermore the investigation of similar dependence was performed for model dependent production cross-section where the equilibrium processes of particle production were described by specific model, i.e. by GEMINI++ [21, 22] and the cross-sections for non-equilibrium processes were found as the difference between the experimental cross-sections and the GEMINI++ predictions.

In the present chapter another investigation is presented of predictive power of the INCL++ model coupled to three models of the second stage of the spalation reaction, i.e. GEMINI++ SMM [25] and ABLA07 [20]. It was tested whether these model cross-sections are able to reproduce very specific phenomenon observed in spallation reactions, namely the odd-even staggering of the total production cross-sections.

Odd-even staggering (OES) refers to the enhancement of production of odd Z particles to adjacent even- Z ones (or vice versa). Such an effect has been observed in many spallation and fragmentation reactions [92–96]. The main cause of this behavior is not yet fully understood, but it is usually

attributed to phenomena related to the emission of particles from excited nuclei, in the context of pairing or mean-field effects (shell effects, nuclear deformations) that affect the density of nuclear states in the final step of the reaction processes.

It has been observed that for neutron-deficient nuclei the OES effects are independent of the nuclear systems (projectile and target mass) and the beam energies [96]. However, this is not the case for isotopes of neutron-rich nuclei. Moreover, in the work of Ricchiardi et al [94] it became clear that for the light fragments the OES effect is strong for the N = Z configuration and increases with the N-Z difference.

Previous work suggested that the OES and nuclear structure effects can be studied along the chain of the third component of the isospin (T_3 = (N-Z)/A), where such effects become prominent [96].

In this work, the effects of OES are investigated using the IMF data measured by Green et al. [29] for which the total production cross-section for different IMFs was calculated in the previous chapter. The aim of this analysis is to examine the OES effects as a function of atomic number Z of the measured IMF for different values of T_3 and finally to compare the data with the predictions of INCL ++(v5.3) plus second stage models (SMM, ABLA07, GEMINI ++).

7.1 Odd-Even staggering in total production cross-sections

It is interesting to compare the specific behaviour of total cross-sections as a function of Z. It was shown on the basis of very rich set of fragmentation data published for $^{56}Fe+p$ reaction at E/A=1 GeV that the total cross-sections reveal very characteristic dependence when presented as function of Z for individual values of T_3 [89]. The cross-sections for even values of Z are systematically larger than those for odd values when nuclei with even (or odd) mass number A are taken into consideration.

Such an effect, called odd-even staggering is strong for even-A nuclei and rather weak for odd-A nuclei. The staggering is most pronounced for T_3=0 (for even-A nuclei) and for T_3=-1/2 (for odd-A nuclei) decreasing when value of T_3 is significantly different from these values.

As it was mentioned earlier the procedure of determination of the total

cross-sections applied in the present work is model independent. Thus variation of the total cross-sections with changing A, Z and T_3 should correspond to the typical behaviour of the cross-sections observed in spallation and/or fragmentation of other target nuclei by energetic protons.

This is indeed the case as can be seen in fig. 7.1.
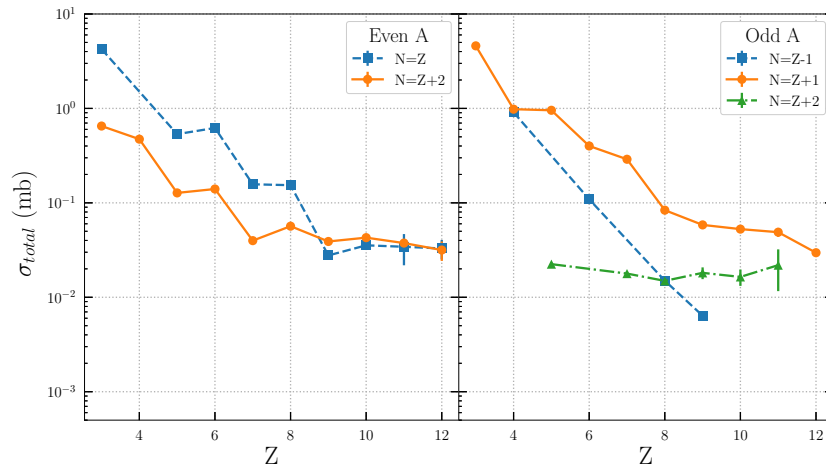
Figure 7.1: The atomic number Z dependence of total production cross-sections for even-mass nuclei (left panel of the figure) and for odd-mass nuclei (right panel). Cross-sections representing intermediate mass fragments with the same third component of the isospin $T_3 \equiv (N\text{-}Z)/A$ are shown by the same symbols connected by thin lines.

Odd-even staggering of the total cross-sections is pronounced for even-A nuclei and is not visible for odd-A nuclei (fig. 7.1). Therefore, it is concluded that the total cross-sections dependence on A, Z and T_3 found in the present investigation agrees qualitatively with typical behaviour of spallation and fragmentation data.

To quantitatively discuss the staggering effect of the data and compare it with the predictions of the models, one needs to introduce a variable (δ) whose value would provide the needed information. This is discussed in the next section.

7.2   Dependence of δ-function on third component of isospin

To quantify OES effect, a procedure proposed by Tracy *et al.* [97] was applied
in the form given by Ricciardi *et al.* [94] for the Z-dependence of cross-sections
at a fixed N-Z. The δ value greater than zero (less than zero) evaluated by
equation 7.1 gives a relative increase in the cross-section for even-Z (odd- Z)
products with respect to a smooth Z dependence.

$$\delta\left(Z + 3/2\right) \equiv \frac{1}{8}\left(-1\right)^{Z+1}\left[\left(L_3 - L_0\right) - 3\left(L_2 - L_1\right)\right] \tag{7.1}$$

where

$$L_i \equiv ln(\sigma\left(Z + i\right))$$

The δ value is assigned on the midpoint of the Z interval from Z to Z+3
where smooth Z-dependence was postulated.

The δ-function values are shown in fig. 7.2 for experimental total cross-
sections (open black squares) and for theoretical cross-sections (solid col-
ored symbols). The theoretical cross-sections were evaluated using INCL++
as the first-stage model and three different second-stage models (ABLA07,
GEMINI++ and SMM) describing the de-excitation of the equilibrated, ex-
cited residual nucleus from the intranuclear cascade.

As in fig. 7.2, the delta function values are positive for the cross-sections
of IMF with N=Z (upper left panel of the figure) and N=Z+2 (lower left
panel) obtained from experimental data. In contrast, the delta function is
negative for IMF with N=Z+1 (upper right panel) and N=Z+3 (lower right
panel).

This indicates that the even Z cross-sections for N=Z and N=Z+2 are
larger than the smooth trend, while it is the case of the odd- Z cross-sections
for N=Z+1 and Z+3. This information is in perfect agreement with the
qualitative conclusions drawn from the inspection of fig. 7.1, where the
experimental cross-sections are collected.

Moreover, the absolute values of the δ-function are close to zero for the
products with N=Z+3, while they are drastically different from zero for other
products. This information is again consistent with fig. 7.1, where the Z-
dependence of the cross-section is lowest for N=Z+3 (smooth line), especially
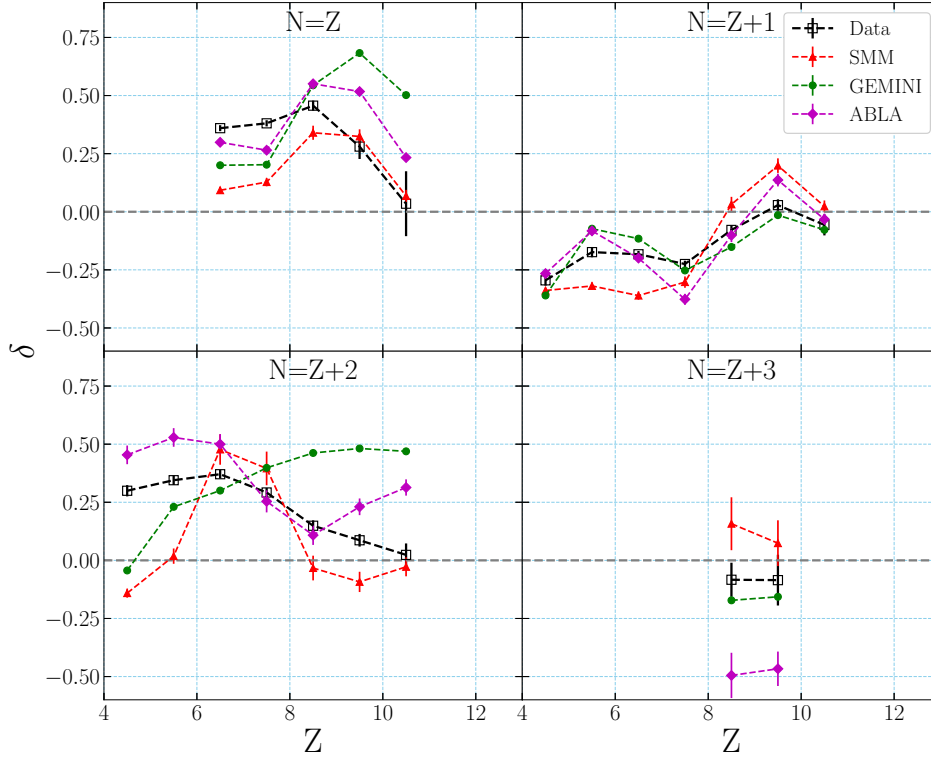
Figure 7.2: Plot of the δ-function versus atomic number Z of the reaction
products. The open, black squares depict values of the δ-function evaluated
for experimental cross-sections whereas magenta, green, and red symbols cor-
respond to the δ-function values obtained with the cross-sections of ABLA07,
GEMINI++ and SMM models, respectively.

compared to N=Z and N=Z+2 (zigzag line). Moreover, the values of the δ-
functions for the experimental cross-sections approach zero as the atomic
number Z of the products increases, which is consistent with the general
trend that the OES effect decreases with increasing Z (cf. Ref. [96]).

Despite the general agreement between the sign of the δ-function of the
experimental cross-sections and those of all three models, there are also vis-
ible discrepancies between experimental and theoretical δ-functions. They
are particularly clear for products with N=Z+2. In this case, the δ-function
evaluated for experimental cross-sections *decreases* from values around 0.3 at

Z=4.5 to zero at Z=10.5, while the δ-function determined for the GEMINI ++ cross-sections *increases* monotonically from -0.05 at Z=4.5 to 0.47 at Z=10.5. Thus, the tendency of the variation of the experimental δ-function and that of GEMINI ++ is also not reproduced.

There are clear differences between the experimental and model δ-function for ABLA07 (the δ-function values do not change monotonically) and for SMM (the δ-function values are large and positive for only two points in the interval 4.5 - 10.5, while they are small and negative at both ends of this interval). Smaller but also significant differences between experimental and model δ-function exist for reaction products with N = Z. The shape of all model δ-function is almost the same as that of the experimental δ- function, but there are two differences. The magnitude of the experimental and model δ-function values are different, and the position of the maximum of the model δ-function is different from that of the experimental one.

The question arises about the origin of the differences between the δ-function obtained from the experimental cross-sections and that calculated from model cross-sections applied in the framework of the two-stage model with different models describing the second stage of the reaction.

The natural candidate for explaining these differences seems to be the neglect of non-equilibrium processes in the model calculations. They were introduced in a phenomenological way in the overall experimental cross-sections but are not explicitly present in the model cross-sections. They are only included in the evaluation of the cross-sections of light charged particles, which are not analyzed in the present study. Of course, they affect the population of residual nuclei after the intranuclear cascade due to the coalescence of nucleons into ejectiles consisting of less than 5 nucleons. Moreover, such a coalescence process changes the population of excited states of the residual nuclei of the cascade.

To check whether an increase in the coalescence of nucleons during the stage of the intranuclear cascade can significantly modify the δ-function determined from model cross-sections, the model calculations were repeated and extended by the coalescence effect to intermediate-mass fragments with mass number A equal up to 8. It was found that such a modification has no significant effect.

Chapter 8

Summary

In this thesis the studies of various aspects of nuclear spallation have been undertaken. Among broad spectrum of not well understood phenomena related to this kind of reaction the four problems were addressed.

1. The proceeding of the initial phase of the proton target nucleus collision. It is commonly accepted hypothesis, that energy dissipation inside the struck nucleus and observed abundant emission of fast particles in spallation reaction is an effect of the intranuclear cascade of binary interactions among the target nucleus constituents.

   Nucleons and pions are the main products of the intranuclear cascade, i.e. of the initial phase of the reaction. Thus, reliable experimental data for these particles, measured in broad range of their energies are necessary to study the initial phase of the reaction. New experimental data ($d^2\sigma/d\Omega dE$) for production of H isotopes and the charged pions in the $p + Nb$ reaction at 3.5 GeV proton bombarding energy were obtained. These data were measured in angular range from 20° to 80° of the laboratory emission angle θ. The high acceptance and magnetic field of HADES spectrometer permitted to obtain the cross-section distributions exceeding the energy ranges of the data available up to now in the literature. It was achieved for almost all detected particles and detection angles. The most significant extension of the measured kinematic region was obtained for proton data. The quality of the achieved distributions has been verified by their comparison to the other world data of the similar type available in the scientific literature.

The experimental data have been compared to the results of calculations performed with the use of three contemporary theoretical models (GiBUU, UrQMD, INCL++) commonly used in nuclear and particle physics. All these models adopt the assumption of the intranuclear cascade as a sequence of binary collisions among the reaction participants embedded in the target nucleus. The INCL++ model is additionally equipped with the hypothetical mechanizm of surface coalescence permitting the dynamical formation of light nuclear clusters.

The qualitative as well as the quantitative analysis of the predictive power of theoretical models has been performed. Despite that all the tested models are able to reproduce the shapes of the experimental excitation functions the magnitudes of the theoretical cross-sections differ from the data in almost all examined cases by the factors up to ~ 2.

It can be concluded that the examined theoretical models do not contain all physics ingredients demanded for description of the experimental spectra of π, p, d and t with precision better in average than factor ~ 2.

2. The emission of nuclear fragments of very broad spectrum of masses. It is believed that this is an effect of the deexcitation of the after-cascade remnant nucleus and the responsible mechanism acts in the second step of spallation reaction.

   The total production cross sections of heavy and intermediate mass products of the reaction contain therefore information on both, first and second stage of the spallation reaction. In the present work the predictive power of four theoretical models of the second stage of the spallation reaction (ABLA07, GEM2, GEMINI++, SMM) have been studied. For this purpose their ability to reproduce the total reaction cross-sections for the production of isotopes of the atomic numbers of $3 \leq Z \leq 56$ from $^{136}Xe + p$ collisions at an energy of 1 GeV/nucleon [89] was investigated. In all cases the first step of the reaction has been simulated with the use of INCL++ model.

   Significant differences between the results of the models and discrepancies with experimental data have been found. They were quantified with the use of the A-factor - a tool allowing the numerical comparison

of the predictive power of theoretical models.

It was realized that for the calculation of cross-sections for isotope production in the very broad range of masses the predictive power of GEMINI++ is the highest whereas the GEM2 results differ most significantly from the data and from the results of other models.

3. The yields of the particles resulting from the first and second phase of the reaction. The contribution of the non-equlibrium and equilibrium emission to the total cross-section for the given isotope is a complicated function of the isospin of emitted particles.

   Qualitative properties of the spectra and angular distributions of intermediate mass fragments (particles heavier than ^4He but lighter than fission fragments) indicate in many spallation reactions the contribution of a non-equilibrium mechanism to the reaction. Such a phenomenon has been studied for the angular distributions published in [29] where production of Li, Be, B, C, N, O, F, Ne, Na and Mg isotopes was investigated in $p + Ag$ collisions at a proton beam energy of 480 MeV.

   The equilibrium and non-equilibrium components of the cross-section were established by integration of angular distributions of INCL++ and GEMINI++ supplied by phenomenological model of moving source with parameters fitted to experimental angular distributions, respectively. The remarkable dependence of the relative yield of both emission classes on the mass A of the emitted fragments and their third component of isospin $T_3 = (N\text{-}Z)/A$ was observed.

4. The variation of the total production cross-section known as an Odd-Even Staggering. This effect is dependent on the charge and mass relations of the emitted reaction products. Most likely this phenomenon is relevant to the available density of states during de-excitation of the excited after-cascade remnant nucleus.

   The dependence of the variation of the total cross-section for fragment emission in the spallation reaction on the third component of isospin T_3, called the Odd-Even Staggering (OES) has been realized and examined for the data obtained from [29].

   The examination of the ability of three theoretical models of nucleus de-excitation (ABLA07, GEMINI++, SMM) coupled to INCL++, to

reproduce the observed staggering effect has been done. The δ-function proposed in [96] was calculated both for experimental cross-sections as well as for theoretical ones. For fragments of N = Z the shape of all model δ-function is almost similar to that of the experimental one, however the disagreement in magnitudes of all of them has been observed. For emitted particles of N $\neq$ Z the deviation between the experimental and theoretical δ-functions is even stronger. It indicates that all examined models neglect the phenomena responsible for experimentally observed OES of isotopic cross-sections.

At the current stage of the theoretical examination of the nuclear spallation reactions induced by protons it seems that the precision of the theoretical models providing solution for different classes of involved processes is still not sufficient in order to identify the exact mechanisms responsible for observed experimental effects and to define the range of their applicability and contribution to the production cross-section.

Apparently the physics ingredients in all used in this thesis theoretical models are sufficient to describe the shapes of the experimental spectra of spallation products. However their magnitudes can be predicted only within the precision of factor usually about 2.

Provided here new experimental cross-sections of high quality and performed critical analysis of the predictive power of various theoretical models of nuclear spallation can be an important contribution to the further extension of understanding of nuclear spallation physics.

Bibliography

[1] J. M. Carpenter, Nuclear Instruments and Methods **145**, 91 (1977).

[2] H. Ravn, Philosophical Transactions of the Royal Society A: Mathematical, Physical and Engineering Sciences **356**, 1955 (1998).

[3] C. Bowman, E. Arthur, P. Lisowski, G. Lawrence, R. Jensen, et al., Nuclear Instruments and Methods in Physics Research Section A: Accelerators, Spectrometers, Detectors and Associated Equipment **320**, 336 (1992).

[4] M. Meneguzzi, J. Audouze, and H. Reeves, Astronomy and Astrophysics **15**, 337 (1971).

[5] R. Serber, Phys. Rev. **72**, 1114 (1947).

[6] J. Cugnon, T. Mizutani, and J. Vandermeulen, Nuclear Physics A **352**, 505 (1981).

[7] A. Boudard, J. Cugnon, S. Leray, and C. Volant, Phys. Rev. C **66**, 044615 (2002).

[8] A. Boudard, J. Cugnon, S. Leray, and C. Volant, Nuclear Physics A **740**, 195 (2004).

[9] A. Boudard, J. Cugnon, J.-C. David, S. Leray, and D. Mancusi, Physical Review C **87**, 014606 (2013).

[10] D. Mancusi, A. Boudard, J. Cugnon, J.-C. David, P. Kaitaniemi, et al., Phys. Rev. C **90**, 054602 (2014).

[11] O. Buss, T. Gaitanos, K. Gallmeister, H. van Hees, M. Kaskulov, et al., Physics Reports **512**, Transport-theoretical Description of Nuclear Reactions, 1 (2012).

[12] S. Bass, M. Belkacem, M. Bleicher, M. Brandstetter, L. Bravina, et al., Progress in Particle and Nuclear Physics **41**, 255 (1998).

[13] M. Bleicher, E. Zabrodin, C. Spieles, S. A. Bass, C. Ernst, et al., Journal of Physics G: Nuclear and Particle Physics **25**, 1859 (1999).

[14] Y. Nara, N. Otuka, A. Ohnishi, K. Niita, and S. Chiba, Phys. Rev. C **61**, 024901 (1999).

[15] H. W. Bertini, Phys. Rev. **131**, 1801 (1963).

[16] H. W. Bertini, Phys. Rev. **188**, 1711 (1969).

[17] K. Gudima, S. Mashnik, and V. Toneev, Nuclear Physics A **401**, 329 (1983).

[18] Y. Yariv and Z. Fraenkel, Phys. Rev. C **20**, 2227 (1979).

[19] Y. Yariv and Z. Fraenkel, Phys. Rev. C **24**, 488 (1981).

[20] A. Kelic, M. V. Ricciardi, and K.-H. Schmidt, arXiv preprint arXiv:0906.4193 (2009).

[21] R. Charity, M. McMahan, G. Wozniak, R. McDonald, L. Moretto, et al., Nuclear Physics A **483**, 371 (1988).

[22] R. J. Charity, Phys. Rev. C **82**, 014610 (2010).

[23] S. Furihata, Nuclear Instruments and Methods in Physics Research Section B: Beam Interactions with Materials and Atoms **171**, 251 (2000).

[24] S. Furihata and T. Nakamura, Journal of Nuclear Science and Technology **39**, 758 (2002).

[25] J. Bondorf, A. Botvina, A. Iljinov, I. Mishustin, and K. Sneppen, Physics Reports **257**, 133 (1995).

[26] A. Budzanowski, M. Fidelus, D. Filges, F. Goldenbaum, H. Hodde, et al., Physical Review C **82**, 034605 (2010).

[27] U. Singh, D. Filges, F. Goldenbaum, B. Kamys, Z. Rudy, et al., The European Physical Journal A **54**, 1 (2018).

[28] U. Singh, B. Kamys, S. Sharma, and K. Pysz, Acta Physica Polonica. B **50**, 1451 (2019).

[29] R. E. L. Green, R. G. Korteling, and K. P. Jackson, Phys. Rev. C **29**, 1806 (1984).

[30] T. Koopmans, Physica **1**, 104 (1934).

[31] A. Wapstra and G. Audi, Nuclear Physics A **432**, 55 (1985).

[32] A. M. Lane, Phys. Rev. Lett. **8**, 171 (1962).

[33] J. Cugnon, C. Volant, and S. Vuillier, Nuclear Physics A **620**, 475 (1997).

[34] S. T. Butler and C. A. Pearson, Phys. Rev. **129**, 836 (1963).

[35] E. A. Uehling and G. E. Uhlenbeck, Phys. Rev. **43**, 552 (1933).

[36] G. F. Bertsch, H. Kruse, and S. D. Gupta, Phys. Rev. C **29**, 673 (1984).

[37] G. F. Bertsch, H. Kruse, and S. D. Gupta, Phys. Rev. C **29**, 673 (1984).

[38] K. Niita, W. Cassing, and U. Mosel, Nuclear Physics A **504**, 391 (1989).

[39] A. Letourneau, A. Böhm, J. Galin, B. Lott, A. Péghaire, et al., Nuclear Physics A **712**, 133 (2002).

[40] P. Hodgson and E. Beták, Physics Reports **374**, 1 (2003).

[41] H. Iwamoto and Y. Uozumi, in Aip conference proceedings, Vol. 1005, 140 (2008).

[42] D. Wei, N. Wang, and L. Ou, Journal of Physics G: Nuclear and Particle Physics **41**, 035104 (2014).

[43] K. Pysz, Phys. Rev. C **91**, 011602 (2015).

[44] S. Typel, G. Röpke, T. Klähn, D. Blaschke, and H. H. Wolter, Phys. Rev. C **81**, 015803 (2010).

[45] J. I. Kapusta, Phys. Rev. C **21**, 1301 (1980).

[46] B. Monreal, S. A. Bass, M. Bleicher, S. Esumi, W. Greiner, et al., Phys. Rev. C **60**, 031901 (1999).

[47] L.-W. Chen, C. Ko, and B.-A. Li, Nuclear Physics A **729**, 809 (2003).

[48] N. Sharma, T. Perez, A. Castro, L. Kumar, and C. Nattrass, Phys. Rev. C **98**, 014914 (2018).

[49] J. Aichelin, E. Bratkovskaya, A. Le Fèvre, V. Kireyeu, V. Kolesnikov, et al., Phys. Rev. C **101**, 044905 (2020).

[50] J. Weil, V. Steinberg, J. Staudenmaier, L. G. Pang, D. Oliinychenko, et al., Phys. Rev. C **94**, 054905 (2016).

[51] S. Acharya, D. Adamová, A. Adler, J. Adolfsson, M. M. Aggarwal, et al., Physical Review C **101**, 044906 (2020).

[52] S. Acharya, D. Adamova, S. P. Adhya, A. Adler, J. Adolfsson, et al., Physics Letters B **800**, 135043 (2020).

[53] V. Weisskopf, Phys. Rev. **52**, 295 (1937).

[54] V. F. Weisskopf and D. H. Ewing, Phys. Rev. **57**, 472 (1940).

[55] F. Atchison, *Spallation and fission in heavy metal nuclei under medium energy proton bombardement*, 1980.

[56] W. Hauser and H. Feshbach, Phys. Rev. **87**, 366 (1952).

[57] L. G. Moretto, Nuclear Physics A **247**, 211 (1975).

[58] D. E. DiGregorio, M. diTada, D. Abriola, M. Elgue, A. Etchegoyen, et al., Phys. Rev. C **39**, 516 (1989).

[59] A. Botvina, A. Iljinov, I. Mishustin, J. Bondorf, R. Donangelo, et al., Nuclear Physics A **475**, 663 (1987).

[60] A. Botvina and I. Mishustin, The European Physical Journal A-Hadrons and Nuclei **30**, 121 (2006).

[61] G. Agakishiev et al. (HADES Collaboration), Physics Letters B **715**, 304 (2012).

[62] G. Agakishiev et al. (HADES Collaboration), Phys. Rev. C **88**, 024904 (2013).

[63] G. Agakishiev et al. (HADES Collaboration), Phys. Rev. C **90**, 054906 (2014).

[64] G. Agakishiev et al. (HADES Collaboration), Eur. Phys. J. A **50**, 81 (2014).

[65] G. Agakishiev et al. (HADES Collaboration), Phys. Rev. Lett. **114**, 212301 (2015).

[66] J. Adamczewski-Musch et al. (HADES Collaboration), Phys. Rev. C **94**, 025201 (2016).

[67] J. Adamczewski-Musch et al. (HADES Collaboration), Physics Letters B **781**, 735 (2018).

[68] I. Kipnis, T. Collins, J. DeWitt, S. Dow, A. Frey, et al., IEEE Transactions on Nuclear Science **44**, 289 (1997).

[69] *Hgeant-hades simulation package*.

[70] R. Brun, L. Urban, F. Carminati, S. Giani, M. Maire, et al., *Geant: detector description and simulation tool*, tech. rep. (Cern, 1993).

[71] M. S. Garcia, "Momentum reconstruction and pion production analysis in the hades spectrometer at gsi", PhD thesis (Universidade de Santiago de Compostela, 2003).

[72] R. Brun and F. Rademakers, Nuclear Instruments and Methods in Physics Research Section A: Accelerators, Spectrometers, Detectors and Associated Equipment **389**, New Computing Techniques in Physics Research V, 81 (1997).

[73] G. Agakichiev, C. Agodi, H. Alvarez-Pol, E. Atkin, E. Badura, et al., The European Physical Journal A **41**, 243 (2009).

[74] P. Tlustý, M. Weber, and P. Salabura (HADES), GSI Scientific Report, 2010.

[75] A. Bolshakova, I. Boyko, D. Dedovitch, A. Elagin, M. Gostkin, et al., The European Physical Journal C **62**, 293 (2009).

[76] A. Bolshakova, I. Boyko, D. Dedovitch, A. Elagin, M. Gostkin, et al., The European Physical Journal C **62**, 697 (2009).

[77] A. Bolshakova, I. Boyko, D. Dedovitch, A. Elagin, M. Gostkin, et al., The European Physical Journal C **63**, 549 (2009).

[78] A. Bolshakova, I. Boyko, D. Dedovitch, A. Elagin, M. Gostkin, et al., The European Physical Journal C **64**, 181 (2009).

[79] A. Bolshakova, I. Boyko, D. Dedovitch, A. Elagin, D. Emelyanov, et al., The European Physical Journal C **70**, 573 (2010).

[80] A. Bolshakova, I. Boyko, D. Dedovitch, A. Elagin, M. Gostkin, et al., The European Physical Journal C **71**, 1 (2011).

[81] A. Bolshakova, I. Boyko, D. Dedovitch, A. Elagin, D. Emelyanov, et al., The European Physical Journal C **72**, 1 (2012).

[82] M. Fidelus, D. Filges, F. Goldenbaum, L. Jarczyk, B. Kamys, et al., Physical Review C **96**, 064618 (2017).

[83] A. Bubak, A. Budzanowski, D. Filges, F. Goldenbaum, A. Heczko, et al., Physical Review C **76**, 014618 (2007).

[84] A. Budzanowski, M. Fidelus, D. Filges, F. Goldenbaum, H. Hodde, et al., Physical Review C **78**, 024603 (2008).

[85] A. Budzanowski, M. Fidelus, D. Filges, F. Goldenbaum, H. Hodde, et al., Physical Review C **80**, 054604 (2009).

[86] M. Fidelus, D. Filges, F. Goldenbaum, H. Hodde, A. Jany, et al., Physical Review C **89**, 054617 (2014).

[87] S. K. Sharma, B. Kamys, F. Goldenbaum, and D. Filges, The European Physical Journal A **53**, 1 (2017).

[88] Transport meets HADES, symposium during the HADES Collaboration Meeting XL, ed., 2021.

[89] P. Napolitani, K.-H. Schmidt, L. Tassan-Got, P. Armbruster, T. Enqvist, et al., Physical Review C **76**, 064609 (2007).

[90] L. Giot, J. Alcantara-Nunez, J. Benlliure, D. Perez-Loureiro, L. Audouin, et al., Nuclear Physics A **899**, 116 (2013).

[91] S. K. Sharma, B. Kamys, F. Goldenbaum, and D. Filges, The European Physical Journal A **52**, 1 (2016).

[92] A. M. Poskanzer, G. W. Butler, and E. K. Hyde, Phys. Rev. C **3**, 882 (1971).

[93] C. Zeitlin, L. Heilbronn, J. Miller, S. E. Rademacher, T. Borak, et al., Phys. Rev. C **56**, 388 (1997).

[94] M. Ricciardi, A. Ignatyuk, A. Kelić, P. Napolitani, F. Rejmund, et al., Nuclear Physics A **733**, 299 (2004).

[95] P. Napolitani, F. Rejmund, L. Tassan-Got, M. V. Ricciardi, A. Kelic, et al., International Journal of Modern Physics E **13**, 333 (2004).

[96] B. Mei, X. L. Tu, and M. Wang, Phys. Rev. C **97**, 044619 (2018).

[97] B. L. Tracy, J. Chaumont, R. Klapisch, J. M. Nitschke, A. M. Poskanzer, et al., Phys. Rev. C **5**, 222 (1972).